Mechanical Characterization and Numerical Modelling of Auxetic Sheet Metal for Innovative Lightweight Structure Design

Dissertation

zur Erlangung des Grades

des Doktors der Ingenieurwissenschaften

der Naturwissenschaftlich-Technischen Fakultät

der Universität des Saarlandes

von

Arash Gordanshekan, M.Sc.

Saarbrücken

2025

Tag des Kolloquiums:	07.11.2025
Dekan:	Prof. Dr.-Ing. Dirk Bähre
Berichterstatter:	Prof. Dr.-Ing. Stefan Diebels Prof. Dr.-Ing. Hans-Georg Herrmann
Akad. Mitglied:	Dr.-Ing. Niklas König
Vorsitz:	Prof. Dr. mont. Christian Motz

To my daughter Noura, whose smile reminded me every day of what truly matters.

Abstract

This dissertation presents a comprehensive study on the characterization of mechanical behavior and numerical modeling of auxetic sheet metals exhibiting a negative Poisson's ratio designed for lightweight and high-performance structural applications. Focusing on rotating unit structures fabricated from AlMg3 aluminum alloy, the research combines experimental characterization with advanced computational techniques to understand and predict the material response under various loading conditions.

The experimental work includes uniaxial and biaxial tensile tests, supported by Digital Image Correlation (DIC) and Infrared Thermography (IRT) for in-situ strain and temperature analysis. Parametric studies were performed to investigate the influence of pattern size, aspect ratio and orientation angle on the global auxetic effect, stiffness and strength of the perforated sheet. A representative volume element (RVE) was identified for effective property evaluation and anisotropic behavior was characterized based on the structural geometry at different orientation angles.

On the numerical side, fully resolved finite element simulations and homogenization techniques were employed to extract effective mechanical properties from the microscale. A macroscopic anisotropic elasto-plastic material model was developed, derived from microscale behavior and implemented in ABAQUS® using a user-defined material subroutine (UMAT). This model accurately captures both the anisotropy and pressure-sensitive plasticity observed in experiments and was validated through comparison with test data, including uniaxial loading scenarios.

The findings provide a validated framework for the design and analysis of auxetic structures and contribute to the broader understanding of metamaterials in engineering.

Zusammenfassung

Diese Dissertation befasst sich umfassend mit der Charakterisierung des mechanischen Verhaltens und der numerischen Modellierung auxetischer Bleche mit negativem Querkontraktionszahl für den Einsatz in innovativen, gewichtsoptimierten Strukturen. Im Fokus stehen „Rotating-Unit"-Strukturen aus der AlMg3-Aluminiumlegierung, deren Verhalten unter verschiedenen Belastungsbedingungen sowohl experimentell als auch numerisch untersucht wurde.
Die experimentellen Untersuchungen umfassen einachsige und biaxiale Zugversuche, die durch Digitale Bildkorrelation (DIC) und Infrarot-Thermografie (IRT) zur in-situ Analyse von Dehnungen und Temperaturfeldern unterstützt wurden. Parametrische Studien wurden durchgeführt, um den Einfluss von Mustergröße, Seitenverhältnis der Perforationen sowie der Orientierung des Musters auf globale Eigenschaften wie den auxetischen Effekt, die Steifigkeit und die Festigkeit der perforierten Bleche zu analysieren. Ein repräsentatives Volumenelement (RVE) wurde zur Ermittlung effektiver Materialkennwerte definiert und das anisotrope Materialverhalten wurde in Abhängigkeit von der strukturellen Geometrie unter verschiedenen Orientierungswinkeln charakterisiert.
Auf numerischer Ebene wurden vollständig aufgelöste Finite-Elemente-Simulationen sowie Homogenisierungstechniken eingesetzt, um effektive mechanische Eigenschaften auf der Mikroskala zu bestimmen. Basierend auf dem mikroskopischen Materialverhalten wurde ein makroskopisches, anisotropes, elasto-plastisches Materialmodell entwickelt und mittels einer benutzerdefinierten Materialsubroutine (UMAT) in ABAQUS® implementiert. Das Modell bildet sowohl die Anisotropie als auch die in den Experimenten beobachtete druckabhängige Plastizität realitätsgetreu ab und wurde erfolgreich anhand experimenteller Ergebnisse, einschließlich einachsiger Zugversuche, validiert.
Die Ergebnisse dieser Arbeit liefern ein zuverlässiges und übertragbares Rahmenwerk zur Beschreibung und Auslegung auxetischer Strukturen und leisten einen wesentlichen Beitrag zum Verständnis von Metamaterialien in der Technik.

Acknowledgement

The research presented in this dissertation was conducted during my time as a doctoral student at the Chair of Applied Mechanics at Saarland University in Saarbrücken. I am sincerely grateful to all those who supported and accompanied me on this academic journey.

First and foremost, I would like to express my profound gratitude to my advisor, Prof. Dr.-Ing. Stefan Diebels. His unwavering support, insightful feedback and generous investment of time played a decisive role in shaping the course of this work. The opportunity to work under his supervision in such a positive and intellectually stimulating environment marked a significant and formative chapter in my life. His guidance—both scientific and personal—has been invaluable throughout every stage of this dissertation.

I would also like to thanks my second reviewer Prof. Dr.-Ing. Hans-Georg Herrmann for taking up the task of reviewing this work.

I would like to take this opportunity to express my sincere thanks to Dr.-Ing. Wolfgang Ripplinger, who accompanied and supported me from the very beginning to the final stages of my doctoral journey. His continuous encouragement, critical insights and constructive advice have been invaluable throughout the entire research process.

I extend my thanks to the German Research Foundation (DFG) for their generous financial support, which made this research possible.

Starting my doctoral research in a new environment was initially a daunting experience, but the supportive atmosphere at the Chair of Applied Mechanics made all the difference. I am especially grateful to my dear friend Dr.-Ing. Prateek Sharma, whose help, insightful discussions and friendship were a constant source of motivation.

Finally, I am deeply grateful to my family—especially my wife—for their relentless support, boundless patience and unwavering faith in me. Their steadfast belief in my potential has been the driving force behind every step of this journey, and without it none of this would have been possible.

Saarbrücken, 2025 Arash Gordanshekan

Contents

1

Introduction

1.1 Motivation

The development and exploration of novel materials have always been at the forefront of engineering and scientific research. Among these, auxetic materials have attracted significant attention due to their unique mechanical properties, which include a negative Poisson's ratio, high energy absorption, high indentation resistance and large fracture toughness. The implications of this behavior are profound, offering potential advancements in a wide range of applications such as biomedical implants, vibration dampers, protective equipment and aerospace structures. Sheet metal, a fundamental component in manufacturing and structural engineering, presents an interesting candidate for auxetic transformation. By integrating auxetic properties into traditional sheet metal, we can unlock a new spectrum of mechanical behaviors that can significantly enhance performance under various loading conditions. Characterizing and modeling the mechanical behavior of auxetic sheet metal is imperative to understanding and harnessing these advanced materials. Accurate characterization ensures that the unique properties of auxetic sheet metals are well documented and can be consistently reproduced. A reliable

material model and its implementation in a FE software (simulation) can serve as an excellent alternative to experiments, resulting in significant time and cost savings.
In the current work, a comprehensive experimental and numerical investigation was conducted on auxetic rotating unit structures, including variations in the geometry parameters of the perforations, as well as different loading conditions. Furthermore, a macroscopic anisotropic elasto-plastic material model for auxetic sheets was developed derived from a corresponding micro-model. This was achieved through application of various experimental techniques including in situ characterization via Digital Image Correlation (DIC) and thermography, accompanied with various numerical approaches such as homogenization and implementation of periodic boundary conditions (PBCs), all within the framework of continuum mechanics theory. The methodology used to develop this material model can also serve as a general approach for other anisotropic perforated materials with other repetitive microstructural patterns.

1.2 Thesis Outline

This study, from the introductory chapter to the final conclusions, has been structured and organized into 8 chapters as follows:
After a brief introduction to the motivation, objectives and relevance of the present research in **Chapter 1**, a general overview of auxetic metamaterials is provided in **Chapter 2**. This chapter includes a literature review of typical auxetic structures such as re-entrant, chiral and rotating unit mechanisms, followed by a specific focus on auxetic sheet metals and their characteristic deformation behaviors. The engineering significance and application potential of such structures are also highlighted. In **Chapter 3**, detailed experimental investigations are presented. This includes the design and fabrication of auxetic samples with varying geometric parameters, such as aspect ratio, pattern size and orientation angle. The mechanical behavior is characterized through quasi-static uniaxial and biaxial tensile tests using advanced measurement techniques like Digital Image Correlation (DIC) and Infrared Thermography (IRT). The fundamentals of continuum mechanics relevant for the development of a material model are discussed in **Chapter 4**. This chapter introduces key concepts including kinematics, balance equations and constitutive relations, particularly for anisotropic elastic and plastic material behavior. In **Chapter 5**, fully resolved finite element simulations and

numerical homogenization methods are employed to analyze the deformation response of auxetic structures specially at the microscale. This includes the investigation of representative volume element (RVE), implementation of periodic boundary conditions and extraction of effective mechanical properties. The derivation of a macroscopic anisotropic elasto-plastic material model is carried out in **Chapter 6**. Based on the previously described numerical and experimental insights, a tetragonal elastic formulation is combined with a pressure-sensitive plasticity model, extended to account for anisotropy. The parameters of this model are based on the numerical simulations on the homogenized RVE. In **Chapter 7**, the implementation of the material model in ABAQUS® via a user-defined material subroutine (UMAT) is discussed. Numerical schemes and validation results are provided, demonstrating strong agreement with experimental observations. Finally, **Chapter 8** summarizes the key findings and contributions and potential directions for future research are proposed.

2

Auxetic Metamaterials

2.1 Auxetic Structures

Generally, a microstructure can be designed in several manners to achieve different mechanical behaviors at the macroscale and this is the concept embodied by the term metamaterials. Auxetic materials, derived from the Greek word αὔξητικός (auxetikos), meaning "that which may be increased", are a unique class of metamaterials that exhibit negative Poisson's ratios. This means that they exhibit an unusual property in which they expand laterally when stretched, instead of contracting like most materials. In contrast, under compressive loading, they exhibit lateral contraction [30, 70, 56].
From a continuum mechanics perspective, there is no strict requirement for the Poisson's ratio (ν) to be positive. However, materials with a negative Poisson's ratio are still a rare exception. Almost all isotropic materials exhibit a positive Poisson's ratio. Based on the principle that the strain energy of an isotropic elastic solid cannot become negative, it is deduced that the Poisson's ratio theoretically lies between -1 and 0.5. For anisotropic materials, the physically possible range is even broader. The upper limit, $\nu = 0.5$, corresponds to incompressible materials. For a smaller Poisson's

ratio, the volume increases under tensile loading and decreases under compressive loading. Therefore, a negative Poisson's ratio is always associated with some degree of compressibility in the material and can theoretically occur in isotropic materials with a very high shear modulus and a low elastic modulus.

Auxetic materials have been known for over a hundred years. The first description of auxetic behavior was made by Voigt in 1888 regarding pyrite [97]. However, interest in auxetic materials was renewed about 40 years ago by significant contributions from researchers such as Almgren (1985) [84], Lakes (1987) [56], Evans (1989) [30], and Alderson (1999) [3]. Recent developments in the field of auxetics can be found in the review articles by Stavroulakis [93], Evans & Alderson [31], and Prawoto [80]. These studies demonstrate that auxetic behavior can arise at different scales, both at the molecular level and at the macroscale. Pyrolytic graphite [97], α-cristoblaite [32] and some biological tissues [60] are examples of such naturally occurring molecular auxetics. Artificial auxetic materials, or the so-called man-made auxetics, are found much more frequently than natural ones, often as cellular materials such as honeycomb structures and foams [59].

All auxetic materials share the characteristic that their behavior is always based on a special internal structure. For example, a folded microstructure that unfolds under tensile stress can macroscopically lead to a material with a negative Poisson's ratio. This is referred to as non-convex microstructures with **re-entrant** mechanism [28, 53, 31] (See Fig. 2.1-a). Both two-dimensional planar and three-dimensional re-entrant structures are described in this context, see, for example, Shokri Rad et al. [82] or Wang et al. [98]. Another possibility involves so-called unrolling mechanisms or **chiral** structures. The deformation mechanism of auxetic chiral structures involves the unrolling of rigid or semi-rigid units (often resembling nodes or arms) connected by flexible ligaments or hinges. When these structures are stretched, the units unroll in a coordinated manner, leading to an overall expansion in both the longitudinal and lateral directions [4, 8, 9, 27, 65, 85](See Fig. 2.1-b). A third approach describes microstructures that are composed of rotating triangles and quadrilaterals. The deformation mechanism of auxetic **rotating units** structures relies on the rotation of interconnected rigid units or "nodes" around flexible hinges or joints. When the structure is stretched, these rigid units rotate relative to each other. Instead of the structure contracting laterally (as would happen in a conventional material), the rotation causes the connected units to push outward, leading to lateral expansion [19, 34, 38](See Fig. 2.1-c).

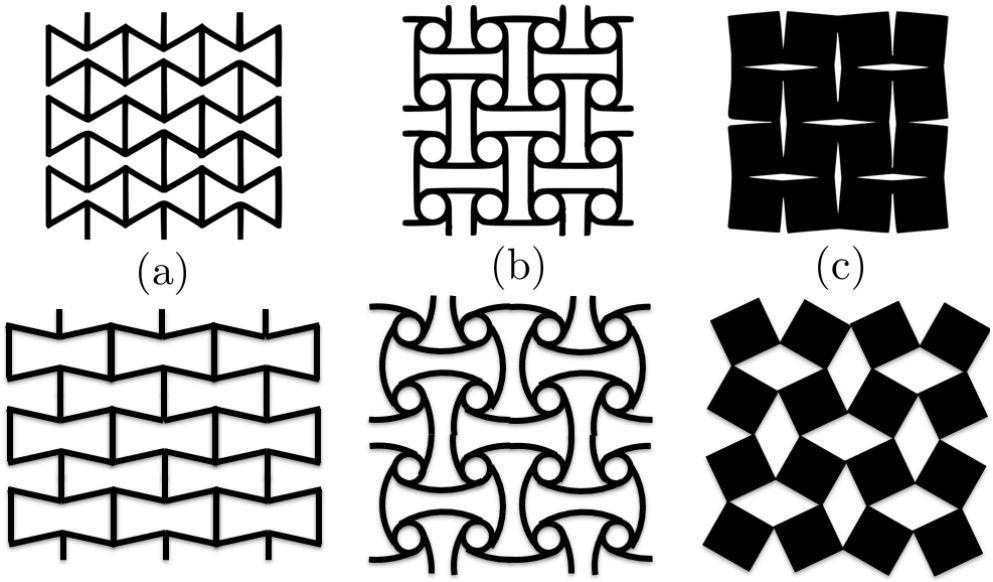

Figure 2.1: Typical auxetic structures; a) re-entrant ; b) chiral; c) rotating units. Top: undeformed state; bottom: deformed under vertical uniaxial tension.

Auxetic materials exhibit superior mechanical properties compared to conventional materials, including excellent indentation resistance, shear resistance, fracture toughness, and energy absorption [67, 33, 39, 56]. Their enhanced indentation resistance results from two key factors: high shear stiffness and the ability of auxetic materials to move toward the region of impact, increasing local density. Research has also shown that more energy is required to propagate cracks in auxetic materials, contributing to their greater fracture toughness [70]. In addition, auxetic materials offer improved damping and sound absorption properties [64, 102], making them ideal for applications where vibration reduction is essential to prevent fatigue under cyclic stresses [102].
The unique properties of auxetic materials make them suitable for a wide range of applications, particularly in industries such as automotive, aerospace, and marine [87, 33]. So far, there are only a few references in the literature to successful technical applications of auxetic materials and structures. For example, macroscopic auxetic structures have been used by Obrecht et al. [77, 76] to enhance load-bearing capacity in lightweight construction. The goal of these developments is to achieve high load-bearing capacity with the lowest possible weight. Due to their high energy absorption capacity and low density, it has also been proposed to use auxetic struc-

tures in lightweight construction as "crash absorbers" [33, 39]. In addition to lightweight construction applications, other potential uses are described by Evans & Alderson [31] and Stavroulakis [93]. For instance, safety vests made from auxetic fabrics can distribute the force of a projectile over a large area, thereby reducing its penetrating power. In sports applications, research has demonstrated potential benefits in comfort and protection gear [86]. In medical technology, the insertion of stents to keep blood vessels open can be made easier if the stents become thinner rather than thicker when subjected to lateral pressure.

2.2 Auxetic Sheet Metal

The auxetic structure investigated in this study is an auxetic sheet made of aluminum alloy (AlMg3) with rectangular perforations. The perforations are arranged orthogonally and are regularly repeated throughout the sheet in a continuous pattern. The perforations are cut out using a micro-water jet cutting machine, which is available at the Chair of Applied Mechanics (AM) at Saarland University and funded by DFG (Deutsche Forschungsgemeinschaft). The machine provides absolute precision, as well as the possibility of using the entire range of abrasive nozzles from 0.2 to 1.0 mm on the microcutting scale. Due to their deformation mechanism, these auxetic sheets belong to the group of auxetic "rotating units structures." In the next chapter, this behavior will be examined and discussed in more detail. As a result of the periodicity in the structure, a unit cell can be defined that repeats uniformly throughout the entire sheet in both the horizontal and vertical directions, as can be seen in Fig. 2.2.

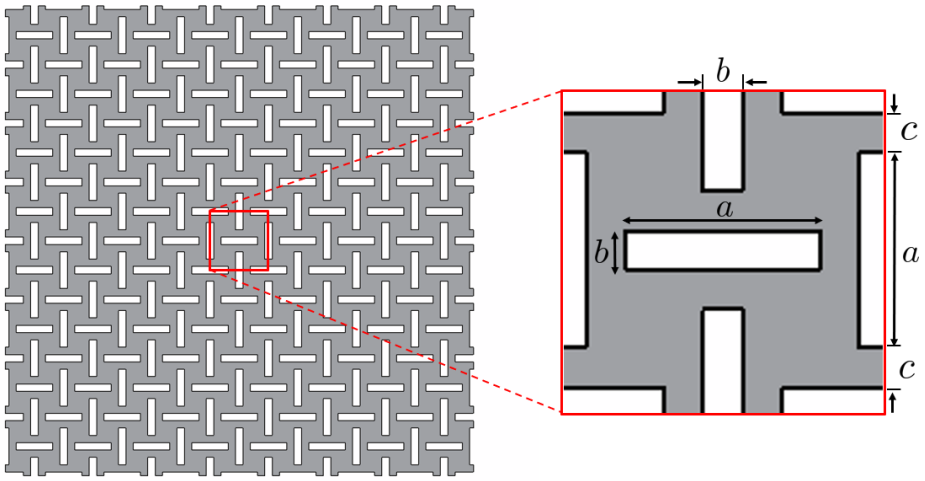

Figure 2.2: Auxetic sheet and the cut-out unit cell including geometry parameters

The mechanical behavior of such auxetic structures is mainly characterized by two key parameters, namely the volume fraction of the perforations or the so-called porosity (V_p) as well as the aspect ratios of the perforations (AR). To calculate the porosity, only a single unit cell needs to be considered due to the periodicity. The porosity and aspect ratio can be determined as:

$$V_p = 4\frac{A_p}{A_{uc}} = \frac{4ab}{(a+b+2c)^2} \tag{2.1}$$

$$AR = \frac{a}{b} \tag{2.2}$$

where a is the length, b the width and c the distance of the perforations. A_p and A_{uc} represent the area of a single perforation and the area of the unit cell, respectively.
It should be noted that the sheet exhibits auxetic behavior only in the plane with the corresponding pattern. The model is therefore a 2D model. In the third direction, conventional behavior is present, but this is not relevant in the following context.

3

Experimental Investigations

3.1 Fundamentals of Experimental Characterization

When a material is subjected to a load, deformation inevitably occurs. The material exhibits a certain resistance to this deformation which must be overcome by external or internal forces. The relationship between the external forces acting on the sample and the corresponding deformations typically represented in force-deformation diagrams or so-called force-displacement diagrams characterizes the mechanical behavior of the material. Depending on the type of external force applied and the resulting deformation, various testing methods are used, including tensile, compression, bending, torsion and shear tests. Each test type reveals specific aspects of the material's behavior under different forms of force and displacement, allowing for a comprehensive understanding of its performance and potential applications.

3.1.1 Uniaxial Tensile Test

The uniaxial tensile test is one of the most important material tests for characterizing metallic materials. Normally, it is completely sufficient for characterizing isotropic metallic materials. The method of tensile test on metallic materials at room temperature was standardized by ISO 6892-1. The test consists of stretching a sample with a defined shape and size by applying a uniaxial tensile load until failure to determine the desired mechanical properties. During the test, the applied force and the elongation (displacement) of the gauge length are captured. To ensure that the resulting force-displacement data reflect only material properties, independent of geometry, two new terms are defined, namely stress and strain. These represent force and displacement relative to the initial cross-sectional area and the initial length of the specimen, respectively, and are calculated through the following equations:

$$\sigma = \frac{F}{A_0} \tag{3.1}$$

$$\varepsilon = \frac{L - L_0}{L_0} = \frac{\Delta L}{L_0} \tag{3.2}$$

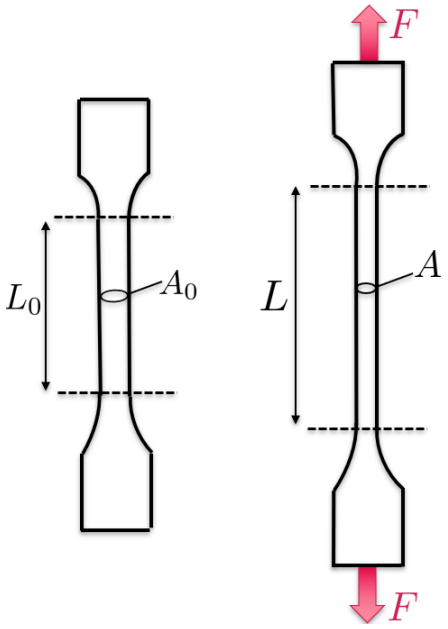

where σ and ε denote stress and strain, F applied force, ΔL elongation and A_0 and L_0 initial cross-sectional area and length, respectively. The calculated stress and strain from the uniaxial tensile test is then plotted as a so-called stress-strain curve, which is shown in Fig. 3.1.

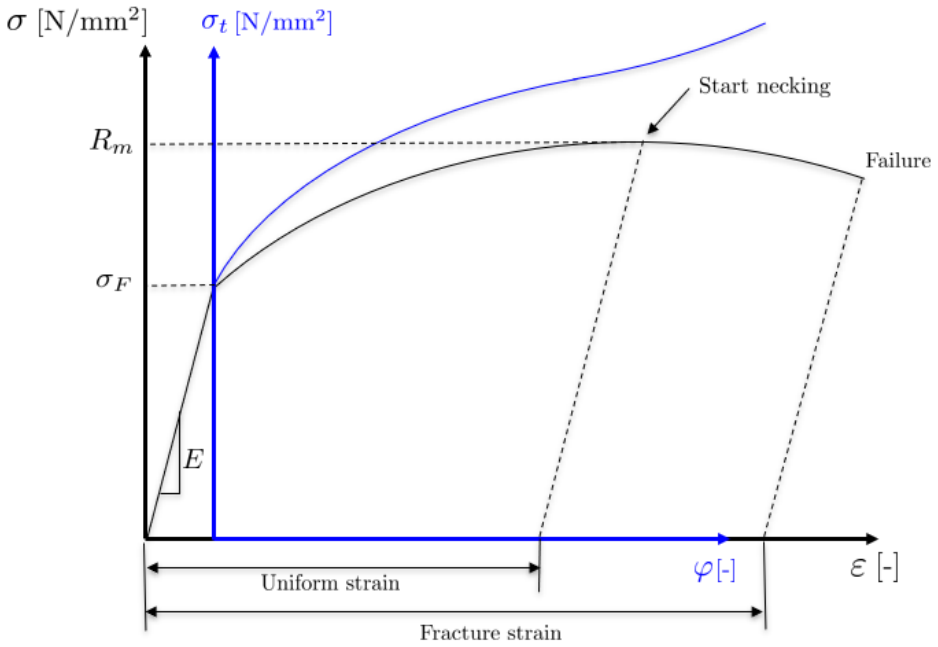

Figure 3.1: Schematic representation of a typical technical stress-strain curve (black) and the corresponding flow curve (blue) (E: Young's modulus; σ_F: Yield point; R_m: Tensile strength)

The stress-strain diagram is divided into an elastic region and a plastic region. In the elastic region, the behavior follows Hooke's law, represented by Young's modulus as the slope of the straight line. When the load is removed in this region, the elastic strain completely disappears. Once a specific critical stress for the material is reached, plastic deformation begins, which persists even after the specimen is unloaded. The transition from elastic to plastic behavior is marked by the yield stress or so-called yield point (σ_F). The plastic region can be divided into the uniform elongation phase and the necking phase. The transition between these two phases is identified by the tensile strength (R_m), which represents the maximum stress point in the stress-strain diagram. During the uniform plastic strain phase, the material undergoes hardening, driven microscopically by the movement and accumulation of dislocations. When the tensile strength is reached, localized necking starts, and further plastic deformation occurs only within the necked region. Since the reduction in the cross-sectional area in the neck exceeds the local hardening, this leads to a decrease in the stress in the diagram. Finally, when the fracture strain is reached, the specimen breaks and the test comes to an

end.
In addition to the technical stress-strain curve, the true stress-strain curve or the so-called yield curve can also be defined, where the true stress σ_t is plotted against the true strain or so-called logarithmic strain φ. In contrast to engineering stress, true stress is calculated based on the real-time value (current value) of the specimen's cross-sectional area, rather than on the initial value. The true stress and true strain are determined as follows:

$$\sigma_t = \frac{F}{A} \tag{3.3}$$

$$\varphi = ln(\frac{L}{L_0}) \tag{3.4}$$

The engineering (technical) and true stress and strain can be converted into each other using equations 3.5 and 3.6 :

$$\sigma_t = \sigma(1 + \varepsilon) \tag{3.5}$$

$$\varphi = ln(1 + \varepsilon) \tag{3.6}$$

It should be noted that the nominal stress-strain curve and the true stress-strain curve show small deviations only if small deformations are investigated. By formation of a localized necking zone, both curves diverge. The true stress-strain curve is mostly used in metal forming applications, as the elastic range of the material is relatively too small and not of interest compared to the plastic range and therefore can be neglected. Furthermore, in material modeling, when hardening behavior needs to also be mapped, the hardening parameters must be derived from the flow curve as well.
Another important material parameter to be determined by the uniaxial tensile test is the Poisson's ratio. This is defined as the negative ratio of transverse strain to axial strain. Figure 3.2 illustrates a rectangle in its undeformed state with dimensions dx and dy. Under uniaxial tensile loading, it deforms to new dimensions $dx + \Delta dx$ and $dy + \Delta dy$.

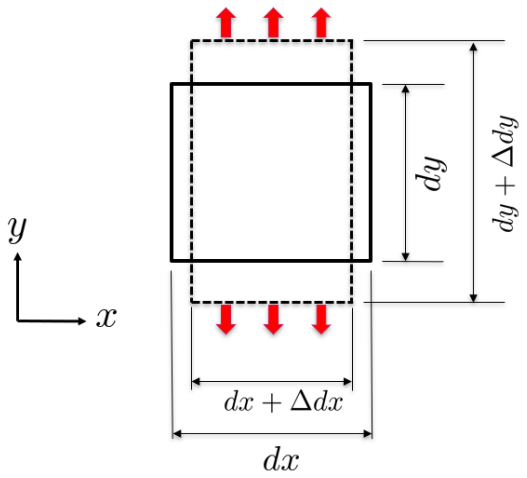

Figure 3.2: Schematic representation of the transvers strain and axial strain to determine of Poisson's ratio in 2D case for conventional material behavior.

In this case, the Poisson's ratio is calculated as follows:

$$\nu_{xy} = -\frac{\varepsilon_{xx}}{\varepsilon_{yy}} = -\frac{\Delta dx}{\Delta dy} \tag{3.7}$$

This means that when a body becomes thinner, Δdx becomes negative, resulting in a positive Poisson's ratio, like almost all conventional materials. However, in auxetic materials, which expand laterally under tensile loading, Δdx becomes positive, leading to a negative Poisson's ratio.

3.1.2 Biaxial Tensile Test

As discussed in the previous section, the uniaxial tensile test is sufficient in most cases to characterize metallic materials. However, this is mainly applicable to bulk metals with a fully homogeneous structure. For heterogeneous materials that display anisotropy (direction-dependent properties) and experience volume changes during deformation, additional tests beyond the uniaxial tensile test are required to accurately capture all material properties. This includes the biaxial tensile test, which is suitable for thin sheets or applications involving plane stress conditions. The biaxial tensile test and

its specimen are also standardized according to ISO 16842:2021(E) [1]. A typical biaxial tensile testing machine, as illustrated in Figure 3.3, includes two perpendicular axes, which can be operated either simultaneously or independently.

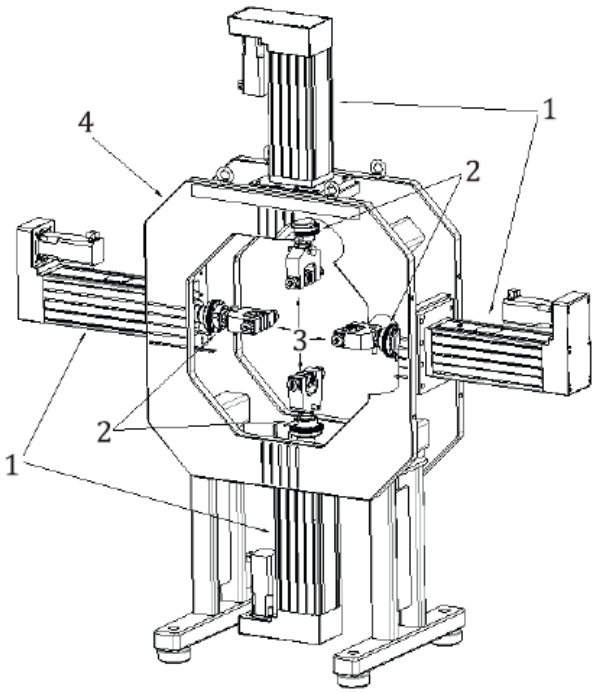

Figure 3.3: Typicall biaxial tensile testing machine, 1: electromechanical actuator; 2: load cell; 3: grips; 4: load frame [ISO-16842:2021(E)].

When both axes move simultaneously, this is known as a "balanced" or equibiaxial test. Balanced biaxial tests and tests where the axes move at different speeds (different strain rates) can induce unique multiaxial stress states in the sample, which cannot be achieved with uniaxial tensile tests. Such varied stress states are crucial for developing elastoplastic material models, particularly when the material exhibits complex behavior due to structural nonhomogeneity. This approach allows for the identification of multiple points on the corresponding yield surface, resulting in a more precise approximation of the material's behavior.
It should be noted that conducting reliable biaxial tests is a challenging task. In recent years, numerous studies have focused on improving the biaxial testing process, particularly the design of the specimen [42, 24, 35], which ultimately led to the development of the cruciform specimen outlined in ISO

16842:2021(E) [1], which is shown in Fig. 3.4.

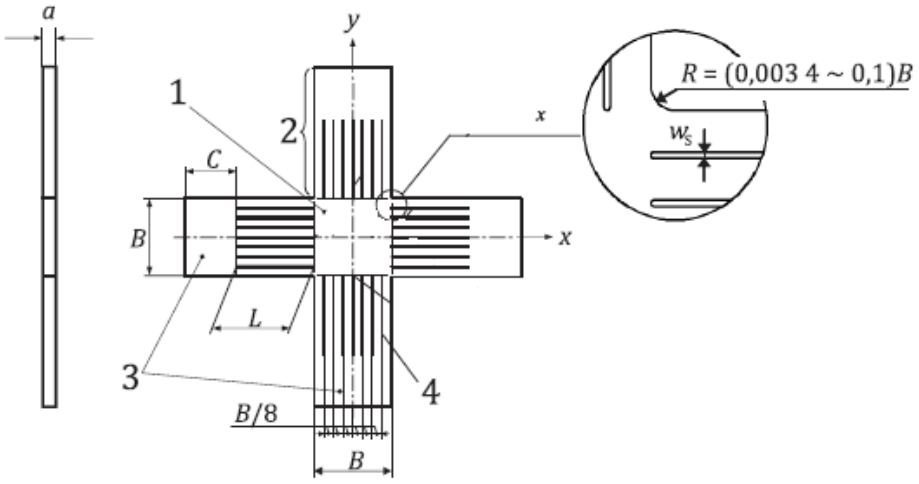

Figure 3.4: The modified cruciform specimen for biaxial tensile testing, 1) gauge area; 2) arm; 3) grips; 4) slit; a) thickness of a test piece; B) arm width; C) grip length; L) slit length; R) corner radius; ws) slit width [ISO 16842:2021(E)].

3.2 Characterization of Bulk AlMg3

The experiments were started with a displacement controlled and quasi-static uniaxial tensile test on a bulk AlMg3 sample at room temperature. The bulk sample is taken from the same AlMg3 sheet that will later be used to cut the corresponding auxetic sheets. The mechanical properties of the bulk sample provided the input values for the fully resolved FE-simulation of the associated auxetic sample. They also present basic values for later comparison with their auxetic counterparts. The resulting stress-strain curve is shown in Figure 3.5.

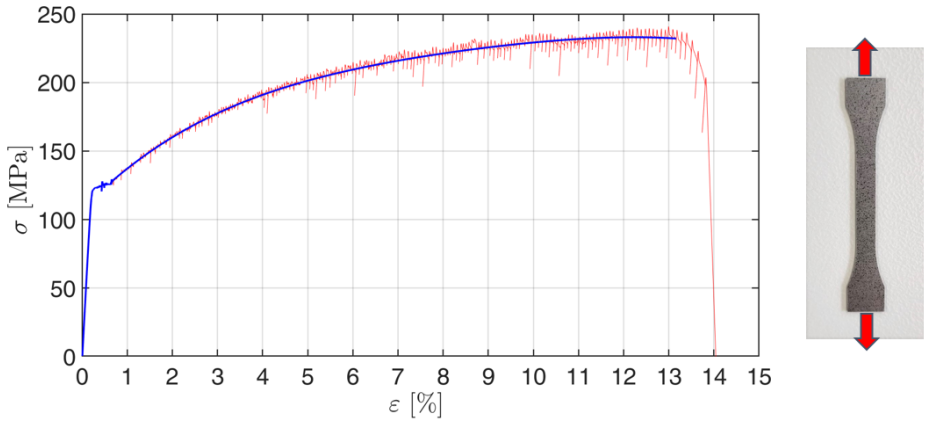

Figure 3.5: Stress-strain curve of the bulk AlMg3 sample with noisy experimental data (red) and low-pass filtered data (blue).

All important material parameters for bulk AlMg3 are summarized in Table 3.1, where E, ν, σ_F, R_m and A denote Young's modulus, Poisson's ratio, Yield stress, Ultimate stress and Fraction strain, respectively.

E	ν	σ_F	R_m	A
60.04 GPa	0.33	119.6 MPa	233.86 MPa	13.87%

Table 3.1: The most important material parameters of the bulk AlMg3 sample, identified from the experimental tests.

3.3 Auxetic Sample Design

3.3.1 Uniaxial Samples

To perform uniaxial tensile tests, the samples were designed as shown in Fig. 3.6. The sheets comprise an auxetic region at the center flanked by two bulk areas at the extremities, each with five holes to clamp the sample to the testing machine. To examine the existing anisotropy and to achieve a locally combined tension-shear stress state within the structure, the uniaxial specimens were designed and cut with different pattern orientation angles θ, namely with θ=0°, 15°, 30° and 45°.

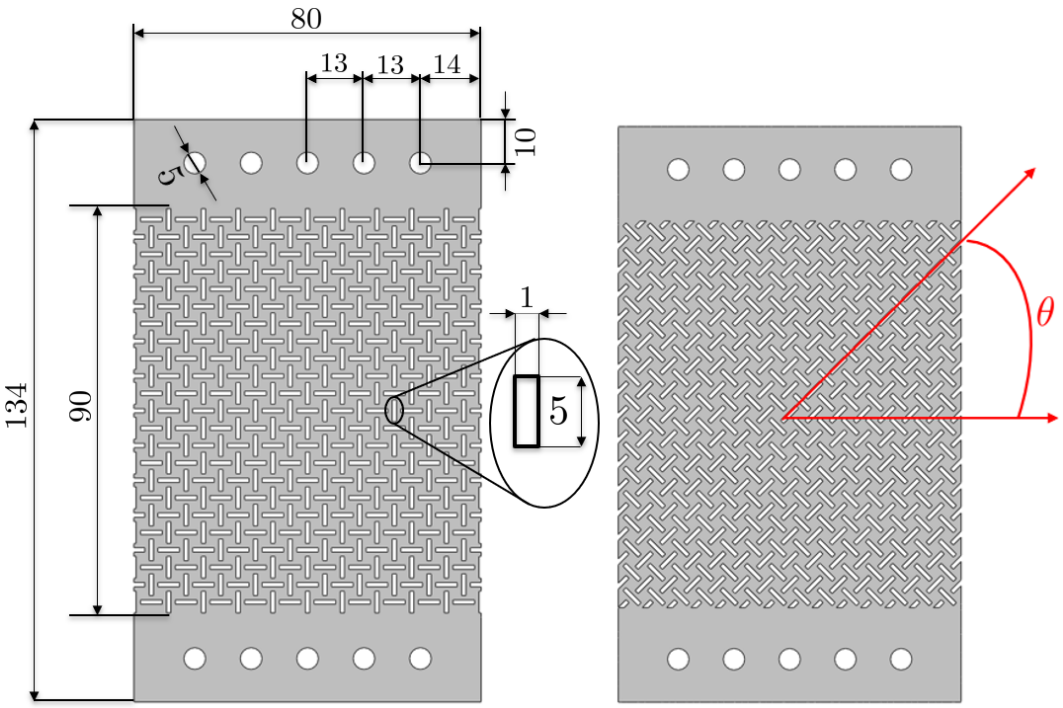

Figure 3.6: Refernce auxetic sheet sample with $AR = 5$ and geometry parameters $a = 5$, $b = 1$ and $c = 1$ (left) and the same sheet with pattern orientation angle (θ) (right), subject to uniaxial tensile tests. All dimensions are in mm.

3.3.2 Biaxial (Cruciform) Sample

Designing a suitable auxetic biaxial sample was significantly more challenging than a uniaxial one. To ensure reliable biaxial characterization, a cruciform specimen must yield fully symmetric strain and stress fields under equibiaxial loading. This is only achieved when (i) the specimen geometry is symmetric, (ii) both loading axes are driven uniformly, and (iii) boundary conditions and clamping are perfectly aligned. Under these conditions undesired stress gradients are minimized, and a homogeneous biaxial stress state can be established in the gauge area. A homogeneous biaxial stress state refers to a region within the specimen where the normal stresses in both principal loading directions are uniformly distributed and remain nearly constant over the gauge area. Another requirement was to minimize stress concentration at the corners between the arms to prevent premature failure of the sample in those areas. Various cruciform samples were designed for this purpose, inspired by ISO 16842:2021(E). The samples differed from each other in the number of slits in the arms, as well as in the completeness of the perforations at the boundaries. The samples were then numerically analyzed using commercial FE software ABAQUS® (Dassault Systems) by subjecting all samples to an identical balanced biaxial tensile test.

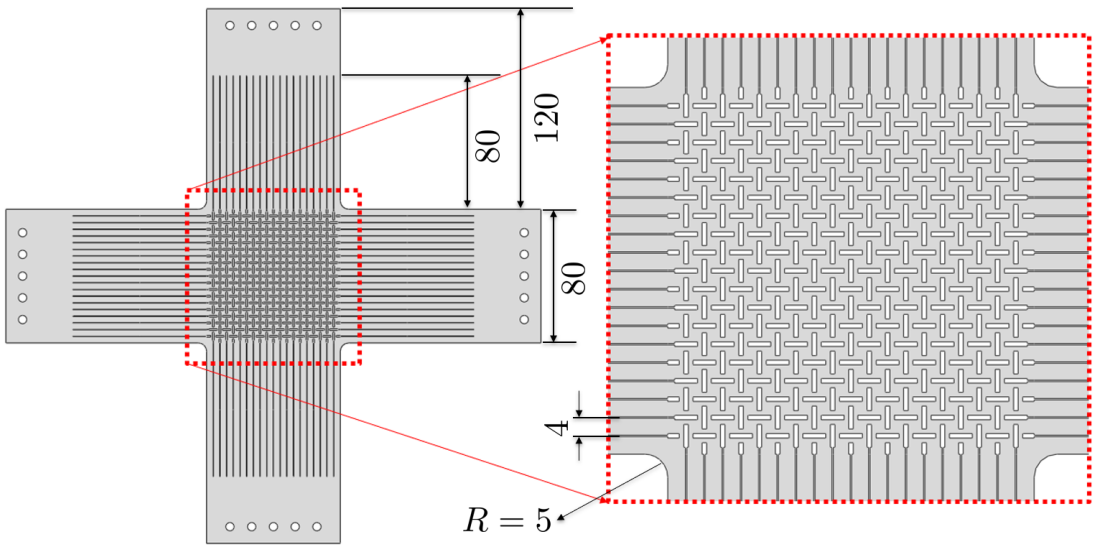

Figure 3.7: Auxetic cruciform sample with $AR = 5$ subject to biaxial tensile tests. All dimensions are in mm.

After evaluation of simulation results, it was determined that the sample in Fig. 3.7 best met the desired requirements compared to the other designed samples. The first noticeable feature of the simulation results under balanced biaxial loading with a total applied displacement of 6 mm in each direction, as shown in Fig. 3.8, is the clear symmetry of both the von Mises stress and the total displacement fields with respect to the x- and y-axes. The large number of slits in the arms helps to facilitate the rotation of the squares surrounded by the perforations at the edges during the pull, which leads to the elimination of boundary effects and to the minimization of stress concentrations at the boundaries.

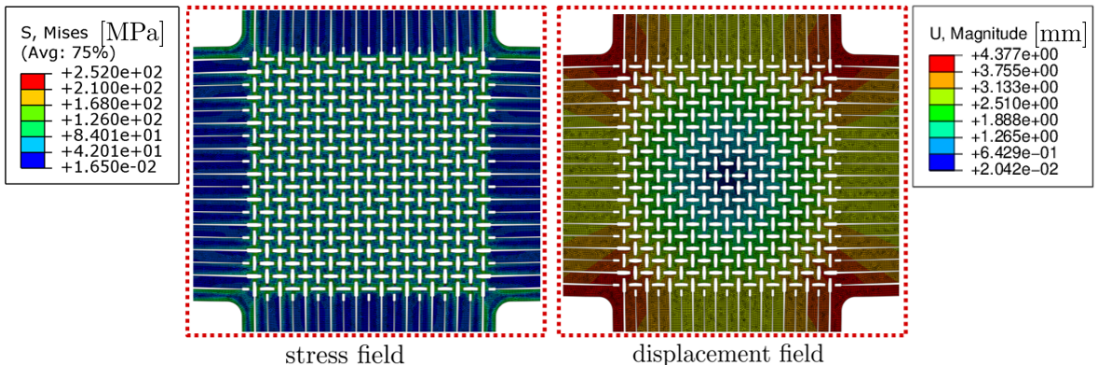

Figure 3.8: Simulation's results in terms of von Mises stress- and total displacement field subjected to the balanced biaxial tensile test.

3.4 Experimental Setup

The experimental studies for this thesis were conducted using a biaxial testing machine. This rig comprises four axes arranged at 90-degree angles to each other, each equipped with a linear motor. A pair of opposite axes can move synchronously, apart or together, and each is fitted with a force transducer capable of measuring up to 25 kN (ME Measuring Systems KD9363s, Hennigsdorf, Germany), allowing for uniaxial and biaxial specimen testing. Synchronous movement ensures that the center of the sample remains stationary. Specimen deformation is captured by an optical camera with a resolution of 1920x1200 pixels (Manta MG-235B, Allied Vision, Stadtroda, Germany), equipped with a 12.5 mm lens (Fujifilm HF12.5SA-1, Minato, Japan) for digital image correlation. The specimen's side is illuminated with an LED spotlight. Temperature fields are measured using a thermographic

camera with a resolution of 1024x768 pixels (Infratec Variocam HD, Dresden, Germany), which covers a spectral range of 7.5 - 14 µm. This camera faces the specimen's other side, directly across from the optical camera, with their optical axes intersecting at the specimen's center. A glass pane shields the thermographic camera from interfering with thermal radiation, such as from the environment or the optical camera. In addition, during tests, the area around the testing machine is covered with black fabric to minimize disturbances, especially since the expected temperature changes are minimal. Figures 3.9 and 3.10 schematically illustrate the setup subjected to the uniaxial and biaxial tensile tests, respectively. The PC connected to the testing machine controls the testing routine, triggers both cameras and records current positions and forces with each trigger. This enables for an effective later analysis of the measurements.

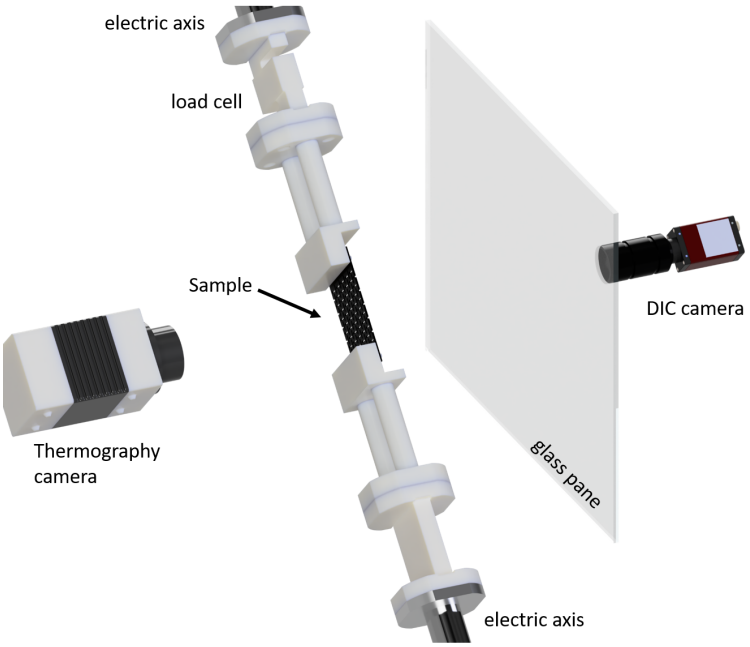

Figure 3.9: Experimental setup of an auxetic uniaxial tensile sample (black), clamped on two sides of one axes. Thermal and optical cameras are aligned to the center of the sample.

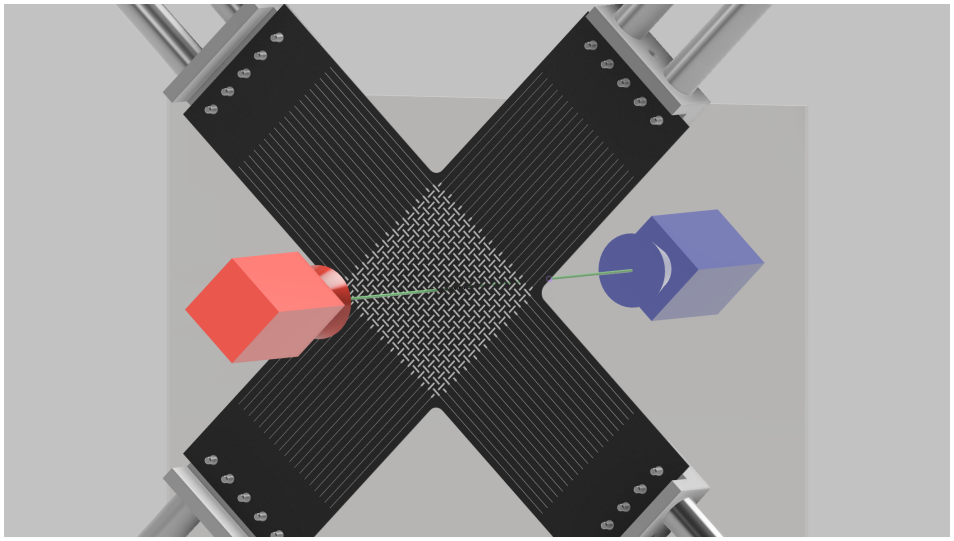

Figure 3.10: Experimental setup of an auxetic biaxial tensile sample (black), clamped on all four sides by actuators at right angles. Thermal imaging (red) and optical (blue) cameras are aligned to the center of the sample (green line).

3.4.1 Methods

Infrared thermography (IRT), commonly referred to as thermography, is a non-invasive imaging technique that captures the infrared radiation emitted by objects to ascertain their temperature distribution. This technique is extensively utilized in materials science due to its capability to deliver real-time thermal images of surfaces under various conditions. Digital Image Correlation (DIC) is another robust non-contact optical method employed to measure full-field displacements and strains on material surfaces. DIC functions by analyzing images of the material surface taken before and after deformation, facilitating the computation of displacement fields and strain maps. To enhance deformation tracking, the sample surface must be coated with a speckle pattern. When used in conjunction with thermography, DIC offers a thorough insight into the thermomechanical properties of materials. The integration of IRT and DIC has been extensively explored in the literature for its numerous benefits [20, 89, 61].

For example, the combination of these techniques allows the simultaneous measurement of temperature and strain fields, providing a more detailed

analysis of the behavior of the material under various loading conditions.

3.4.2 Sample Preparation

Following the initial preparation of the samples with their respective patterns by waterjet cutting, the samples undergo a cleaning process. This cleaning involves the use of an ultrasonic bath with isopropanol, ensuring the removal of any debris or contaminants that might have adhered during the cutting process. This step is crucial in preparing the surface for subsequent treatments and measurements. Given the specific requirements for surface treatment imposed by DIC and IRT techniques, each side of the sample is coated differently. For the side intended for DIC, a homogeneous background with a stochastically distributed speckle pattern is necessary. To achieve this, we first applied a white primer (Maston, Veikkola, Finland) to create a uniform base. Subsequently, a black Color Spray Paint (Maston, Veikkola, Finland) is used to add the speckle pattern and the speckles must be distributed stochastically and as finely as possible on the surface to achieve higher resolution. In order to have the correct gray value contrast, the ratio of 30%-black 70%-white should be kept. This contrasting color scheme enhances the accuracy of the DIC by facilitating the tracking of deformation [58, 63, 26].

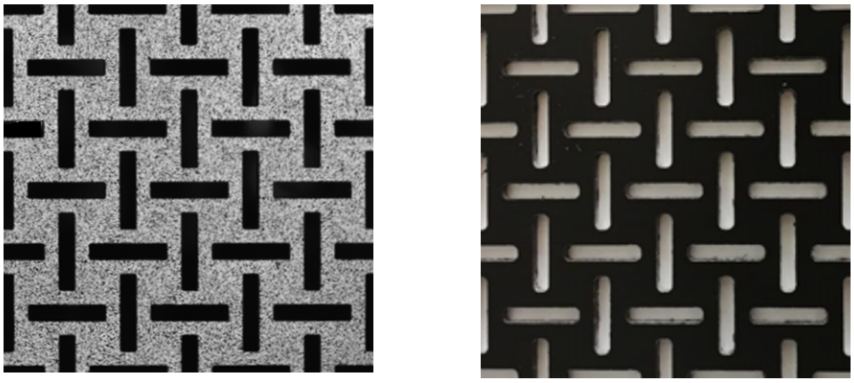

Figure 3.11: The side of the sample intended for DIC (left), the side of the sample intended for thermography (right).

On the side intended for thermography, a nonreflective surface with high emissivity is advantageous. For this purpose, the surface is coated with

Metal Expert Heat Resistant Metal Spray Paint in black (Rust-Oleum Europe, Zelem, Belgium). Preliminary tests were conducted to determine the emissivity of this coating at room temperature. These tests revealed an emissivity value $\epsilon = 0.964$, indicating the suitability of the coating for accurate thermographic measurements [96, 103].

3.5 Deformation Mechanism and Properties

To investigate the deformation mechanism of the auxetic sheet metal, a quasi-static, strain-controlled uniaxial tensile test was carried out using the in-house developed biaxial test rig (described in detail in 3.4) at room temperature, with a strain rate of $\dot{\varepsilon} = 0.0025\ s^{-1}$. For this purpose, an auxetic sheet (reference auxetic sheet) was used with geometry parameters of $a = 5$mm, $b = 1$mm and $c = 1$mm as shown in Fig. 2.2 and a thickness of 1mm. These parameters result in an aspect ratio $AR = 5$ and a porosity $V_P = 31\%$ according to equations 2.2 and 2.1, respectively. As discussed in section 2.1, the auxetic structure examined in this research falls under the category of "rotating unit structures" due to its unique deformation mechanism. As illustrated in Fig. 3.12, when the auxetic sheet is subjected to tension, the squares surrounded by perforations rotate while preserving their original shape. To examine this behavior in greater detail, a unit cell located at the center of the sample was analyzed during the uniaxial tensile test. The central unit cell was chosen because the edge effects have the least impact on the deformation behavior in that region. The local displacement field and the strain field of the unit cell were tracked from the beginning up to 10% global strain via DIC, as shown in Fig. 3.13.

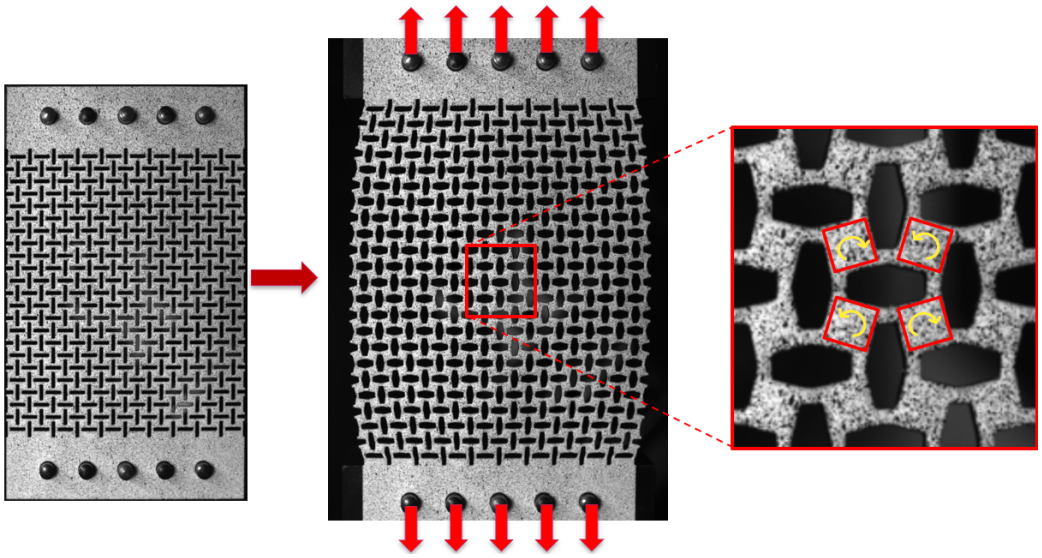

Figure 3.12: Representation of rotating squares responsible for the auxetic behavior in deformed state.

The resulting strain field illustrated in Fig. 3.13 demonstrates that the squares remain undeformed throughout the test. The calculated local principal strains, ε_1 and ε_2, within the squares are zero, confirming that they undergo a pure rigid body rotation during the test. Actually, the deformation occurs only in the struts between the perforations, which enable the rigid rotation of the squares during the experiment in a way that allows the sheet to expand in both directions, resulting in the characteristic auxetic behavior of the sheet metal.

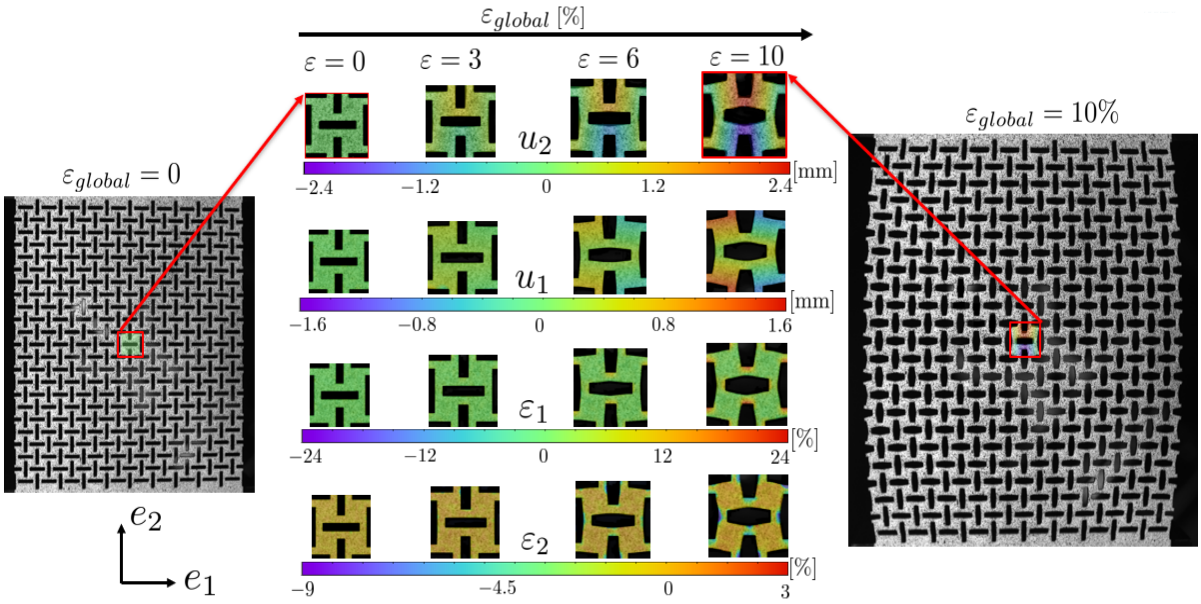

Figure 3.13: Local displacements and principal strains of the unit cell at the center of the sheet during the tensile test until 10% global strain using DIC.

The next step involved determining the global (effective) stress-strain curve from the uniaxial tensile test. For greater accuracy, the global strain, which refers to the elongation of the entire sheet, was calculated based on the total displacement measured with DIC, rather than using the machine displacement. In this context, the global stress also represents the total force exerted by the machine on the reference surface, defined by the sheet's width. The special feature of the resulting stress-strain curve plotted in Fig. 3.14 is the smooth transition from the linear elastic to the plastic regime, without showing any Lüder strain, in contrast to the corresponding bulk AlMg3. The fact is that the plasticized regions are so small that the effects are eliminated or vanish at the macroscale. In addition, the curve exhibits an almost linear hardening trend up to the fracture. No reliable statement can be made about the resulting elongation at fracture, as this depends strongly on edge effects, sheet size and the microstructure's fineness. Finally, the resulting most important material properties such as Young's modulus and yield point were determined from the curve and are shown in Tab. 3.2.

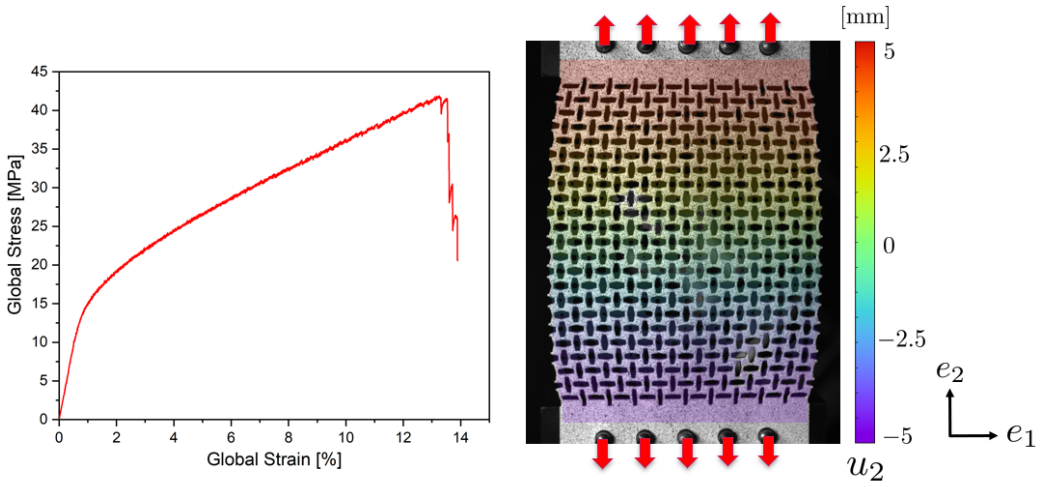

Figure 3.14: Global stress-strain curve (left) and local displacement field (u_2) corresponding to the tensile direction using DIC (right).

In order to determine the effective Poisson's ratio as the negative quotient of transverse strain to the axial strain within the elastic regime, the displacement field of a 2x2 unit cells at the center of the sheet was considered. The 2x2 unit cells at the center of the sheet is chosen because this region is the least influenced by edge effects. Although the displacement field of the central unit cell in Fig. 3.13 was captured very well, the 2x2 unit cells provided a more accurate basis for this analysis, as it was later identified (in the simulation section) as the correct representative volume element (RVE) for this auxetic structure.
As shown in Fig. 3.15, the local displacement field of the 2x2 unit cells was determined using DIC regarding both directions during the experiment. The transverse strain ε_{11} and the axial strain ε_{22} were obtained from the displacement fields in both directions by dividing the average relative displacements of all measurement points along the RVE edges by their corresponding initial lengths, according to equation 3.7.

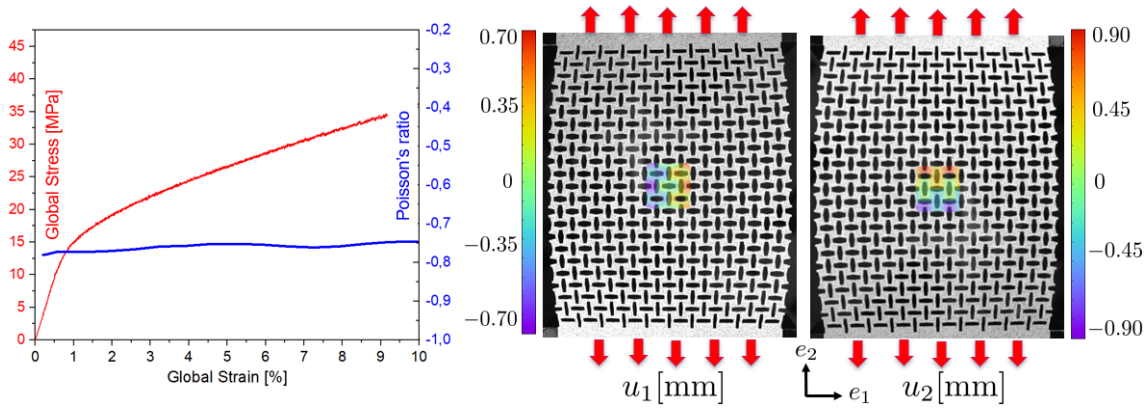

Figure 3.15: Local Poisson's ratio evaluated by a 2x2 unit cell in the center of the sheet and plotted as a function of the global strain using DIC. u_1 and u_2 refer to the displacement field in both directions.

To ensure that the determined Poisson's ratio refers only to the elastic region, the calculated Poisson's ratio was plotted as a function of global strain together with the corresponding stress-strain curve (see Fig. 3.15). This allowed only for the value of the Poisson ratio within the elastic range to be considered, resulting in a Poisson ratio $\nu = -0.77$ up to $\varepsilon_{global} = 0.6\%$.
Finally, all important material parameters for the auxetic structure with an aspect ratio $AR = 5$ and a porosity $P = 31\%$ extracted from uniaxial tensile test are summarized in Table 3.2, where E, ν, σ_F, R_m and A denote Young's modulus, Poisson's ratio, Yield stress, Ultimate stress and Fraction strain, respectively.

E	ν	σ_F	R_m	A
1750 MPa	-0.75	14.4 MPa	41.5 MPa	14.9%

Table 3.2: The most important material parameters of auxetic sheet with $AR = 5$.

3.6 Variation of Pattern Size

After detailed analysis of the mechanical behavior of the auxetic sheet with an aspect ratio of $AR = 5$, this section examines how the size of the pattern affects the overall mechanical properties. For this purpose, an auxetic sheet with the same aspect ratio and porosity but with varying pattern sizes was designed, as illustrated in Fig. 3.16. The second sheet is defined by the geometry parameters $a = 10$ mm, $b = 2$ mm and $c = 2$ mm, which result in the same aspect ratio ($AR = 5$) and porosity ($V_P = 31\%$) as the reference sheet according to the equations 2.2 and 2.1.

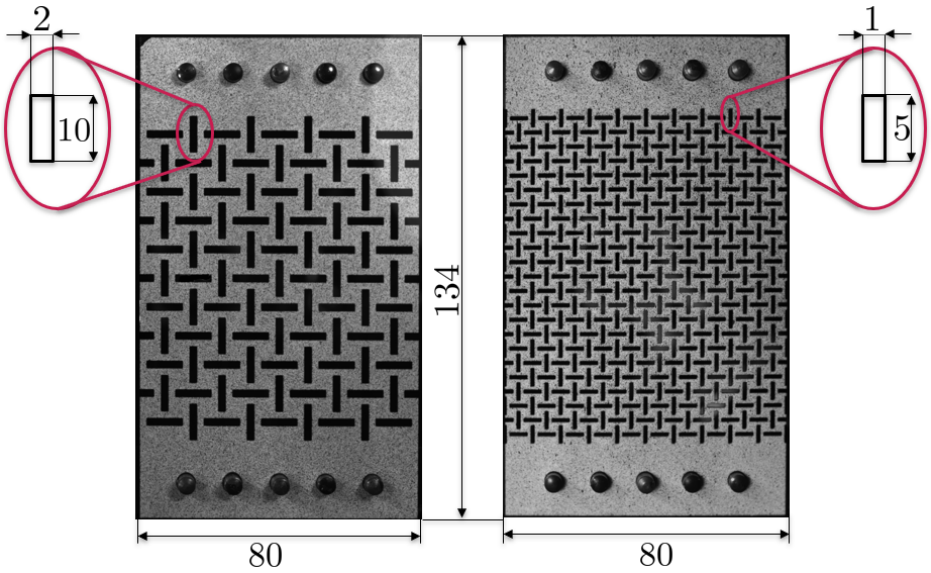

Figure 3.16: Auxetic sheets with the same aspect ratio $AR = 5$ and porosity $V_P = 31\%$ and different pattern size.

Quasi-static uniaxial tensile tests with the same test parameters were carried out on the samples. As shown in the stress-strain curve in Figure 3.17, the two sheets exhibit nearly identical mechanical properties. The only distinction lies in the fracture strain, where the sheet with the coarser pattern fails sooner than the reference sheet. This phenomenon can be interpreted to mean that the finer pattern can minimize the harmful edge effects. This is actually due to how far the rotating squares near the top and bottom edges can rotate.

Actually, by refining the pattern, we allow the rotating squares on edges to rotate even further, leading to a greater fracture strain while maintaining the same effective transverse strain.

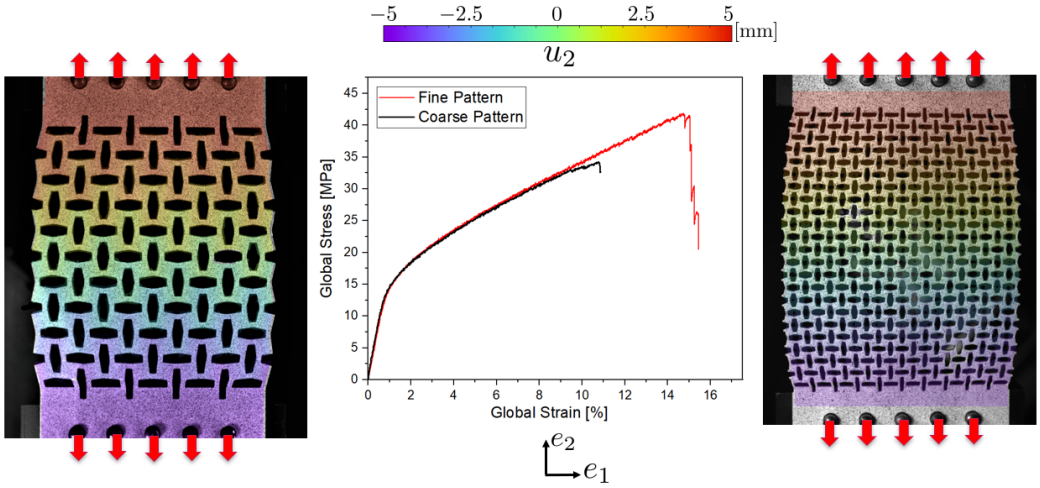

Figure 3.17: Stress-strain-curve and local displacement field (u_2) of the auxetic sheets after ca. 10% global strain with the same aspect ratio $AR = 5$ and porosity $V_P = 31\%$ and different pattern size.

3.7 Variation of Aspect Ratio (AR)

Following the discussion on the influence of pattern size in the previous section regarding the auxetic sheet with aspect ratio of $AR = 5$, this section examines how the variation of aspect ratio affects the mechanical behavior of auxetic rotating unit structures with rectangular perforations with the same amount of porosity $V_P = 31\%$. To achieve this, two additional auxetic sheets with different aspect ratios were designed and cut, complementing the previously studied auxetic sheet with an aspect ratio of $AR = 5$. As illustrated in Fig. 3.18, the first sheet has the geometry parameters of $a = 4$ mm, $b = 1.25$ mm and $c = 1.375$ mm, resulting in an aspect ratio of $\boldsymbol{AR = 3.2}$, while the other sheet has the geometry parameters of $a = 6.25$ mm, $b = 0.8$ mm, and $c = 0.5$ mm, which yields an aspect ratio of $\boldsymbol{AR = 7.8}$.

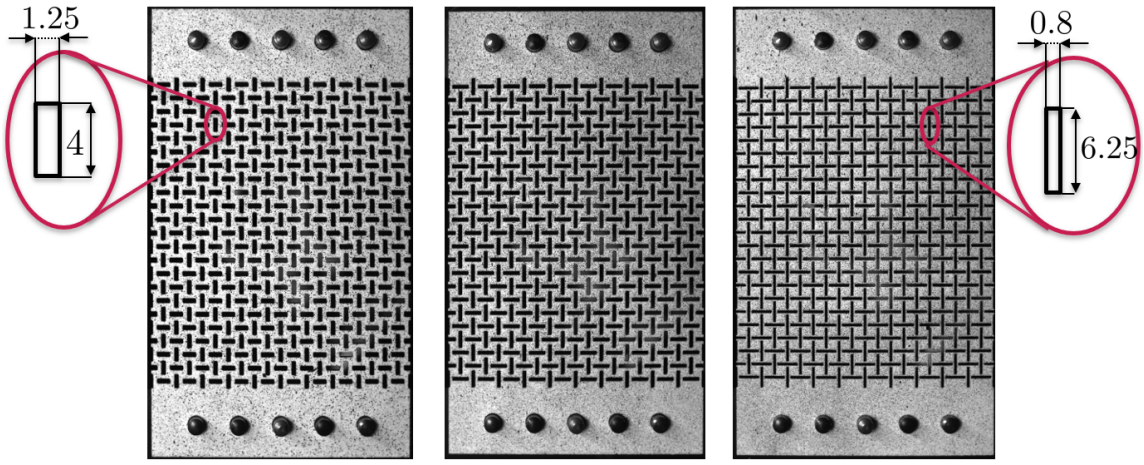

Figure 3.18: Auxetic sheets with different aspect ratios from left to right: $AR = 3.2$, $AR = 5$ and $AR = 7.8$. The dimensions are in mm.

Quasi-static uniaxial tensile tests were performed on the sheets. The deformed auxetic sheets after approx. 10% global strain for sheets with aspect ratios of $AR = 3.2$ and $AR = 7.8$ are shown in Figures 3.19 and 3.20 respectively. At first glance, even without analyzing the DIC results, it is evident that the sample with $AR = 3.2$ shows less auxetic behavior (lower transverse strain) compared to the sample with $AR = 7.8$. To accurately determine the effective Poisson's ratio, the displacement field of the 2x2 unit cells at the sheet's center was examined using DIC, as previously done for the reference sheet with an aspect ratio of $AR = 5$. To calculate the transverse and axial strains, the relative displacement of all measurement points on the edges was divided by the corresponding initial length, according to equation 3.7.
Finally, the values of Poisson's ratios (ν) for all sheets are shown in Tab. 3.3, which increases continuously in magnitude as the aspect ratio rises.

AR	E	ν	σ_F	R_m	A
3.2	2500 MPa	−0.55	34.4 MPa	73.5 MPa	15.7%
5	1750 MPa	−0.75	14.4 MPa	41.5 MPa	14.9%
7.8	620 MPa	−0.95	4.8 MPa	14.5 MPa	17.2%

Table 3.3: The most important material parameters of auxetic sheet with different Aspect ratios (AR).

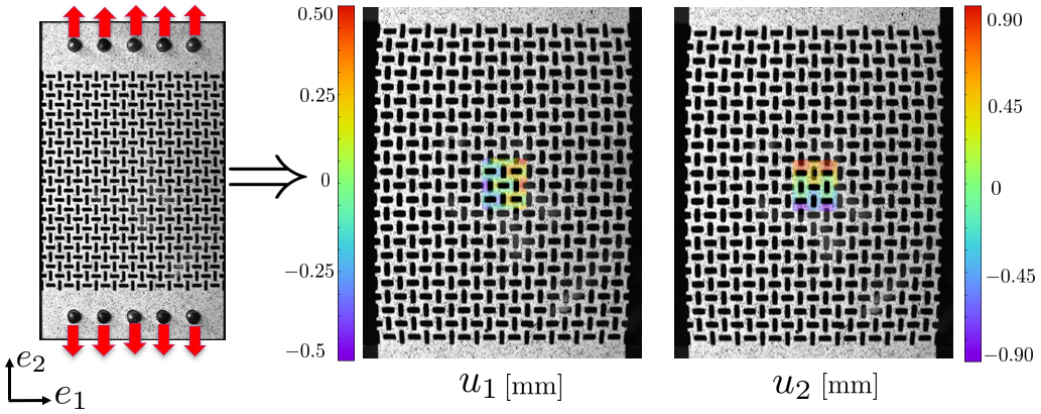

Figure 3.19: The deformed auxetic sheet with $AR = 3.2$, subjected to uniaxial tensile test at approximately 10% global strain, including DIC evaluations of the displacement field for the 2x2 unit cell at the center.

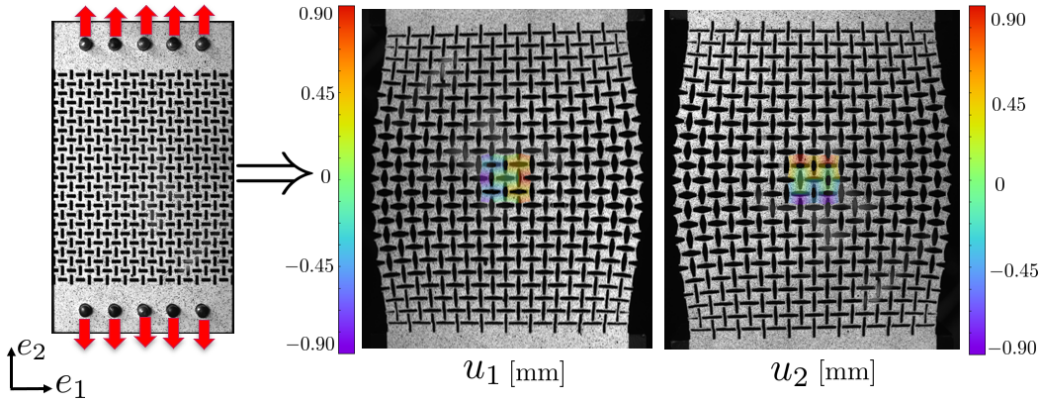

Figure 3.20: The deformed auxetic sheet with $AR = 7.8$, subjected to uniaxial tensile test at approximately 10% global strain, including DIC evaluations of the displacement field for the 2x2 unit cell at the center.

Interestingly, as shown in figure 3.21, the corresponding global stress-strain curves show significant differences, despite all sheets being made of the same material (AlMg3) and having the same porosity ($V_P = 31\%$). This fact is due to how much the squares surrounded by the perforations can rotate during loading. As can be seen from the stress-strain curves illustrated in figure

3.21, the sample with $AR = 3.2$ possesses the highest stiffness and strength, while showing the lowest auxetic behavior compared to the other two samples with larger AR.

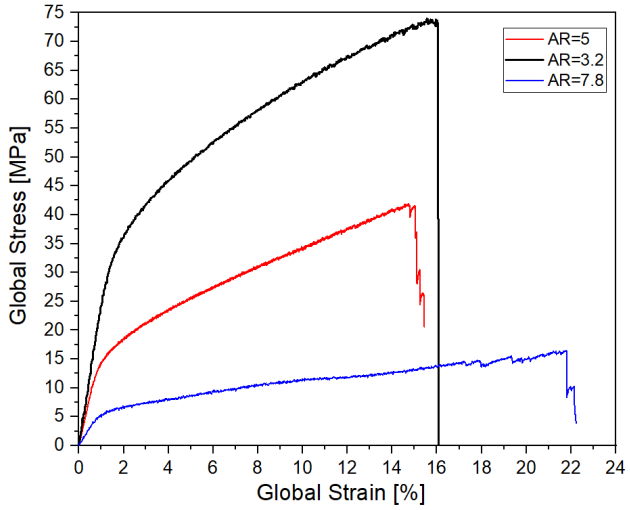

Figure 3.21: Stress-strain curves of the auxetic sheets with different aspect ratios (AR).

This observation can also be interpreted in another way, namely the geometry parameter c (distance between perforations) significantly influences the resulting mechanical properties. The results indicate that a lower value of the parameter c corresponds to improved auxetic behavior and reduced material strength. However, to achieve the same porosity, the aspect ratio and parameter c are related in such a way, that as the aspect ratio $AR = \frac{a}{b}$ increases, the value of c must necessarily decrease according to the equation 2.1, resulting in a greater auxetic effect, i.e. auxetic effects and strength are strongly coupled by the microstructure.
Finally, all important mechanical material parameters regarding auxetic sheets with different aspect ratios (AR) were calculated and presented in Table 3.3, where E, ν, σ_F, R_m and A denote Young's modulus, Poisson's ratio, Yield stress, Ultimate stress and Fraction strain respectively.

3.8 Variation of Pattern Orientation Angle (θ)

This section discusses how the orientation angle of the patterns affects the mechanical properties of auxetic sheets with rectangular perforations. For comparable results, the reference auxetic sheet with an aspect ratio of $AR = 5$ and a porosity of $V_P = 31\%$ was also considered here. The auxetic sheets vary only in the orientation angle of the pattern (θ), which represents the inclination of the pattern relative to the horizontal axis, as illustrated schematically in Figure 3.6. The primary goal of designing auxetic sheets with varying pattern orientations is to gain an initial understanding of the existing anisotropy in the structure. Anisotropy refers to material properties that vary with direction, a characteristic often found in heterogeneous structures. To achieve this, in addition to our reference sheet, three other sheets with the same aspect ratio $AR = 5$ and with orientation angles of 15°, 30° and 45° were designed and cut, as shown in Figure 3.22.

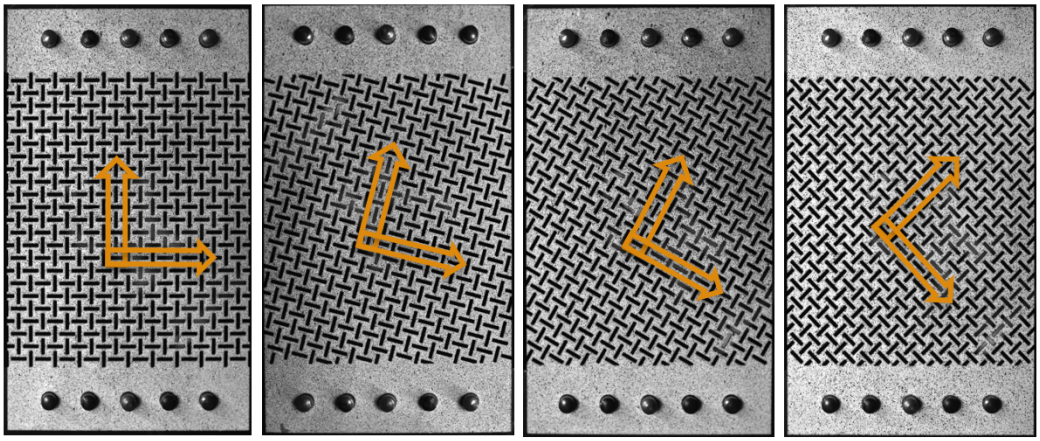

Figure 3.22: Auxetic sheets with the same aspect ratio $AR = 5$ and different pattern orientation angel (θ).

Each sheet was then subjected to quasi-static uniaxial tensile test using identical test parameters, applied up to 8% global strain. After evaluating the local transverse displacements of 2x2 unit cells at the center of the sheets via DIC, it was observed that with increasing orientation angle (θ), the expansions of the sheets or, in other words, the auxetic effect in the sheets

decreases, as can be seen in Figure 3.23. Evaluating the 2×2 unit cells at the center of the sheet rather than the entire sheet offers the advantage that these cells will later be defined as the RVE of the auxetic structures (see Section 5.4.3). Additionally, their central position minimizes the influence of edge effects.

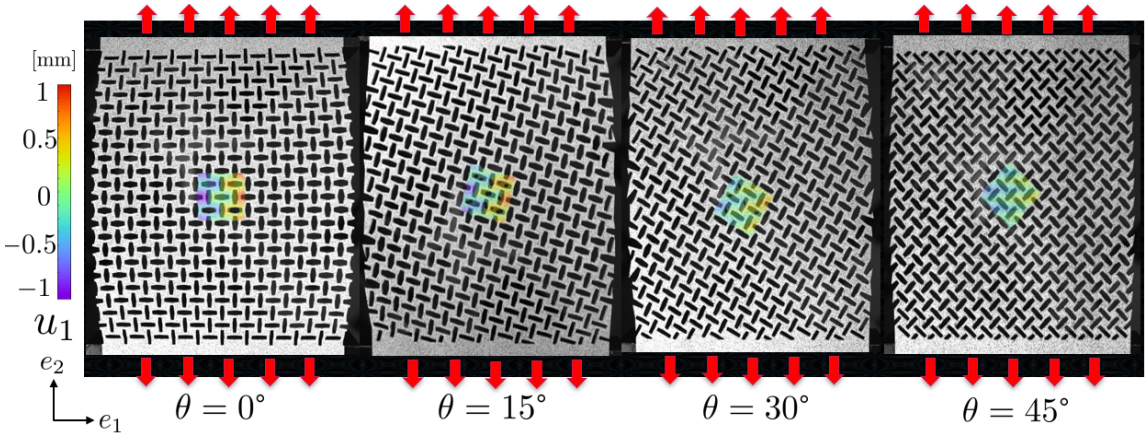

Figure 3.23: Local displacement fields (u_1) of 2x2 unit cells in center of the sheet for auxetic sheets with $AR = 5$ at various orientation angel (θ) after 8% global strain, evaluated by DIC.

To further investigate the impact of angle on the overall mechanical behavior of the auxetic sheets, the corresponding stress-strain curves were plotted and are presented in Figure 3.24.

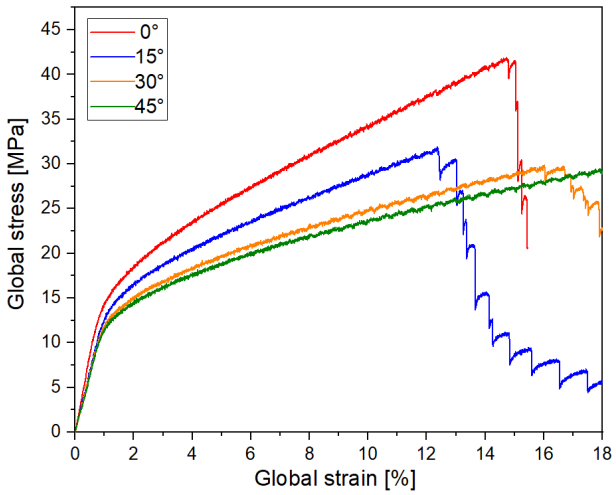

Figure 3.24: The stress-strain curves of auxetic sheets with $AR = 5$ at various pattern orientation angels (θ).

As can be seen in Figure 3.24, with increasing orientation angle (θ) the corresponding Young's modulus and yield strength decrease, indicating that the strength of the sheets continuously decreases. These results based on the fact that in sheets with a rotated pattern, the auxetic effect is localized. Consequently, as the angle increases, the proportion of global transverse strain calculated through transformation relations progressively decreases, resulting in a reduction of the overall effective auxetic effect. This phenomenon will be discussed in more detail, both qualitatively and quantitatively, in the following chapters.
Finally, the material properties of the sheets with different orientation angles are summarized in Table 3.4.

θ	E	ν	σ_F	R_m	A
0°	1750 MPa	−0.75	14.4 MPa	41.5 MPa	14.9%
15°	1680 MPa	−0.66	13.8 MPa	31.8 MPa	12.3%
30°	1510 MPa	−0.53	12.4 MPa	29.8 MPa	16%
45°	1255 MPa	−0.32	10.5 MPa	31.5 MPa	18.1%

Table 3.4: The most important material parameters of auxetic sheets with $AR = 5$ at various pattern orientation angels (θ).

3.9 Biaxial Tensile Tests

This section discusses the results of the biaxial tensile tests on the reference auxetic sheet with aspect ratio $AR = 5$. The design and fabrication of the auxetic biaxial specimen used here to perform the biaxial tensile tests has already been discussed in detail in Section 3.3.2. The experiments were carried out at three different rates of $\dot{\varepsilon}_{11}/\dot{\varepsilon}_{22}$, where $\dot{\varepsilon}_{11}$ represents the strain rate along the e_1 axis and $\dot{\varepsilon}_{22}$ the strain rate along the e_2 axis.
The test with $\dot{\varepsilon}_{11}/\dot{\varepsilon}_{22} = 1$, also known as the balanced biaxial tensile test, is carried out with both axes at the same speed, keeping the center of the sample stationary, as shown in Fig. 3.25. This configuration results in a fully symmetrical total displacement field relative to both axes. The total strain shown in Fig. 3.25 is a scalar value, derived from all in-plane strain components using the following relationship:

$$\varepsilon_{total} = \sqrt{\varepsilon_{11}^2 + \varepsilon_{22}^2 + 2\varepsilon_{12}^2} \tag{3.8}$$

Furthermore, the corresponding stress-strain curves for the e_1- and e_2-axes align perfectly on each other, confirming that the balanced biaxial tensile test was performed reliably.

Subsequently, the experiment was conducted with a strain rate ratio of $\dot{\varepsilon}_{11}/\dot{\varepsilon}_{22} = 1.5$. The larger displacement field along the e_1-axis, observed at the left and right edges of the sample, confirms a greater elongation in this direction compared to the e_2-axis. The corresponding stress-strain curves reveal an interesting pattern. While the curve along the e_1-axis follows a typical tensile load progression, the curve along the e_2-axis reflects a more complex behavior. Initially, both curves display linear elastic behavior up to approximately 1% total strain. Beyond this point, the e_2-axis curve shows an almost plateau behavior up to around 10% total strain before rising again. The slower strain rate along the e_2-axis allows the sample to demonstrate its auxetic effect, meaning expansion in the e_2-direction. The force generated by the sample's expansion nearly balances the force required by the testing machine to maintain the specified strain rate, creating the plateau in the curve. At some point, this balance is lost and the test machine must apply more force to maintain the strain rate, causing the curve to rise again.
In the third experiment with a strain rate ratio of $\dot{\varepsilon}_{11}/\dot{\varepsilon}_{22} = 2$ a similar scenario occurs as in the experiment with $\dot{\varepsilon}_{11}/\dot{\varepsilon}_{22} = 1.5$, with the key difference

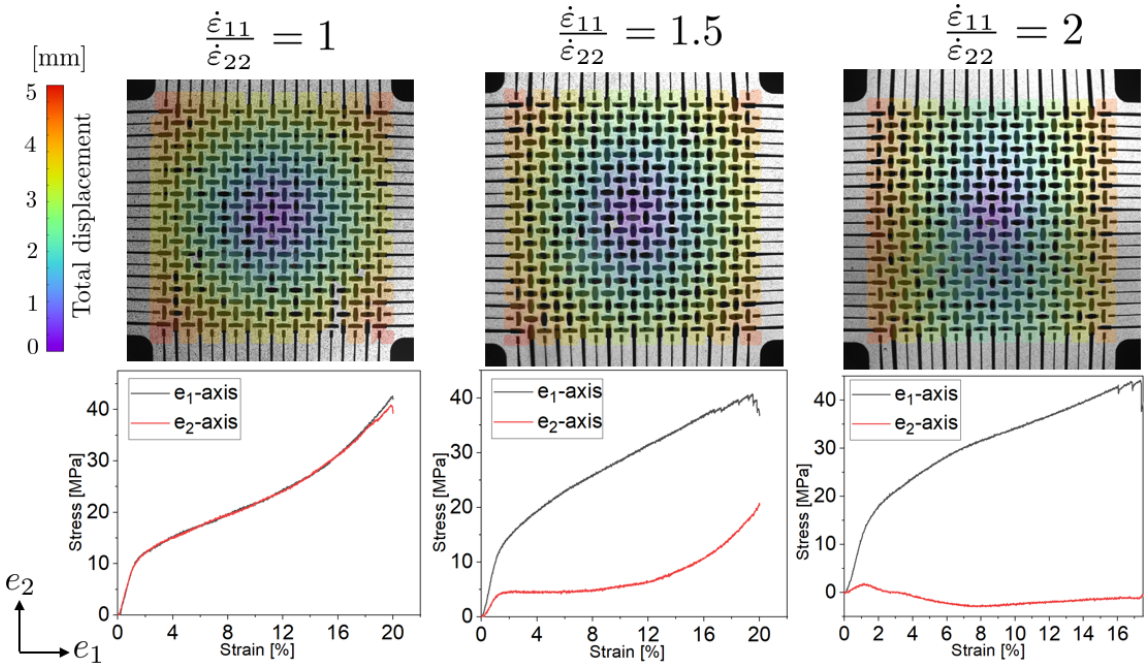

Figure 3.25: The global stress-strain curves of auxetic sheets with $AR = 5$ subjected to biaxial tensile tests at various strain rate ratios.

being that the strain rate induced by the auxetic effect along the e_2-axis is faster than the prescribed strain rate. This slower prescribed strain rate acts as resistance to further expansion in the e_2-direction, resulting in increased pressure on the sample in this direction, as shown in the stress-strain curve for the e_2-axis. This phenomenon can also be mildly observed in Figure 3.25, where the sheet shows a slight out-of-plane bending due to the induced pressure in the e_2 direction.
The results of biaxial tensile tests with varying strain rate ratios enabled conditions in the specimen to more accurately reflect real-world loading conditions, providing insight into how the auxetic sheet responds to these loads. Furthermore, the stress-strain curves obtained from the biaxial tests can serve to validate the subsequently developed material model.

4

Fundamental of Continuum Mechanics

Continuum mechanics deals with the behavior of continuously distributed and deformable bodies. It provides a phenomenological framework for describing the motion and deformation of these bodies under external forces and environmental changes, independent of their atomic structure. The continuum is actually a material body composed of an infinite number of infinitesimally small points, which are evenly distributed in the body. Each mathematical point in the continuum represents a material point having physical properties that contribute to the properties of the bulk material. The material points always stay within the body and cannot exceed its boundaries during deformation. The uniform and continuous distribution of material points within a material body as assumptions allows the application of vector algebra and differential calculations as analytical tools to develop such material models.
In this chapter, the relevant parts of continuum mechanics have been explained serving as a foundation for the developed material model.
In general, continuum mechanical theory is divided into:

- **Kinematics**, describing the motion and deformation of a body independent of its cause;

- **Balance equations**, as axiomatic conservation laws governing mass, momentum, energy and entropy;
- **Constitutive laws**, describing the material specific behaviour as correlation between the stress state and the deformation state,

which are discussed in detail in the following sections.

4.1 Kinematics

As explained, kinematics focuses on the motion of a body without addressing its causes, enabling the mathematical quantification of the body's deformation. We consider a material body $\mathcal{B}$ at time $t = t_0$ as the reference configuration, where the body is still in its undeformed state (Fig. 4.1). Once the body is subjected to a stress vector $\boldsymbol{t}$ at time $t > t_0$, this leads to a deformation of the body. The deformed state of the body is referred to as the current configuration. In the context of continuum mechanics, a material point is a mathematical point. This means that each material point within the body can be associated with a position vector.

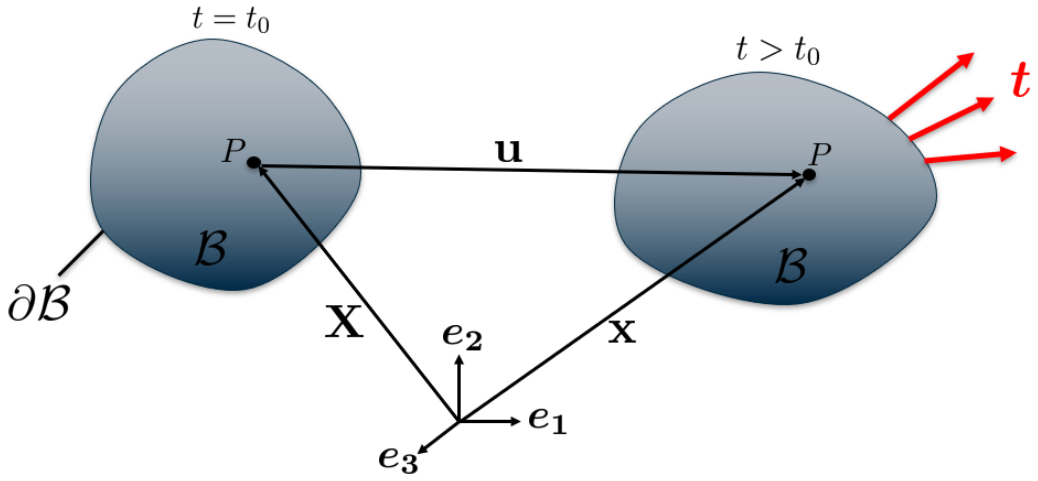

Figure 4.1: Reference and current configuration of a material body $\mathcal{B}$.

The material body $\mathcal{B}$ is enclosed by the boundary $\partial\mathcal{B}$, which consists of the set of material points located on its surface. The motion and deformation

of the material body $\mathcal{B}$ are characterized by the movement of these material points. The material point P has the position vector $\mathbf{X}$ in the reference configuration and the position vector $\mathbf{x}$ in the current configuration. The displacement experienced by point P is calculated by the displacement vector $\mathbf{u}$. It applies:

$$\mathbf{x}=\mathbf{X}+\mathbf{u}(P,\mathrm{t})=\mathbf{X}+\mathbf{u}(\mathbf{X},\mathrm{t}) \tag{4.1}$$

A material point $\mathbf{X}$ is mapped from the reference configuration to the current configuration under an external load through the motion function $\boldsymbol{\chi}(\mathbf{X},\mathrm{t})$. This motion function is bijective, ensuring a one-by-one correspondence. The position vectors $\mathbf{X}$ in the reference configuration and $\mathbf{x}$ in the current configuration are related through this motion function:

$$\mathbf{x} = \boldsymbol{\chi}(\mathbf{X},\mathrm{t}) \Longleftrightarrow \mathbf{X} = \boldsymbol{\chi}^{-1}(\mathbf{x},\mathrm{t}) \tag{4.2}$$

The Lagrangian or material representation expresses kinematic quantities relative to the reference configuration. In contrast, the Eulerian or spatial representation defines kinematic quantities based on the position vector in the current configuration. In the Lagrangian framework, the velocity $\dot{\mathbf{x}}$ and acceleration $\ddot{\mathbf{x}}$ of a material point P are determined as the first and second time derivatives of the motion function with respect to time (eq. 4.2):

$$\dot{\mathbf{x}}(\mathbf{X},\mathrm{t}) = \frac{\mathrm{d}\boldsymbol{\chi}(\mathbf{X},\mathrm{t})}{\mathrm{dt}} \quad \text{and} \quad \ddot{\mathbf{x}}(\mathbf{X},\mathrm{t}) = \frac{\mathrm{d}^2\boldsymbol{\chi}(\mathbf{X},\mathrm{t})}{\mathrm{dt}^2} \tag{4.3}$$

In kinematics, two concepts are distinguished based on the magnitude of deformations, namely geometric linearity and geometric nonlinearity. Geometric linearity applies to situations involving small deformations, such as linear elastic deformation or even metal plasticity, whereas geometric nonlinearity pertains to cases with large deformations, like viscoelastic behavior of rubber or metal forming. Since this work focuses on metal plasticity, where deformations can still be considered small-scale, the theory of geometric linear kinematics will be further explored [7, 44, 40].

4.1.1 Geometric Linear Kinematics

As previously explained, the displacement field of the entire body can be determined by mapping all material points. However, this displacement field alone is insufficient for calculating the deformation.
To achieve this, we must examine the displacements of the respective points

within a small volume element. Since representing a 3D volume element is highly complex, we will simplify the analysis by focusing on a 2D representation instead.
We pick out a small volume element from the entire body with the reference points P, Q and R, as shown in Figure 4.2.

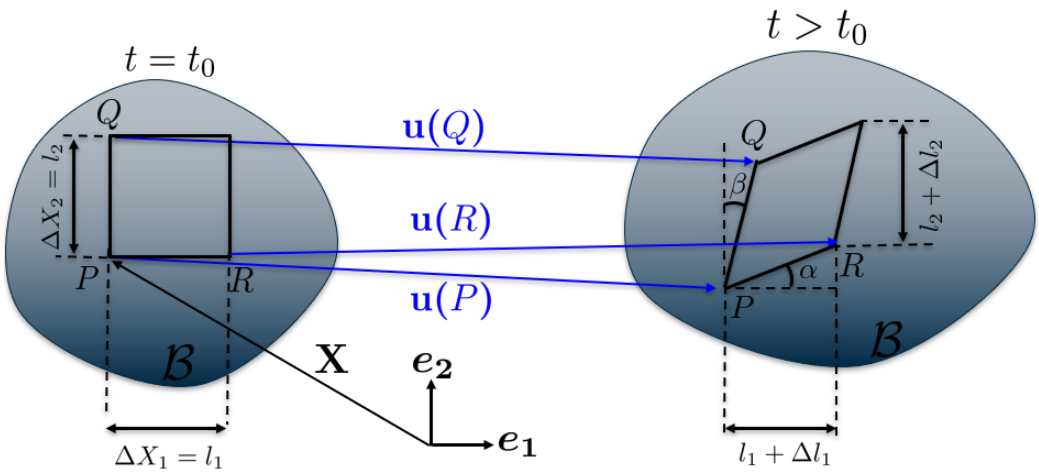

Figure 4.2: Material volume element in the reference and current configuration .

The corresponding displacement vectors for the respective reference points are also illustrated schematically in Fig. 4.2. The displacement of point P is assumed to be known. Since the dimensions of the volume element are infinitesimally small, the displacements of neighboring points can be approximated using a Taylor series expansion.

$$\mathbf{u}(Q) \cong \mathbf{u}(P) + \frac{\partial \mathbf{u}(\mathbf{X})}{\partial X_2} \Delta X_2 \qquad \mathbf{u}(R) \cong \mathbf{u}(P) + \frac{\partial \mathbf{u}(\mathbf{X})}{\partial X_1} \Delta X_1 \tag{4.4}$$

After approximating the displacement field, the changes in length can be determined by calculating the difference between the corresponding lengths in the current configuration and those in the reference configuration.

$$\Delta l_1 = \frac{\partial u_1}{\partial X_1} l_1 \implies \varepsilon_{11} = \frac{\Delta l_1}{l_1} = \frac{\partial u_1}{\partial X_1} \tag{4.5}$$

$$\Delta l_2 = \frac{\partial u_2}{\partial X_2} l_2 \implies \varepsilon_{22} = \frac{\Delta l_2}{l_2} = \frac{\partial u_2}{\partial X_2} \tag{4.6}$$

The shape of the rhombus or Rhombohedron in the three-dimensional case is characterized not only by the changes in the length of the edges but also by the changes in the angle of the originally right angles.

$$\tan(\alpha) = \frac{u_2(R) - u_2(P)}{l_1 + \Delta l_1} \qquad \tan(\beta) = \frac{u_1(Q) - u_1(P)}{l_2 + \Delta l_2} \tag{4.7}$$

After applying Eq. 4.4 and linearization due to the small deformation framework, where $\alpha = \tan(\alpha)$ and $\beta = \tan(\beta)$, Eq. 4.22 results as follows:

$$\alpha = \frac{\partial u_2}{\partial X_1} \qquad \beta = \frac{\partial u_1}{\partial X_2} \tag{4.8}$$

and then a mean angle change can be defined by:

$$\varepsilon_{12} = \frac{1}{2}(\alpha + \beta) = \frac{1}{2}(\frac{\partial u_1}{\partial X_2} + \frac{\partial u_2}{\partial X_1}) \tag{4.9}$$

When this concept is extended to 3D in a same way, the deformation can be represented in matrix notation as follows:

$$\boldsymbol{\varepsilon} \hat{=} \begin{bmatrix} \varepsilon_{11} & \varepsilon_{12} & \varepsilon_{13} \\ \varepsilon_{21} & \varepsilon_{22} & \varepsilon_{23} \\ \varepsilon_{31} & \varepsilon_{32} & \varepsilon_{33} \end{bmatrix} \tag{4.10}$$

In this matrix representation, the diagonal elements represent the changes in length, while the off-diagonal elements indicate the changes in angles. Finally, the deformation can generally be formulated as the strain tensor as follows:

$$\boldsymbol{\varepsilon} = \frac{1}{2}(\mathrm{Grad}\,\mathbf{u} + \mathrm{Grad}^{\mathrm{T}}\mathbf{u}) \tag{4.11}$$

$$\mathrm{Grad}\,\mathbf{u} = \frac{\partial \mathbf{u}}{\partial \mathbf{X}} = \frac{\partial u_i}{\partial X_j}\mathbf{e}_i \otimes \mathbf{e}_j \tag{4.12}$$

4.2 Balance Equations

While the kinematic considerations of the previous section establish a link between the displacement of the material points and the distortions, the balance equations represent the mathematical formulation of the physical conserva-

tion statements. In classical physics, the balance equations are introduced axiomatically. In continuum mechanics, the balances of mass, momentum and angular momentum are fundamental principles [7, 44, 40, 55]. These can be expressed through the following axioms

- **Mass balance**: The mass of a material body remains constant during its motion;
- **Momentum balance**: The momentum of a material body changes due to the forces acting on the body;
- **Angular momentum balance**: The spin of a material body changes due to the moments that act on the body.

The momentum balance equation will be discussed in greater detail, as it is the most important balance equation in this work.
The core concept of momentum balance is Newton's second law ($\mathbf{f} = \mathrm{m}\mathbf{a}$), which is valid for rigid bodies. However, in continuum mechanics, where deformable bodies are considered, Newton's second law must be generalized to account for deformable materials. The force $\mathbf{f}$ acting on a body can be split into short-range and long-range components. Short-range forces arise from the immediate environment interacting with the body's surface $\partial\mathcal{B}$, while long-range forces, such as gravity, act within the body and are not affected by immediate surroundings. This division leads to

$$\mathbf{f} = \int_{\partial\mathcal{B}} \mathbf{t}\,\mathrm{d}a + \int_{\mathcal{B}} \rho\mathbf{b}\,\mathrm{d}v \tag{4.13}$$

Here, $\mathbf{t}$ represents the stress vectors on the body surface that are transmitted by contact of the body with its environment, while $\rho\mathbf{b}$ is the volume force density acting inside the body.
The term "$m\boldsymbol{a}$" on the right-hand side of Newton's second law represents the momentum change of a rigid body:

$$\dot{\mathbf{I}} = m\dot{\mathbf{v}} = m\ddot{\mathbf{x}} \tag{4.14}$$

For deformable materials, the momentum change is given as the total contribution of all material points within the body $\mathcal{B}$:

$$\dot{\mathbf{I}} = \frac{\mathrm{d}}{\mathrm{d}t}\int_{\mathcal{B}} \rho\dot{\mathbf{x}}\,\mathrm{d}v = \int_{\mathcal{B}} \rho\ddot{\mathbf{x}}\,\mathrm{d}v \tag{4.15}$$

Combining this with Eq. 4.13 leads to the global momentum balance:

$$\int_{\mathcal{B}} \rho \ddot{\mathbf{x}} \, \mathrm{d}v = \int_{\partial\mathcal{B}} \mathbf{t} \, \mathrm{d}a + \int_{\mathcal{B}} \rho \mathbf{b} \, \mathrm{d}v \tag{4.16}$$

To transition from a global statement to a local one, the surface integral of the short-range forces must be converted to a volume integral. This transformation is feasible if the Cauchy theorem applies to the surface force density $\mathbf{t}$ on the body's boundary

$$\mathbf{t} = \mathbf{T} \cdot \mathbf{n} \tag{4.17}$$

if there is a stress tensor $\mathbf{T}$ that generates the stress vector $\mathbf{t}$ on the surface with the normal vector $\mathbf{n}$. The stress tensor $\mathbf{T}$ is called the Cauchy stress tensor. In this case, Gauss's theorem (divergence theorem) can be applied, provided the stress tensor has the necessary continuity and differentiability requirements. The following then follows

$$\int_{\partial\mathcal{B}} \mathbf{t} \, \mathrm{d}a \; = \int_{\partial\mathcal{B}} \mathbf{T} \cdot \mathbf{n} \, \mathrm{d}a \; = \int_{\mathcal{B}} \operatorname{div} \mathbf{T} \, \mathrm{d}v \tag{4.18}$$

where

$$\operatorname{div} \mathbf{T} \hat{=} \sum_{j=1}^{3} \frac{\partial T_{ij}}{\partial X_j} \tag{4.19}$$

The combination of equations 4.16 and 4.18 leads to

$$\int_{\mathcal{B}} (\rho \ddot{\mathbf{x}} \; - \operatorname{div} \mathbf{T} \; - \rho \mathbf{b}) \, \mathrm{d}v = 0 \tag{4.20}$$

Since the momentum balance 4.20 also applies to any partial body, the integral itself must be zero. This leads to the local form of the momentum balance

$$\rho \ddot{\mathbf{x}} \; = \operatorname{div} \mathbf{T} \; + \rho \mathbf{b} \tag{4.21}$$

In the static or quasi-static case, ignoring the inertia forces expressed by $\rho \ddot{\mathbf{x}}$, the balance of momentum simplifies to

$$\operatorname{div} \mathbf{T} \; + \rho \mathbf{b} = 0 \tag{4.22}$$

4.3 Constitutive Equations

Kinematics and balance equations are universal, material-independent relationships. In contrast, constitutive laws are formulated to describe the specific behavior of a material by relating stresses to strains. The development of constitutive laws is guided by principles from rational mechanics, which provide several foundational rules for this process [74, 75, 95]. The second law of thermodynamics plays a crucial role in the development and formulation of these constitutive laws by ensuring that the material behavior is physically realistic and thermodynamically consistent. Additional details on constitutive modeling can be found in [41, 44, 55, 78].
Material behavior can generally be classified into four groups based on their response to external forces, considering factors such as time dependence and reversibility, as follows [18, 57, 79]:

- **Elastic**: Rate-independent without equilibrium hysteresis (reversible);
- **Viscoelastic**: Rate-dependent without equilibrium hysteresis (reversible);
- **Plastic**: Rate-independent with equilibrium hysteresis (irreversible);
- **Viscoplastic**: Rate-dependent with equilibrium hysteresis (irreversible);

The typical stress-strain curves of the above-mentioned material groups are shown in Fig. 4.3.

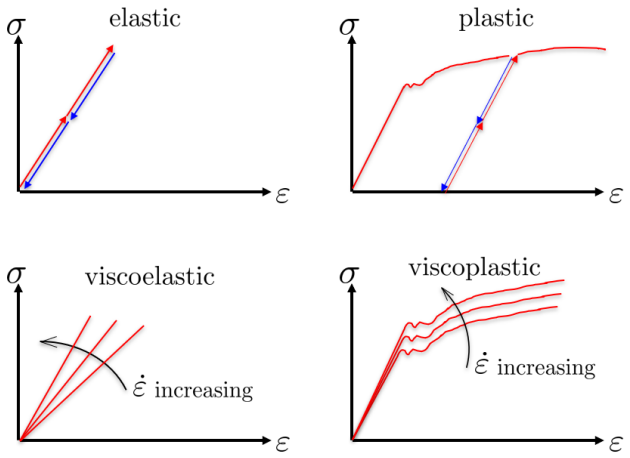

Figure 4.3: Typical stress-strain curves of the different types of material behavior.

As this study focuses on the development of an anisotropic elasto-plastic material model, only the theories of elastic and plastic behavior are discussed in detail below.

4.3.1 Anisotropic Elasticity and Orthogonal Transformations

Anisotropy is an important common feature of most heterogeneous materials. Physical or mechanical properties of a specimen vary depending on the direction in which they are measured. In other words, an anisotropic material does not have uniform characteristics in all directions. With the exception of the complete anisotropy the anisotropy is always restricted by symmetry conditions caused by material structure [21, 17]. These symmetry conditions result from either special microstructures such as composite materials or, on a macroscale, from a special geometry of the structure such as auxetic materials. All solids can be characterized in different material groups based on the number of existing symmetry planes in the structure, from triclinic materials without any symmetry plane to isotropic materials with infinite symmetry planes. With the help of Tab. 4.1 and Fig. 4.4 all possible material groups can be well represented in terms of the number of symmetry planes, where the vectors $\boldsymbol{OP}$ and $\boldsymbol{OQ}$ represent the normal vectors of the corresponding symmetry planes [94].

Table 4.1: The groups of material symmetry in context of anisotropy

Type of symmetry	Planes of symmetry	Position of normal vectors
Triclinic	0	-
Monoclinic	1	$\theta = 0$ or $\pi/2$ or $\varphi = \pi/2$
Orthotropic	3	$\theta = 0$, $\pi/2$ and $\varphi = \pi/2$
Trigonal	3	$\theta = 0$ and $\pm\pi/3$
Tetragonal	5	$\theta = 0$, $\pm\pi/4$, $\pi/2$ and $\varphi = \pi/2$
Hexagonal	7	$\theta = 0$, $\pm\pi/6$, $\pm\pi/3$, $\pi/2$ and $\varphi = \pi/2$
Cubic	9	$\theta = 0$, $\pm\pi/8$, $\pm\pi/6$, $\pm\pi/4$, $\pi/2$ and $\varphi = \pi/2$
Transverse isotropic	∞	$\boldsymbol{e}_3$ axis of symmetry
Isotropic	∞	∞

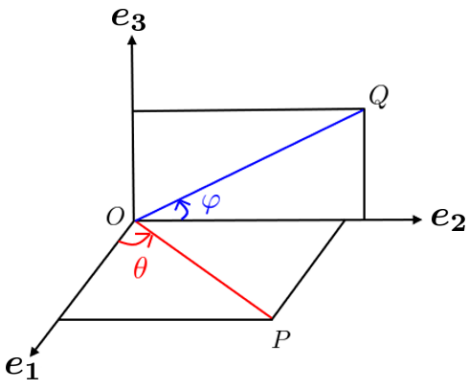

Figure 4.4: O represents the material origin and the vectors $\boldsymbol{OP}$ and $\boldsymbol{OQ}$ are the normals to planes of reflection symmetry mentioned in Table 4.1

Hooke's law is a key principle that explains the elastic behavior of materials under small strains caused by external forces. It is generally expressed as:

$$\boldsymbol{\sigma} = \overset{4}{\mathbf{C}} : \boldsymbol{\varepsilon} \tag{4.23}$$

$$\boldsymbol{\varepsilon} = \overset{4}{\mathbf{S}} : \boldsymbol{\sigma} \tag{4.24}$$

Here, $\boldsymbol{\sigma}$ and $\boldsymbol{\varepsilon}$ represent engineering stress and strain, respectively, while $\overset{4}{\mathbf{C}}$ and $\overset{4}{\mathbf{S}}$ denote the fourth-order elastic stiffness and compliance tensors. The superscript 4 indicates the order of the tensor, signifying the number of basis components required to characterize it.
The fourth order elasticity tensor $\mathbf{C}$ contains 81 components ($3 \times 3 \times 3 \times 3$), which in the general case (full anisotropy) are characterized by 21 indepen-

dent elastic material parameters.
For isotropic materials, Hooke's law is expressed as:

$$\boldsymbol{\sigma} = 2\mu\boldsymbol{\varepsilon} + \lambda(\operatorname{tr}\boldsymbol{\varepsilon})\,\mathbf{I} \tag{4.25}$$

where the elastic behavior is characterized by only two independent material parameters, namely μ and λ known as the Lamé constants. In this equation $\operatorname{tr}\boldsymbol{\varepsilon}$ denotes the trace of the strain tensor and $\mathbf{I}$ refers to the identity tensor. These parameters can alternatively be expressed using Young's modulus E, the bulk modulus k and Poisson's ratio ν.
Anisotropic elasticity has been extensively studied in the past several decades, primarily because of its relevance in composite materials. Its behavior is always constrained by symmetry conditions imposed by the material's internal structure. To understand how symmetry properties impact the elastic behavior of an anisotropic material, it is crucial to consider orthogonal transformation relationships that mathematically describe rotations around an axis or reflections across a plane. This approach results in a reduction in the number of independent elastic constants needed to characterize the fourth-order elastic tensor $\mathbf{C}$, which depends on the number of symmetry planes in the structure of the material [94].
An orthogonal tensor represents a rigid transformation, which means that it does not alter the shape of a body. Orthogonal tensors possess several useful properties, one of which is that their inverse is equal to their transpose, making them particularly convenient to work with [45].
Consider an orthonormal basis $\mathbf{B} = \{\boldsymbol{e}_1, \boldsymbol{e}_2, \boldsymbol{e}_3\}$ that is rotated counterclockwise around the $\boldsymbol{e}_3$-axis by an angle θ, resulting in a new orthonormal basis $\mathbf{B}' = \{\boldsymbol{e}'_1, \boldsymbol{e}'_2, \boldsymbol{e}_3\}$, as shown in Fig. 4.5. The two bases, $\mathbf{B}$ and $\mathbf{B}'$, are related by an orthogonal tensor $\mathbf{R}$.

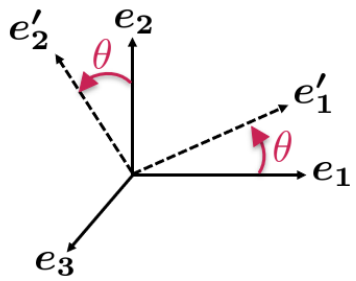

Figure 4.5: Illustration of the two orthonormal bases $\mathbf{B} = \{\boldsymbol{e}_1, \boldsymbol{e}_2, \boldsymbol{e}_3\}$ and $\mathbf{B}' = \{\boldsymbol{e}'_1, \boldsymbol{e}'_2, \boldsymbol{e}_3\}$, where $\mathbf{B}'$ is obtained by rotating $\mathbf{B}$ by an angle θ about the $\boldsymbol{e}_3$-axis.

Depending on the type of objects to be transformed according to the new base $\mathbf{B}'$, the following relationships apply:

$$\mathbf{e}' = \mathbf{R} \cdot \mathbf{e} \tag{4.26}$$

$$\mathbf{L}' = \mathbf{R} \cdot \mathbf{L} \cdot \mathbf{R}^{\mathrm{T}} \tag{4.27}$$

$$\overset{4}{\mathbf{C}}{}' = (\mathbf{R} \otimes \mathbf{R}) : \overset{4}{\mathbf{C}} : (\mathbf{R} \otimes \mathbf{R})^T \tag{4.28}$$

where $\mathbf{e}$, $\mathbf{L}$ and $\overset{4}{\mathbf{C}}$ denote a first order (vector), a second order and a fourth order tensor respectively, with respect to the basis $\mathbf{B}$, while $\mathbf{e}'$, $\mathbf{L}'$ and $\overset{4}{\mathbf{C}}{}'$ represent the corresponding quantities relative to the rotated basis $\mathbf{B}'$ [94]. In general, the terms ***reflection*** and ***rotation*** are distinguished in the context of orthogonal transformations. The existence of a plane of symmetry in the structure implies that objects are reflected across this symmetry plane without altering their properties. Consequently, the orthogonal tensor $\mathbf{R}$ must satisfy the following conditions:

$$\mathbf{R} \cdot \mathbf{n} = -\mathbf{n} \tag{4.29}$$

$$\mathbf{R} \cdot \mathbf{m} = \mathbf{m} \tag{4.30}$$

where $\mathbf{n}$ refers to the unit vector normal to the reflection plane and $\mathbf{m}$ to the any vector on the reflection plane. The conditions 4.29 and 4.30 lead to this expression for tensor $\mathbf{R}$, thus:

$$\mathbf{R} = \mathbf{I} - 2\mathbf{n} \otimes \mathbf{n} \tag{4.31}$$

where $\mathbf{I}$ denotes the second order identity tensor. In general, the unit vector $\mathbf{n}$ in plane can be written as:

$$\mathbf{n}^{\mathrm{T}} \mathrel{\hat{=}} [\cos\theta,\ \sin\theta,\ 0] \tag{4.32}$$

which leads to a concrete definition of the tensor $\mathbf{R}$ using Equation 4.31:

$$\mathbf{R}(\theta)_{ref} \mathrel{\hat{=}} \begin{bmatrix} -\cos 2\theta & -\sin 2\theta & 0 \\ -\sin 2\theta & \cos 2\theta & 0 \\ 0 & 0 & 1 \end{bmatrix} \tag{4.33}$$

By applying the same methodology, the corresponding orthogonal tensor

responsible for rotation around the $\boldsymbol{e_3}$-axis can also be derived as:

$$\mathbf{R}(\theta)_{rot} \hat{=} \begin{bmatrix} \cos\theta & -\sin\theta & 0 \\ \sin\theta & \cos\theta & 0 \\ 0 & 0 & 1 \end{bmatrix} \tag{4.34}$$

As shown in Table 4.1, orthotropic materials, which are the most common type of anisotropic materials, exhibit three planes of symmetry located at $\theta = 0,\ \pi/2$ and $\varphi = \pi/2$. This means that the elasticity tensor $\overset{4}{\mathbf{C}}$ must remain unchanged (be invariant) under the respective reflection transformations associated with these symmetry planes. Applying the three angles specified for orthotropy in the transformation tensor $\mathbf{R}$ and using them in Eq. 4.28, together with the condition $\overset{4}{\mathbf{C}}' = \overset{4}{\mathbf{C}}$ derived from the symmetry constraint, leads to some restriction on the elasticity tensor $\overset{4}{\mathbf{C}}$, which require some of its components to be zero. In Voigt notation, this leads to:

$$\begin{bmatrix} C_{11} & C_{12} & C_{13} & C_{14} & C_{15} & C_{16} \\ C_{21} & C_{22} & C_{23} & C_{24} & C_{25} & C_{26} \\ C_{31} & C_{32} & C_{33} & C_{34} & C_{35} & C_{36} \\ C_{41} & C_{42} & C_{43} & C_{44} & C_{45} & C_{46} \\ C_{51} & C_{52} & C_{53} & C_{54} & C_{55} & C_{56} \\ C_{61} & C_{62} & C_{63} & C_{64} & C_{65} & C_{66} \end{bmatrix} \Longrightarrow \begin{bmatrix} C_{11} & C_{12} & C_{13} & 0 & 0 & 0 \\ C_{21} & C_{22} & C_{23} & 0 & 0 & 0 \\ C_{31} & C_{32} & C_{33} & 0 & 0 & 0 \\ 0 & 0 & 0 & C_{44} & 0 & 0 \\ 0 & 0 & 0 & 0 & C_{55} & 0 \\ 0 & 0 & 0 & 0 & 0 & C_{66} \end{bmatrix}$$

where the left matrix denotes the corresponding elasticity matrix in case of total anisotropy (triclinic), while the matrix on the right side corresponds to the orthotropic materials. This approach can also be applied to characterize all other elastic tensors with respect to the type of symmetry present in the materials. For simplicity in presentation, the compliance tensor $\overset{4}{\mathbf{S}}$ is preferably presented here including its elastic constant instead of the elastic tensor $\overset{4}{\mathbf{C}}$. The so-called engineering constants, as the components of the tensor $\overset{4}{\mathbf{S}}$, can be determined in the Voigt notation for orthotropic materials as a function of the coefficients S_{ij}:

$$S_{ii} = \frac{1}{E_i}, \qquad i = 1, 2, 3$$
$$S_{kk} = \frac{1}{2G_{ij}}, \quad i \neq j = 1, 2, 3, \quad k = 4, 5, 6$$

$$S_{ij} = \frac{-\nu_{ij}}{E_i}, \quad i \neq j = 1, 2, 3$$

resulting in the compliance tensor for orthotropic materials as follows:

$$\mathbf{S} \hat{=} \begin{bmatrix} \frac{1}{E_1} & \frac{-\nu_{21}}{E_2} & \frac{-\nu_{31}}{E_3} & 0 & 0 & 0 \\ \frac{-\nu_{21}}{E_2} & \frac{1}{E_2} & \frac{-\nu_{32}}{E_3} & 0 & 0 & 0 \\ \frac{-\nu_{31}}{E_3} & \frac{-\nu_{32}}{E_3} & \frac{1}{E_3} & 0 & 0 & 0 \\ 0 & 0 & 0 & \frac{1}{G_{13}} & 0 & 0 \\ 0 & 0 & 0 & 0 & \frac{1}{G_{23}} & 0 \\ 0 & 0 & 0 & 0 & 0 & \frac{1}{G_{12}} \end{bmatrix}$$

As can be seen from the tensor $\overset{4}{\mathbf{S}}$, there are in total 9 independent elastic constants describing the elastic behavior of an orthotropic material, where E_i, G_{ij} and ν_{ij} correspond to the Young's moduli, shear moduli and Poisson's ratios in terms of different directions.

4.3.2 Plasticity

Plasticity is a fundamental property of materials that describes their ability to undergo permanent deformation when subjected to external forces. In contrast to elasticity, where materials regain their original shape after the applied load is removed, plasticity involves permanent and irreversible changes in shape or size. At the microscopic level, plasticity arises from the movement of dislocations, whereas elasticity results from the distortion of the material's lattice structure. This phenomenon causes a shift in the behavior of the stress-strain curve at the macroscopic level [52, 6, 66, 49, 37].
Figure 4.6 illustrates a typical stress-strain curve of a ductile metal subjected to a uniaxial tensile test.

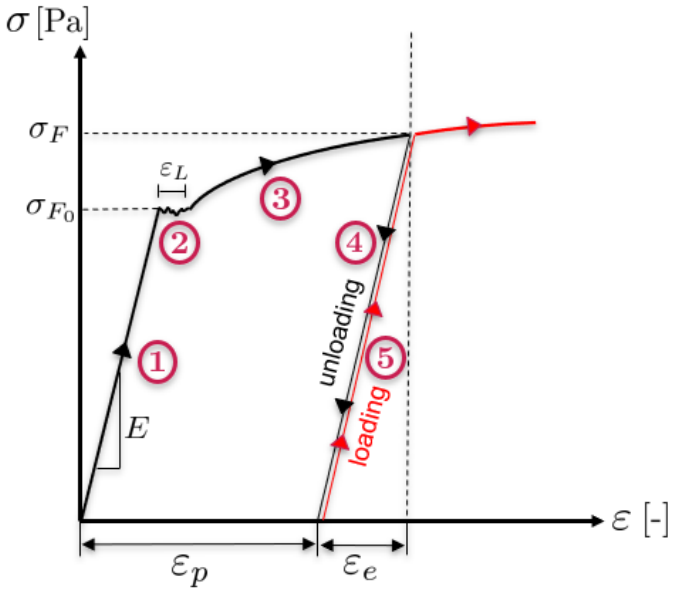

Figure 4.6: Typical stress-strain curve of a ductile metal including loading and unloading path [25].

Initially, the material exhibits linear-elastic behavior in response to the load, which is characterized by the Young's modulus (E) as the slope of the linear region. In this area ①, the material returns to its original state when the load is removed. Once the stress reaches the critical value σ_{F_0}, the material begins to deform plastically. Beyond this point, the curve has a flatter slope, with slight stress oscillations often occurring as strain increases which is known as Lüders strain (ε_L) ②. This behavior, common in metals, arises from dislocations piling up at grain boundaries. Once enough dislocations accumulate, they move again, restoring a uniform stress-strain curve ③. In continuum mechanical modeling, the area of Lüders strain is usually neglected. If loading is reversed at the $\sigma = \sigma_F$, unloading follows a curve parallel to the elastic line ④. After complete unloading, a residual plastic strain $\varepsilon_p > 0$ remains, leaving the sample longer. Re-loading increases stress along the unloading curve until σ_F is reached again, then continues along the original loading path ⑤.
In summary, the main points discussed so far are as follows:

$$\sigma < \sigma_{F_0} \implies \varepsilon_p = 0 \implies \varepsilon = \varepsilon_e \implies \sigma = E\varepsilon_e$$
$$\sigma \geq \sigma_{F_0} \implies \varepsilon_p > 0 \implies \varepsilon = \varepsilon_e + \varepsilon_p \implies \sigma = E(\varepsilon - \varepsilon_p)$$

This can be utilized to define a new term that characterizes the material

yielding, referred to as the yield condition or yield criterion F, which is expressed as follows in one dimensional case:

$$F(\sigma) = \sigma - \sigma_F : \begin{cases} < 0 \rightarrow \text{elastic}, \\ = 0 \rightarrow \text{plastic}, \\ > 0 \rightarrow \text{undefined}, \end{cases} \tag{4.35}$$

where σ refers to the current stress acting on material and σ_F to the current yield stress. Under the yield condition, $F > 0$ is not allowed, since the stresses cannot exceed the current yield stress. Instead, the yield stress increases during yielding, a process known as hardening, also referred to as strain or work hardening. This implies a hardening rule to describe how yield stress increases with strain. For linear hardening, the following applies:

$$\dot{\sigma}_F = H\dot{\varepsilon}_p \implies \sigma_F = \sigma_{F_0} + H\varepsilon_p \tag{4.36}$$

Here H refers to the linear hardening modulus, which is determined experimentally.
All the concepts discussed so far apply to the 1D case. However, for continuum mechanical material modeling, they must be extended to 3D. As mentioned in Section 4.1.1, strain in 3D is defined as a tensor, its components are derived from the displacement gradient (see Eq. 4.11). The strain tensor can be additively decomposed into elastic and plastic components:

$$\boldsymbol{\varepsilon} = \boldsymbol{\varepsilon}_e + \boldsymbol{\varepsilon}_p \tag{4.37}$$

As long as the material deforms elastically, the generalized Hooke's law applies:

$$\boldsymbol{\sigma} = 2G\boldsymbol{\varepsilon}'_e + k(\operatorname{tr}\boldsymbol{\varepsilon}_e)\,\mathbf{I} \tag{4.38}$$

where $\operatorname{tr}\boldsymbol{\varepsilon}_e$ refers to the volumetric part and $\boldsymbol{\varepsilon}'_e$ to the deviatoric part of elastic strain tensor:

$$\boldsymbol{\varepsilon}'_e = \boldsymbol{\varepsilon}_e - \frac{1}{3}(\operatorname{tr}\boldsymbol{\varepsilon}_e)\,\mathbf{I} \tag{4.39}$$

Yield Criteria

A yield condition defines the elastic limit within a material. It specifies when and under which loading conditions the material begins to deform plastically.

In the 1D-case the yield condition is formulated as Eq. 4.35. In 3D, the yield condition appears similar, except that F depends on tensorial stress rather than scalar stress:

$$F(\boldsymbol{\sigma}) \begin{cases} < 0 \rightarrow \text{elastic} \\ = 0 \rightarrow \text{plastic} \\ > 0 \rightarrow \text{undefined} \end{cases} \tag{4.40}$$

This implies F to be formulated in such a way that it outputs a scalar value from the stress tensor $\boldsymbol{\sigma}$. Since the stress tensor depends on the choice of a coordinate system, F is formulated in terms of stress invariants to ensure its value remains independent of the coordinate system. Theoretically, three different stress invariants can be derived from the symmetric stress tensor, which are independent of each other. These invariants are expressed as follows:

$$I_1 = \operatorname{tr} \boldsymbol{\sigma} = \boldsymbol{\sigma} : \mathbf{I} \tag{4.41}$$

$$I_2 = \operatorname{tr} (\boldsymbol{\sigma} \cdot \boldsymbol{\sigma}) = \boldsymbol{\sigma} \ : \boldsymbol{\sigma}^{\mathrm{T}} \tag{4.42}$$

$$I_3 = \operatorname{tr} (\boldsymbol{\sigma} \cdot \boldsymbol{\sigma} \cdot \boldsymbol{\sigma}) = (\boldsymbol{\sigma} \cdot \boldsymbol{\sigma}) : \boldsymbol{\sigma}^{\mathrm{T}} \tag{4.43}$$

It implies:

$$F(\boldsymbol{\sigma}) = f(I_1, I_2, I_3) - \sigma_F \tag{4.44}$$

This implies that the yield function F in three dimensions for an isotropic material is governed by an arbitrary function f of the stress invariants and the yield stress σ_F obtained from the uniaxial tensile test. The function F is material-specific and must be modified or adjusted as needed to satisfy the properties of the material. In this context, the stress tensor can be split into two terms, namely deviatoric $\boldsymbol{\sigma}'$ and volumetric $\boldsymbol{\sigma}^{\mathrm{V}}$ parts, which are defined as follows:

$$\boldsymbol{\sigma}' = \boldsymbol{\sigma} - \frac{1}{3}(\operatorname{tr} \boldsymbol{\sigma})\, \mathbf{I} \qquad \text{where} \qquad \operatorname{tr} \boldsymbol{\sigma}' = 0 \tag{4.45}$$

$$\boldsymbol{\sigma}^{\mathrm{V}} = \frac{1}{3}(\operatorname{tr} \boldsymbol{\sigma})\, \mathbf{I} = -p\, \mathbf{I} \tag{4.46}$$

where p refers to the hydrostatic pressure defined as $p = -\frac{1}{3}(\operatorname{tr} \boldsymbol{\sigma})$. The volumetric part of the stress tensor is responsible for the change in volume of the material, whereas the deviatoric part contributes to the change in shape of the material. Analogous to the stress tensor, three invariants can also be defined with respect to the stress deviator $\boldsymbol{\sigma}'$:

$$J_1 = \operatorname{tr} \boldsymbol{\sigma}' = 0 \tag{4.47}$$

$$J_2 = \frac{1}{2}(\boldsymbol{\sigma}' : \boldsymbol{\sigma}') \tag{4.48}$$

$$J_3 = \det(\boldsymbol{\sigma}') \tag{4.49}$$

After decomposing the stress tensor into its volumetric and deviatoric components, the yield function defined in Eq. 4.44 is modified accordingly:

$$F(\boldsymbol{\sigma}) = \tilde{f}(I_1, J_2, J_3) - \sigma_F \tag{4.50}$$

In the following, the function value of $\tilde{f}$ is referred to as the equivalent stress σ_e, i.e.:

$$\tilde{f}(I_1, J_2, J_3) = \sigma_e \tag{4.51}$$

It has been demonstrated that bulk metals do not exhibit yielding under a hydrostatic stress state i.e. $\sigma_{11} = \sigma_{22} = \sigma_{33}$, as dislocation movements, which are responsible for yielding, are mutually obstructed. Consequently, yielding in these materials depends only on the stress deviator invariants (J_2 , J_3), which are independent of the hydrostatic stress components.
Von Mises (1913) is the most widely used yield criterion for massive metals. It states that yielding occurs when the second invariant of the stress deviator J_2 reaches a critical value κ^2, i.e.:

$$F = J_2 - \kappa^2 = 0 \tag{4.52}$$

By considering the yield condition under a uniaxial tensile test and using σ_F as the single non-zero component of the stress tensor $\boldsymbol{\sigma}$ at which yielding begins to compute J_2, κ^2 can be determined as:

$$\kappa^2 = \frac{1}{3}\sigma_F^2 \tag{4.53}$$

In terms of principal stresses the von Mises yield criterion (4.52) is expressed as follows:

$$(\sigma_{\mathrm{I}} - \sigma_{\mathrm{II}})^2 + (\sigma_{\mathrm{II}} - \sigma_{\mathrm{III}})^2 + (\sigma_{\mathrm{I}} - \sigma_{\mathrm{III}})^2 = 2\sigma_F^2 \tag{4.54}$$

Equation 4.54 forms a cylindrical surface in principal stress space, oriented parallel to the hydrostatic axis, with a radius of $r = \sqrt{\frac{2}{3}}\sigma_F$ in the corresponding π-plane which is prependicular to the hydrostatic axis (see Fig. 4.7-left). As long as the stress state remains inside the cylinder, the material undergoes elastic deformation. Once the stress vector reaches the surface of the cylinder, the material begins to deform plastically. In case of plane stress

($\sigma_{\text{III}} = 0$), Eq. 4.54 reduces to:

$$\sigma_{\text{I}}^2 - \sigma_{\text{I}}\sigma_{\text{II}} + \sigma_{\text{II}}^2 = \sigma_F^2 \tag{4.55}$$

This represents an ellipse in the $\sigma_{\text{I}} - \sigma_{\text{II}}$ plane, as illustrated in Fig. 4.7-right.

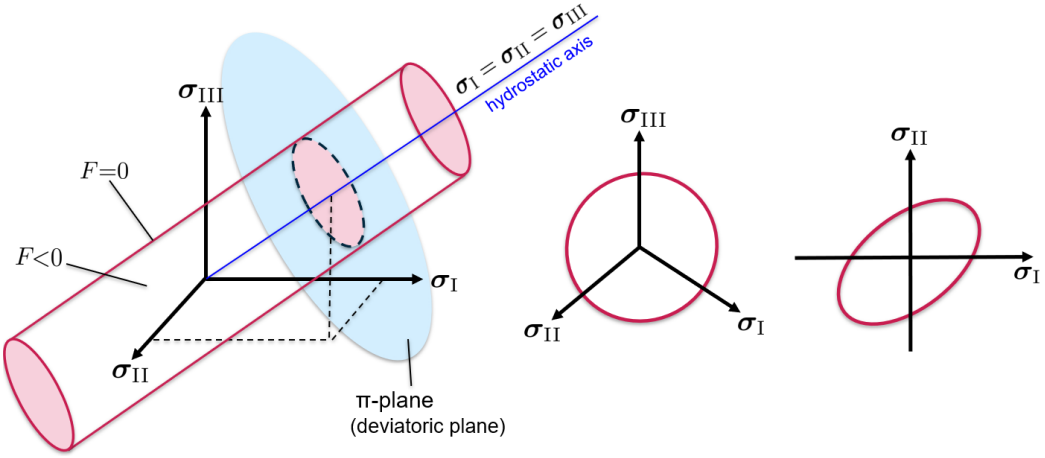

Figure 4.7: Von Mises yield surfaces in terms of principal stresses in 3D (left) and in 2D (right) and the corresponding π-plane (middle).

The von Mises yield criterion describes yielding in bulk metals quite well, where hydrostatic stress has no effect. However, it fails for porous materials, where plasticity can occur under pure hydrostatic stress states.
Drucker and Prager (1950) proposed modifying the von Mises yield criterion by incorporating a hydrostatic stress term αI_1, treating the yield surface as a circular cone [5]:

$$F = \sqrt{3J_2} - \alpha I_1 - \kappa = 0 \tag{4.56}$$

For materials with equal yield stresses in uniaxial tension and compression, κ is determined as:

$$\kappa = \frac{\sigma_F}{3}(\sqrt{3} - \alpha) \tag{4.57}$$

here σ_F is also the yield stress in uniaxial tension. In these equations, α is referred to as the pressure sensitivity parameter, which will be determined experimentally. It is also referred to as the slope of the line in the hydrostatic plane ($I_1 - J_2$ plane).

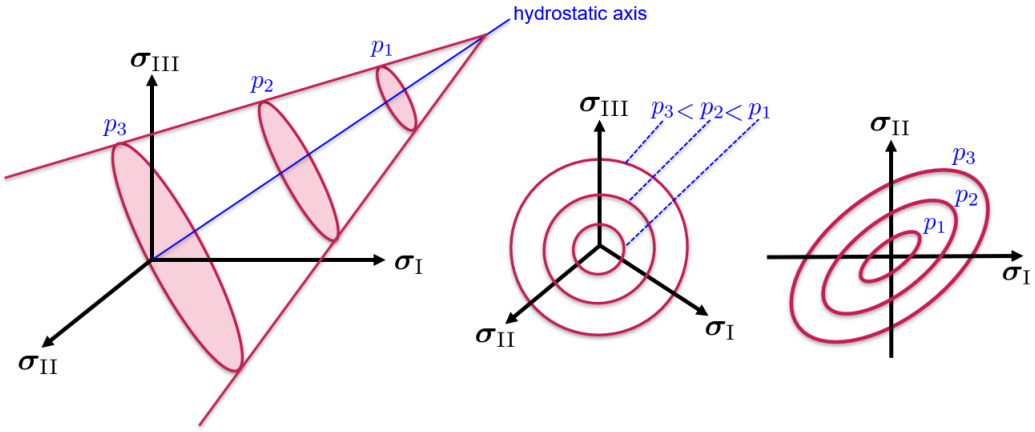

Figure 4.8: Drucker-Prager yield surfaces in terms of principal stresses in 3D (left) and in 2D (right) and the corresponding π-plane (middle).

Figure 4.8 illustrates that the Drucker-Prager yield criterion forms a conical shape in the principal stress space, featuring a circular cross section in the deviatoric plane. The pressure dependence is evident from the variation in the cross-sectional area along the hydrostatic axis; as the hydrostatic pressure (p) increases, the deviatoric area decreases.

Flow Rule

As previously discussed, the total strain can be additively decomposed into elastic and plastic components (Eq. 4.37). The flow rule describes the evolution of plastic strain as an internal variable during deformation and is formulated as follows

$$\dot{\boldsymbol{\varepsilon}}_p = \dot{\lambda} \frac{\partial G(\boldsymbol{\sigma})}{\partial \boldsymbol{\sigma}} \tag{4.58}$$

where $\dot{\lambda}$ represents the plastic multiplier, controlling the magnitude of plastic strain and G denotes the plastic potential, which must be determined experimentally. The term $\frac{\partial G(\boldsymbol{\sigma})}{\partial \boldsymbol{\sigma}}$ represents the direction of the plastic flow. In most cases, the flow function F is chosen as the plastic potential, providing accurate results, particularly for bulk metals. When this assumption is

made, the flow is referred to as ***associated flow***

$$\dot{\boldsymbol{\varepsilon}}_p = \dot{\lambda} \frac{\partial F(\boldsymbol{\sigma})}{\partial \boldsymbol{\sigma}} \,. \tag{4.59}$$

In associated flow, the direction of the plastic flow is always perpendicular to the yield surface in the principal stress space, as illustrated schematically in Fig. 4.9.

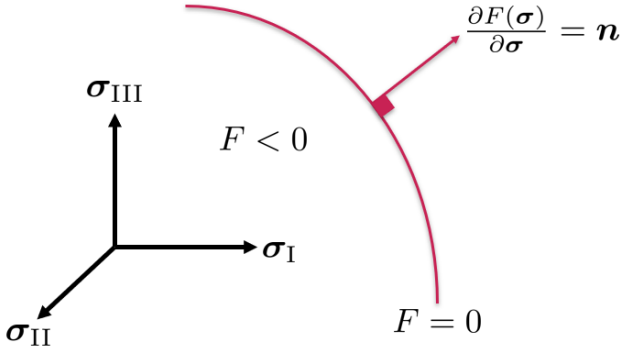

Figure 4.9: Schematic representation of flow direction in principal stress state in case of associated flow [25].

Hardening

Hardening is another component of plasticity and describes how yield stress develops with increasing load. The yield stress σ_F is then influenced by additional internal variables, known as hardening variables φ_i. In general, multiple hardening variables may arise which can be either scalar-valued or tensor-valued. The yield function must be modified to incorporate these variables in a manner that

$$F = F(\boldsymbol{\sigma}, \varphi_i). \tag{4.60}$$

In general, as hardening progresses, the shape and position of the yield surface $F = 0$ in stress space can change in various ways. However, two commonly observed types of hardening are ***isotropic*** and ***kinematic*** hardening. In isotropic hardening, the yield surface retains its shape while its size expands uniformly, as illustrated in Fig. 4.10 (left). In contrast, in kinematic hardening, the yield surface preserves its size but changes position within the

stress space, as shown in Fig. 4.10 (right).

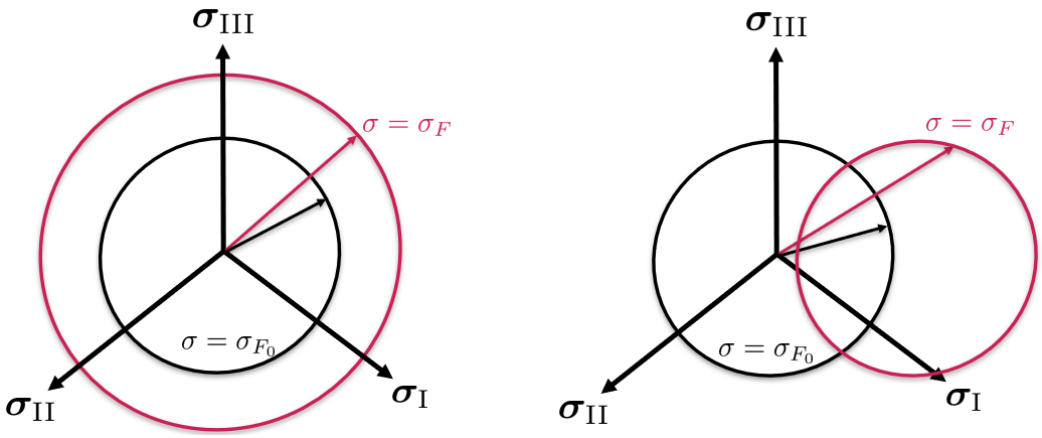

Figure 4.10: Isotropic hardening (left) and kinematic hardening (right)[25].

To determine the type of hardening that a material undergoes, appropriate experiments must be conducted. Kinematic hardening is observed when a material exhibits different yield strengths in tension and compression during cyclic loading. This phenomenon is also known as the *Bauschinger effect*. In the case of isotropic hardening, which is particularly relevant to this work, uniform expansion of the yield surface can be described by scalar hardening parameters q_i, typically expressed as a function of the effective plastic strain $\bar{\varepsilon}^p$. It is therefore convenient to write the yield function as

$$F(\boldsymbol{\sigma}, \bar{\varepsilon}^p) = \sigma_e - \sigma_F = \sigma_e(\boldsymbol{\sigma}) - \sigma_F(\bar{\varepsilon}^p) \tag{4.61}$$

where σ_e refers to the effective stress. In case of von Mises material

$$\sigma_e = \sqrt{3J_2} = \sqrt{\frac{3}{2}(\boldsymbol{\sigma}' : \boldsymbol{\sigma}')} \tag{4.62}$$

$$\bar{\varepsilon}^p = \sqrt{\frac{2}{3}\boldsymbol{\varepsilon}_p : \boldsymbol{\varepsilon}_p} = \sqrt{\frac{2}{3}\left(\lambda\frac{\partial F}{\partial \boldsymbol{\sigma}} : \lambda\frac{\partial F}{\partial \boldsymbol{\sigma}}\right)} \tag{4.63}$$

Since the yield condition $F = 0$ must hold during plastic flow, the material must harden under increasing load. This is expressed by the ***consistency***

condition, which states that:

$$F = 0 \implies \dot{F} = 0 \tag{4.64}$$

Applying the chain rule gives:

$$\dot{F} = \frac{\partial F}{\partial \boldsymbol{\sigma}} : \dot{\boldsymbol{\sigma}} + \frac{\partial F}{\partial \bar{\varepsilon}^p} \dot{\bar{\varepsilon}}^p = 0 \tag{4.65}$$

Now, by combining Equations 4.63 and 4.65, we arrive at a precise definition of the plastic multiplier rate:

$$d\lambda = -\frac{\dfrac{\partial F}{\partial \boldsymbol{\sigma}} : d\boldsymbol{\sigma}}{\dfrac{\partial F}{\partial \bar{\varepsilon}^p}((\dfrac{2}{3})(\dfrac{\partial F}{\partial \boldsymbol{\sigma}}) : (\dfrac{\partial F}{\partial \boldsymbol{\sigma}}))} \tag{4.66}$$

4.3.3 Anisotropic Plasticity

As discussed in Section 4.3.1, anisotropy refers to the variation of a material's properties depending on the direction in which they are measured. In contrast to isotropic models, where the choice of a reference frame is arbitrary, anisotropic models require the use of a coordinate system aligned with the material's structure.
In general, anisotropic plasticity can be characterized in various ways, as discussed by Skrzypek and Ganczarski [90]. One of the earliest formulations of anisotropic plasticity was proposed by Hill 1948 [47], which is an extension of the classical von Mises yield criterion to account for anisotropy. It introduces a quadratic yield function that incorporates different yield stresses along various material directions as follows, making it particularly useful for metals and sheet materials that exhibit orthotropic symmetry.

$$\bar{F}(\boldsymbol{\sigma}) = \sqrt{F(\sigma_{22} - \sigma_{33})^2 + G(\sigma_{33} - \sigma_{11})^2 + H(\sigma_{11} - \sigma_{22})^2 + 2L\sigma_{23}^2 + 2M\sigma_{31}^2 + 2N\sigma_{12}^2}$$

Hier F, G, H, L, M and N are constants obtained by tests of the material in different orientations. Although the Hill model effectively describes the anisotropic plastic behavior of metals, it is restricted to materials with orthotropic symmetry and cannot represent other types of material symmetry. Additionally, it is only applicable to bulk metals where the hydrostatic pressure does not affect the plastic flow.
Following Hill's work, many other researchers have proposed anisotropic yield surfaces in stress space. Among the most notable are those developed

by Bassani (1977) [13], Budiansky (1984) [14], and Barlat et al. (1989, 1991) [12, 11]. All of these yield theories employed an associated flow rule and described the yield surfaces as convex in the stress space. They proposed flow functions that, unlike the Hill criterion, were not restricted to a quadratic form, but instead had an arbitrary degree.
Almost all anisotropic plasticity models are based, either directly or indirectly, on generalized forms of stress deviator invariants. In this framework, the Cauchy stress tensor undergoes a linear transformation. Here, two fundamental concepts are employed. The first involves the use of structural tensors, typically denoted by $\mathbf{M}_i$, which represents the material's privileged directions as

$$\mathbf{M}_i = \mathbf{a}_i \otimes \mathbf{a}_i \tag{4.67}$$

where $\mathbf{a}_i$ denotes unit vectors of the material's privileged directions [83, 22, 46]. As a result, the flow function F depends not only on the stress state, but also on the structural tensors $\mathbf{M}_i$

$$\bar{F}(\boldsymbol{\sigma}, \mathbf{M}_i) = \sqrt{\boldsymbol{\sigma} : \mathbf{C}(\mathbf{M}) : \boldsymbol{\sigma}} - \sigma_F \tag{4.68}$$

where $\bar{F}$ is intended to involve only the second invariant of the stress deviator J_2. In this Equation $\overset{4}{\mathbf{C}}$ is a fourth order anisotropy tensor, which is defined as

$$\mathbf{C} = \alpha\, \mathbf{I}^{(4)} + \beta \sum_{i=1}^{n} w_i\, (\mathbf{M}_i \otimes \mathbf{M}_i)\,. \tag{4.69}$$

Here, α and β are scalar anisotropy parameters determined experimentally, while w_i is a weighting factor reflecting the intensity of the material properties in the corresponding direction. Applying $\beta = 0$ and $\alpha = 1$, the corresponding isotropic flow function is recovered.
All the anisotropic models discussed so far are based basically on the analytical solution, which require simplified geometry, boundary conditions and material behavior to be solvable. Karafillis and Boyce (1993) [51] introduced a refined approach that leveraged linear stress transformation and arbitrary nonlinearity while overcoming limitations like restricted stress states and anisotropic behavior. The Karafillis–Boyce model (KB93) applies a linear transformation of the Cauchy stress to derive an Isotropic Plasticity Equivalent (IPE) deviatoric stress, which was later adopted in other anisotropic models (e.g. [10, 68]). This modeling approach has been effectively applied to metal forming processes, as demonstrated by [16, 101, 54]. The "IPE

stress transformation" is defined as

$$\widetilde{\mathbf{S}} = \overset{4}{\mathbf{L}} : \boldsymbol{\sigma} \tag{4.70}$$

where $\overset{4}{\mathbf{L}}$ is a fourth-order transformation tensor, $\boldsymbol{\sigma}$ is the actual stress tensor of the anisotropic material, and $\widetilde{\mathbf{S}}$ is the resulting Isotropic Plasticity Equivalent (IPE) stress tensor, which is also deviatoric (traceless). The idea is to replace the actual stress tensor $\boldsymbol{\sigma}$ with the transformed IPE tensor $\widetilde{\mathbf{S}}$. For example, the anisotropic von Mises yield criterion becomes

$$F(\boldsymbol{\sigma}') = \sqrt{\frac{3}{2}(\boldsymbol{\sigma}' : \boldsymbol{\sigma}')} - \sigma_F \implies \bar{F}(\widetilde{\mathbf{S}}) = \sqrt{\frac{3}{2}(\widetilde{\mathbf{S}} : \widetilde{\mathbf{S}})} - \bar{\sigma}_F = \widetilde{\sigma} - \bar{\sigma}_F \tag{4.71}$$

where $\boldsymbol{\sigma}'$ refers to the stress deviator and $\bar{\sigma}_F$ to the mean yield stress in different directions and $\widetilde{\sigma}$ to the equivalent transformed stress. The main challenge in this approach is to identify the components of the transformation tensor $\overset{4}{\mathbf{L}}$. Its structure, particularly the zero entries, is the same as the elasticity tensor due to the symmetry condition. For example, in orthotropic materials, $\overset{4}{\mathbf{L}}$ has 9 independent components to be determined. In the isotropic case, $\overset{4}{\mathbf{L}}$ must leave the stress deviator unchanged. In anisotropic case, it must be transformed itself according to the material orientation as described in Eq. 4.28. Finally, an error function (E) can be defined to identify the components of tensor $\overset{4}{\mathbf{L}}$ based on experimental data

$$E(L_{ij}) = \sum_{k=1}^{n} \left(\frac{\widetilde{\sigma}_{exp}^{(k)}}{\bar{\sigma_F}} - 1 \right)^2 \tag{4.72}$$

where k refers to the number of experimental data available from different tests.

IPE approach is an elegant way, especially for numerical implementation for models that are independent of the hydrostatic stress component. In order to generalize the IPE method also for porous materials whose yielding behavior depends also on the hydrostatic stress component, Smith et al. [91] proposed a new transformation tensor $\overset{*}{\mathbf{L}}$, where

$$\overset{*}{\mathbf{L}} = \mathbf{L} + \frac{1}{3}\mathbf{I} \otimes \mathbf{I}. \tag{4.73}$$

Here, $\overset{*}{\mathbf{L}}$ is the new fourth-order pressure-augmented isotropic projection tensor, $\mathbf{L}$ is the original deviatoric fourth-order projection tensor from KB93, and $\mathbf{I}$ is the second-order identity tensor. This leads to a new, non-deviatoric form of the IPE tensor, termed the Pressure-augmented Isotropic Plasticity Equivalent (PIPE) tensor,

$$\overset{*}{\mathbf{S}} = \overset{*}{\mathbf{L}} : \boldsymbol{\sigma} \; = \; (\mathbf{L} + \frac{1}{3}\mathbf{I} \otimes \mathbf{I}) : \boldsymbol{\sigma} \tag{4.74}$$

The structure of the IPE tensor indicates that the PIPE stress can be additively decomposed into the following two tensors

$$\overset{*}{\mathbf{S}} = \; \widetilde{\mathbf{S}} + \mathbf{P} \tag{4.75}$$

where $\widetilde{\mathbf{S}}$ denotes the IPE tensor as defined in Eq. 4.70, and $\mathbf{P}$ represents the pressure tensor, which due to the Eq. 4.74 is defined by

$$\mathbf{P} = -p\,\mathbf{I}. \tag{4.76}$$

Here, p refers to the hydrostatic pressure of the Cauchy stress tensor. Therefore, the results from Equations 4.75 and 4.76 demonstrate that the anisotropic pressure-dependent yield function associated with the PIPE tensor $\overset{*}{\mathbf{S}}$ depends on both the $\mathbf{L}$ and the Cauchy stress tensor $\boldsymbol{\sigma}$. Consequently, the corresponding anisotropic Drucker–Prager yield criterion (Eq. 4.56) derived from this framework is given by

$$\overset{*}{F}(\overset{*}{\mathbf{S}}) = \sqrt{3\widetilde{J}_2(\widetilde{\mathbf{S}})} - \alpha I_1(\boldsymbol{\sigma}) - \kappa = 0 \tag{4.77}$$

This confirms that the projection tensor $\mathbf{L}$ from the KB93 is fully sufficient to characterize an anisotropic, pressure-dependent yield function as well.

5

Fully Resolved Simulation and Homogenization

5.1 Introduction to the FEM

The Finite Element Method (FEM) is a numerical technique used to find approximate solutions to complex engineering and physical problems, those that involve partial differential equations (PDEs). FEM has become one of the most powerful and widely used tools in fields such as structural analysis, heat transfer, fluid dynamics, and electromagnetics. Its success lies in its flexibility and adaptability to complex geometries, complex boundary conditions and diverse material properties. The method is based on dividing a large and complex problem into smaller and simpler parts called "finite elements", which are connected at discrete points known as nodes. By solving these smaller, discrete problems, FEM builds an approximate solution to the entire problem.
Finite Element Analysis (FEA) is divided into three main phases: **preprocessing**, where a computable model is created by defining geometry, material properties, boundary conditions and discretization of geometry; **solving**, where the global system of equations is solved; and **postprocessing**, where results are evaluated and visualized for interpretation.

In FEA, variables are categorized as primary or secondary on the basis of their role in solving the problem. Primary variables are the main unknowns that the FEA seeks to solve directly, such as displacements in structural analysis or temperature in thermal analysis. These primary variables are typically calculated at the nodes. These variables are then interpolated within the elements using the node values. The interpolation is carried out using the shape functions, which are typically polynomial functions due to their continuously differentiable or integrable nature. The field quantities generated by interpolation within the elements can be used to calculate secondary variables such as stress or strain. This calculation is performed through numerical integration at specific locations called integration points (or Gauss points). Increasing the discretization fineness or choosing a higher order polynomial function for interpolation enhances result accuracy, but also significantly increases computational effort. Therefore, choosing the appropriate mesh and element type is a challenging task that requires experience. A balance must be achieved to ensure that the results are sufficiently accurate while keeping computational effort manageable.
This concept is referred to as the **convergence study**. It is a process used to ensure that the simulation results are accurate and independent of the mesh size or element discretization. It involves systematically refining the mesh typically by increasing the number of elements and observing how the results (such as stress, strain, or displacement) change with each refinement. Once the results converge to a consistent value (no significant change in results), the solution can be considered accurate. At this point, the density of the mesh is likely sufficient for a reliable solution.

5.2 Plane Stress State and Element Formulation

In the field of continuum mechanics, a plane stress state refers to a condition in which the stress components perpendicular to a specific plane (usually the thickness direction) are negligible compared to the in-plane stresses. This assumption is valid in thin flat structures such as plates and shells, where the thickness is much smaller than the other dimensions and the out-of-plane forces are minimal. Under plane stress state, only the normal stresses (σ_{11} , σ_{22}) and shear stress (τ_{12}) are considered, simplifying analysis and enabling two-dimensional modeling.
Depending on the dimension and complexity of the model, different types of elements can be chosen, each differ in terms of dimensionality and number of nodes as well as number of integration points. Theoretically, volume

elements or surface elements can be used for the spatial discretization of auxetic sheets. Volume elements are typically used for massive or thick-walled components. For thin-walled components, as utilized in this work, the thickness resolution would be significantly lower than the dimensions in the plane of the component, making the use of volume elements less suitable. In addition, the computation time increases significantly as the number of elements grows. In practice, volume elements require approximately eight times as much computation time as equivalent surface elements [15]. Figure 5.1 shows a continuum element as an example of a volume element, as well as 2D shell elements with different numbers of integration points.

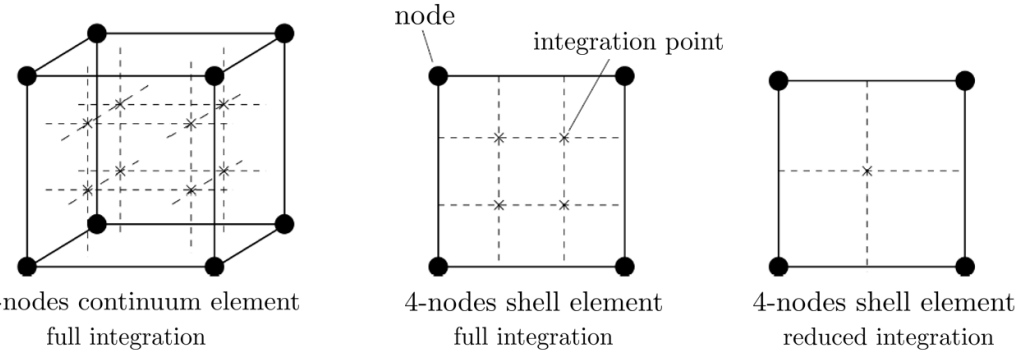

Figure 5.1: Continuum element and shell elements including nodes and integration points.

For computational efficiency reasons, linear shell elements, which use bilinear shape functions, are used for auxetic sheets. The governing equations are integrated over the element, which is performed numerically by selecting appropriate integration points. For bilinear shell elements, numerical integration is carried out based on four integration points. By using reduced integration, the number of integration points is reduced to one per surface, decreasing the computation time and avoiding locking effects (shear locking and volumetric locking). First-order elements with full integration suffer from the problem of shear locking. **Shear locking** results in an excessively high element stiffness under bending load because the corresponding deformation modes cannot be accurately represented by the shape functions. The cause of this issue lies in the element edges, which cannot bend due to the linear order. Even fully integrated quadratic elements can experience shear locking when the bending load becomes too large. In reduced integration, the value of the volume integral is determined only by the support values at the center

of the element. Linear elements with reduced integration tend to exhibit a stiffness that is too low. Reduced integration leads to a rank deficiency when calculating the element stiffness matrix, and thus, it is no longer solved exactly. This numerical problem is known as **hourglassing** and can lead to unphysical solutions. Hourglassing occurs when, during bending the element, no strain energy is generated due to a single integration point, meaning that the element cannot resist the applied load.
In contrast to shear locking, there are stabilization methods available for hourglassing to minimize the problem. ABAQUS® provides a range of suitable element formulations, integration methods, and stabilization techniques. Details can be found in the ABAQUS® user's manual [69].

5.3 Fully Resolved Simulation of Auxetic Sheets

A fully resolved simulation or in other words a micromodel simulation refers to a numerical model that captures all relevant physical details of a structure, including fine-scale stress distributions, deformations, and material behavior, without relying on simplifications or submodels. All simulations in this study were performed using commercial FE software ABAQUS® (Dassault Systems). The CPS4R element type (4-node bilinear plane stress quadrilateral, reduced integration) with a seed size of 0.5 mm is used. The seed size of 0.5 is chosen so that the struts (thin webs) can be meshed by two elements. Young's modulus of 60.04 GPa and Poisson's ratio of 0.33 as well as the hardening parameters (Table 5.1) were applied as input parameters for the fully resolved elasto-plastic simulation of the corresponding auxetic sheet, which were determined from the experimental flow curve of the bulk AlMg3 discussed in Section 3.2 (see Fig. 5.2).

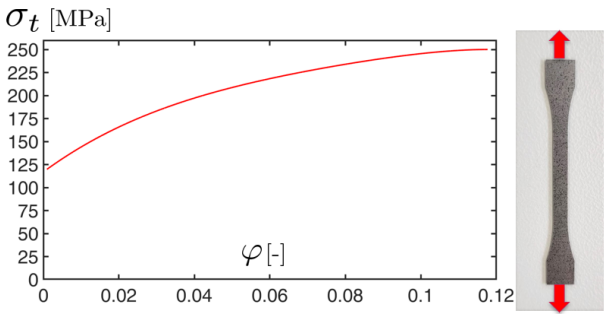

Figure 5.2: Flow curve of bulk AlMg3 sample.

σ_t (MPa)	φ [-]
119.64	0
126.24	0.004151
158.40	0.017051
195.00	0.041381
227.84	0.093941
232.70	0.127941

Table 5.1: Input Parameters for the hardening simulation.

Strain-controlled tensile tests were simulated, where a total displacement of 9 mm was specified, which corresponds to approximately 10% global strain. As boundary conditions, a displacement of $U2 = 4.5$ mm is applied to both ends of the specimen in clamping holes so that the center of the specimen remains stationary during deformation. The other degrees of freedom, i.e. the displacement $U1$ in the e_1 direction and the rotation $UR3$ around the e_3 axis are fixed, as illustrated in Fig. 5.3.

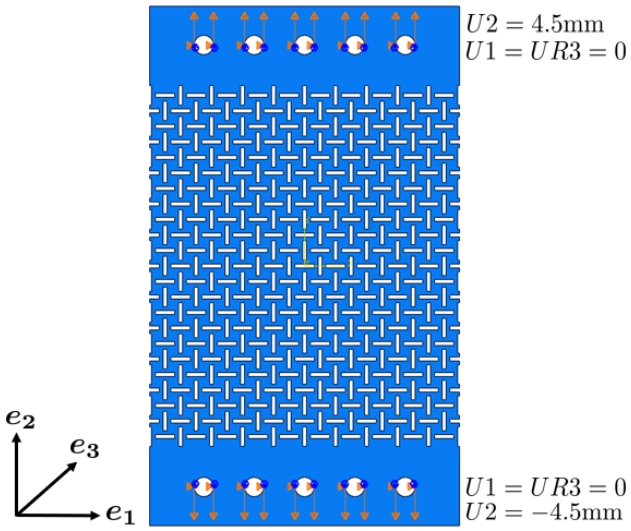

Figure 5.3: representation of boundary conditions applied to the auxetic sheets for fully resolved simulations.

5.3.1 Reference Auxetic Sheet with $AR = 5$

At first, the fully resolved simulation was carried out on the reference auxetic sheet with $AR = 5$. The deformed auxetic sheet with cut-out unit cell in the center of the sheet after 10%-global strain are shown in Figure 5.4. The micromodel results with respect to the von Mises equivalent stress distribution are in total agreement with the experimental results of the local strains determined by DIC, which are represented in Section 3.5. As can be seen in Fig. 5.4, the maximum stresses occur in the struts that are responsible for the rotation of the squares. In the central areas of the squares, however, low stresses occur, so that these stress values are below the yield point of AlMg3 (approx. 120 MPa). This means that these areas do not experience any plastic deformation at all, but they exhibit only rigid-body rotations during the tensile test.

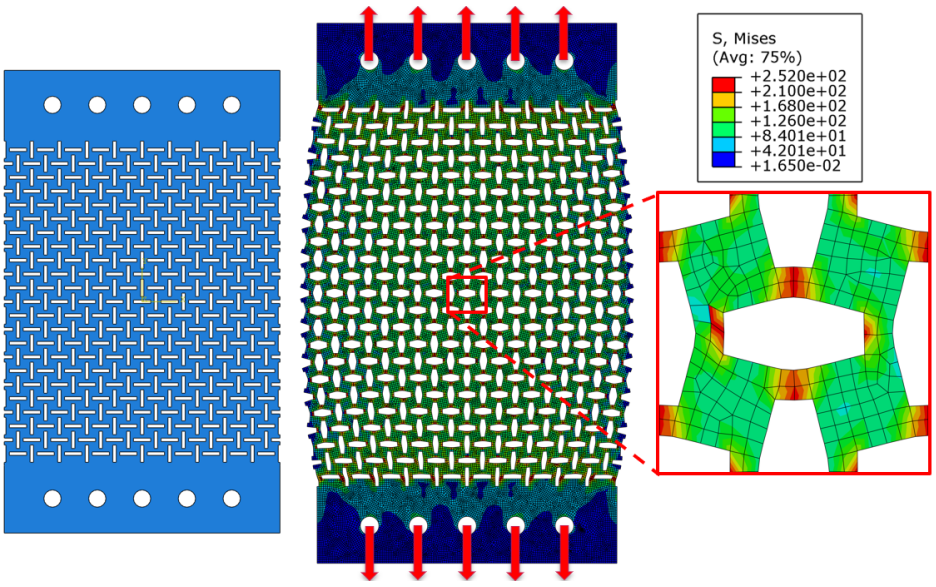

Figure 5.4: Undeformed reference auxetic sheet whit $AR = 5$ (left) and corresponding deformed state including cut-out unit cell subjected to uniaxial tensile test after 10%-global strain (right). The contour refers to the von Mises stress.

As shown in Figure 5.5, there is a small deviation between the global stress-strain curves obtained from the experiment and the simulation. However, this is quite typical. The difference occurs because simulations are always based on idealized conditions and boundary constraints, unlike real-world experiments. In the experiment, local effects may have influenced the outcome such as localized plastic deformation around the clamping holes or minor measurement errors in tracking machine displacement, causing the experimental stress-strain curve to appear slightly softer.
In general, as can be seen in Fig. 5.5, both the local and global deformations as well as the global stress-strain curves of simulation and experiment agree well with each other. The minor deviation observed in the initial elastic region is attributed to the idealized conditions in the simulation—namely, perfect material homogeneity and ideal boundary conditions, which result in an overestimation of the specimen's stiffness. This suggests that the simulations accurately capture the auxetic behavior and could potentially substitute for real experiments if needed.

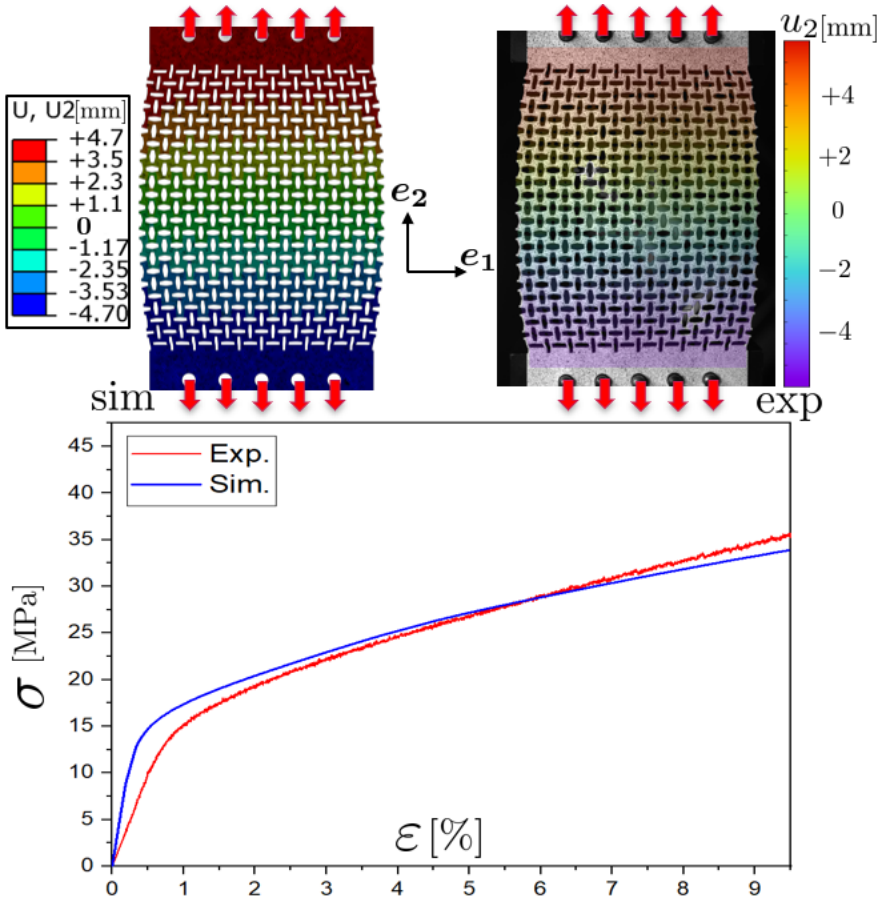

Figure 5.5: The deformed reference auxetic sheets ($AR = 5$) in simulation (left) and experiment (right) and the corresponding global stress-strain curves subjected to uniaxial tensile test after approx. 10% global strain for both simulation and experiment.

5.3.2 Anisotropy Investigations

In order to analyze the type of anisotropy present in the auxetic structure, various auxetic sheets with an identical aspect ratio of $AR = 5$ were designed, featuring different orientation angles. These angles progressively increased from 0° to 90° in 5-degree intervals. All these auxetic sheets with different orientation angles (θ) were subjected to uniaxial tensile tests up to approximately 10% global strain, as illustrated in Figure 5.6 for the sheet with an orientation angle of $\theta = 45°$.

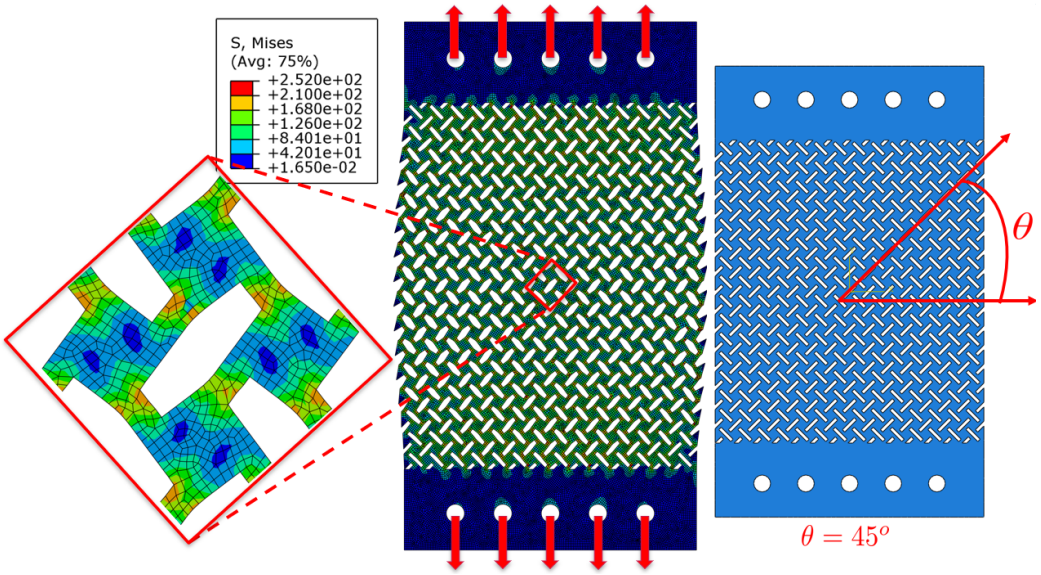

Figure 5.6: Undeformed auxetic sheet whit $AR = 5$ and orientation angle of θ =45° (right) and corresponding deformed state including cut-out unit cell subjected to uniaxial tensile test after 10% global strain (left).

At the microscale, as evidenced by the comparison of Figures 5.4 and 5.6, the von Mises stress in the struts decreases as the orientation angle increases. This phenomenon on the macroscale leads to a decline in global stress, which is responsible for the deformation of the entire sheet. This decrease in global stresses can also be observed in the corresponding global stress-strain curves for the specimens with 0° to 45° rotated pattern (see Fig. 5.7a). Young's moduli and yield strengths decrease continuously with increasing orientation angle (θ). For the specimens from 45° to 90° rotated pattern, the mechanical properties repeat in such a way that the stress-strain curves related to the specimen with θ° rotated pattern are quite identical to the specimen with $(90 - \theta)$° rotated pattern (see Fig. 5.7b).

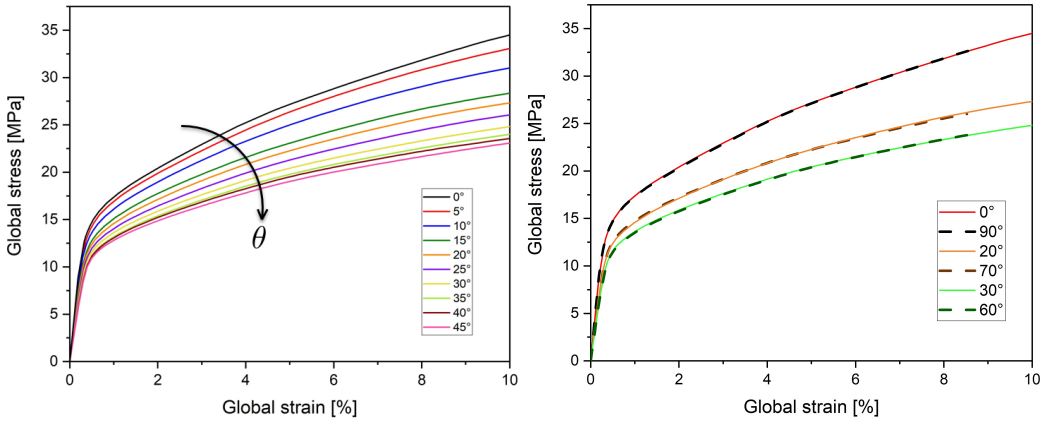

(a) $0° \leq \theta \leq 45°$ (b) $0° \leq \theta \leq 90°$

Figure 5.7: Global stress-strain curves related to the specimens with different pattern orientation angles (θ).

It is obvious that after 90° rotation of the pattern, the initial state is recovered, which corresponds to orthotropic materials based on Tab. 4.1. Furthermore, referring to the stress-strain curves in Fig. 5.7, it was also derived that the 45° axis forms an additional axis of symmetry in this structure, which corresponds to the so-called **tetragonal** materials due to Tab. 4.1. A spatial representation of the tetragonal symmetry is shown in Fig. 5.8, where four of the five planes of symmetry lie at distances of 45° from each other and the fifth plane of symmetry lies transverse to all of them. The corresponding normal vectors to the planes of symmetry are denoted by $\boldsymbol{a1} - \boldsymbol{a5}$.

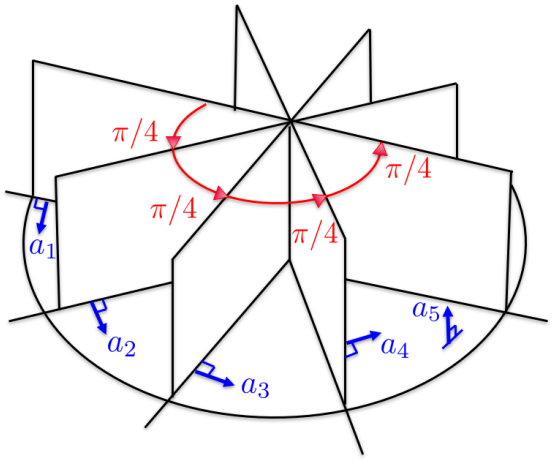

Figure 5.8: Spatial illustration of the five planes of symmetry characterizing tetragonal symmetry. The normals to the five planes are denoted by $\boldsymbol{a1}-\boldsymbol{a5}$.

5.4 Numerical Homogenization

Numerical homogenization is a powerful computational technique used to evaluate and predict the effective properties of heterogeneous materials by bridging the micro- and macroscales. It ensures that the chosen RVE reflects the macroscopic behavior of the material without bias or excessive computation. The representative volume element (RVE) is an important concept in the field of computational mechanics, representing the smallest volume of material that can statistically capture the macroscopic properties of a larger structure [72]. The concept of RVE was first introduced by Hill [48] and Hashin [43] and is currently widely used for the homogenization of heterogeneous microstructures such as composite and porous materials. Fig. 5.9 provides a schematic illustration of the homogenization process. To apply continuum-mechanical principles to heterogeneous materials, it is crucial to establish a way to transition from a heterogeneous structure to a homogeneous structure.

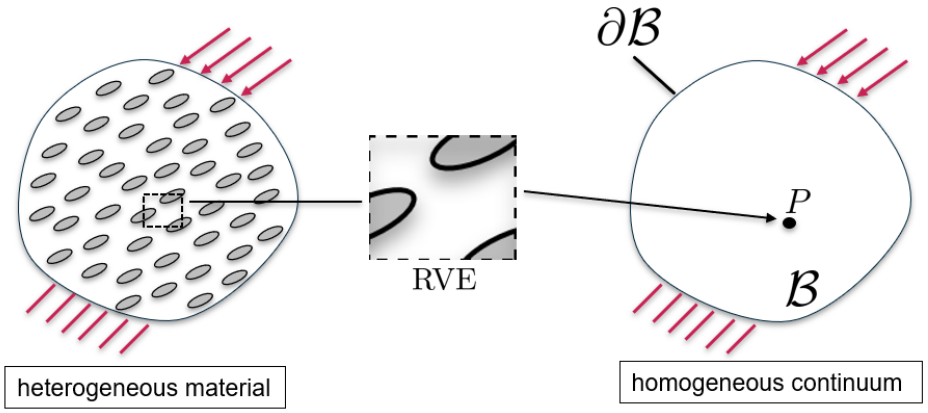

Figure 5.9: Transition from the physical body to the homogenized continuum.

For this purpose, an RVE is chosen, whose properties result from the integral mean over the entire volume element v at the microscale. The mean operator is defined for any unweighted field quantity by Eq. 5.1

$$\bar{(\bullet)} = \frac{1}{v}\int_v (\bullet)\,\mathrm{d}v \tag{5.1}$$

In this equation, $\bar{(\bullet)}$ denotes any arbitrary macroscopic variable, while $(\bullet)$ represents the corresponding microscopic counterpart. The transition from microscopic variables to macroscopic variables is called *homogenization* and the reverse process is called *localization* [88]. By applying divergence theorem and Gauss's integral theorem, Equation 5.1 can be reformulated in terms of boundaries integration. This boundary formulation is then used to compute the effective (macroscopic) strain and stress within an RVE as follows:

$$\bar{\boldsymbol{\varepsilon}} = \frac{1}{|\Omega|}\int_{\partial\Omega} \boldsymbol{u}\otimes\boldsymbol{n}\,\mathrm{d}a \tag{5.2}$$

$$\bar{\boldsymbol{\sigma}} = \frac{1}{|\Omega|}\int_{\partial\Omega} \boldsymbol{t}\otimes\boldsymbol{x}\,\mathrm{d}a \tag{5.3}$$

where $\boldsymbol{u}$ denotes the displacement field on the RVE boundary, $\boldsymbol{n}$ is the unit normal vector, $\boldsymbol{t}$ refers to the stress vector acting on the RVE boundary and $\boldsymbol{x}$ is position vector. $\mathrm{d}a$ and $|\Omega|$ are the differential element along the boundary and the area of the RVE respectively [72]. The tensor product $\boldsymbol{u}\otimes\boldsymbol{n}$ in Eq. 5.2 captures the directional contribution of the displacement field relative to the RVE boundary orientation, while $\boldsymbol{t}\otimes\boldsymbol{x}$ in Eq. 5.3 forms the corresponding stress tensor arising from the normalized edge forces (stress

vectors).
Using Cauchy's theorem (Eq. 4.17) $\boldsymbol{t}$ can be replaced by the stress tensor $\boldsymbol{\sigma}$ and the corresponding normal vector $\boldsymbol{n}$ as below, in case $\boldsymbol{\sigma}$ is already defined along the RVE boundaries.

$$\bar{\boldsymbol{\sigma}} = \frac{1}{|\Omega|} \int_{\partial\Omega} (\boldsymbol{\sigma} \cdot \boldsymbol{n}) \otimes \boldsymbol{x} \, \mathrm{d}a \tag{5.4}$$

Such boundary-based homogenization approaches are especially useful in FE simulations, where boundary displacements and forces can be directly extracted.
Different boundary conditions can be applied on a homogenized RVE to determine the effective material properties of the entire system. The shape and size of the RVE depend mainly on the randomness of the geometry or microstructure, which has been extensively discussed in the context of multiscale homogenization-based modeling [73, 36, 50, 2, 92]. For mechanical metamaterials such as auxetics, which are regularly composed of periodic unit cells, it is simpler to obtain an appropriate RVE than for materials with arbitrary microstructure. For such materials, the RVE typically consists of one or more unit cells, the number of which is to be determined by comparison with the fully resolved sample. Finite element (FE) analysis is one of the most common methods to deal with these systems. In order for the RVE to be a proper representative for the corresponding infinite system, the boundary effects must be eliminated somehow. This can be achieved by implementing Periodic Boundary Conditions (PBCs). Kinematic periodic boundary conditions are a set of boundary conditions applied often in a FE program, where all opposite pairs of nodes are kinematically coupled with each other, so that they deform in an identical manner and accordingly the boundary effects disappear completely [71, 100, 62].
Periodic boundary conditions are actually linear couplings between the pairs of nodes, which are supposed to be adjusted based on the prescribed load scenario. In strain-controlled simulations, these linear equations must result in the relative motion of all pairs of nodes being equal to the specified displacement in the loading direction. This can be formulated in general for a single node pair as equation (5.5), where A denotes the node number, $i = (1, 2, 3)$ is degree of freedom and a is the constant coefficient that define the relative motion of the nodes and $\widehat{u}$ is a prescribed displacement value [99].

$$a_1 u_i^{A_1} + a_2 u_i^{A_2} = \widehat{u_i} \tag{5.5}$$

Figure 5.10 presents a schematic representation of the expected coupling

structure and the associated linear equations relating the node pairs.

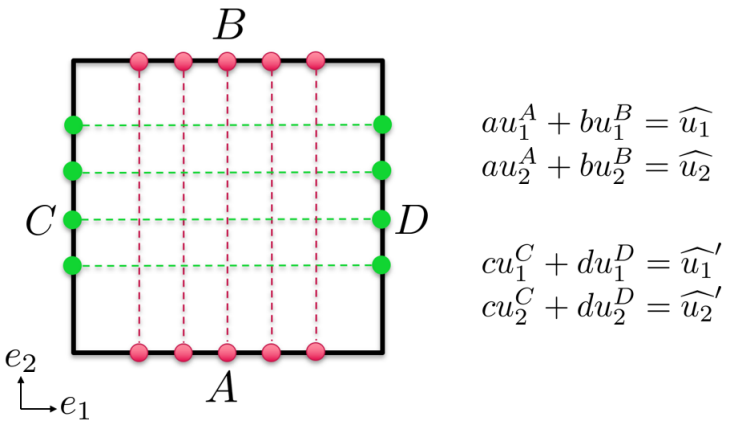

Figure 5.10: Schematic representation of the coupling between node pairs in order to implement PBCs within RVE and associated linear equations for the node pairs AB and CD in 2D.

5.4.1 Influence of Boundary Conditions

As outlined in the previous section, applying periodic boundary conditions (PBCs) to the representative volume element (RVE) is essential for eliminating undesirable edge effects. Fig. 5.11 illustrates the nature of these effects, showing a comparison between a unit cell, a 2×2 cells and a 4×4 cells subjected to uniaxial loading along the $\boldsymbol{e_2}$ direction with standard (non-periodic) boundary conditions. The corresponding cut-outs from a full sheet are shown below each case. The noticeable difference in local deformation patterns between the upper and lower images highlights the impact of edge effects at the locations where external forces are applied. Specifically, the restriction of square rotations near the boundaries alters the local deformation and, consequently, affects the effective material properties. Naturally, the smaller the sample, the more pronounced this influence becomes. Implementing PBCs within the RVE removes these artifacts, ensuring that the derived effective properties accurately reflect those of a larger auxetic structure.

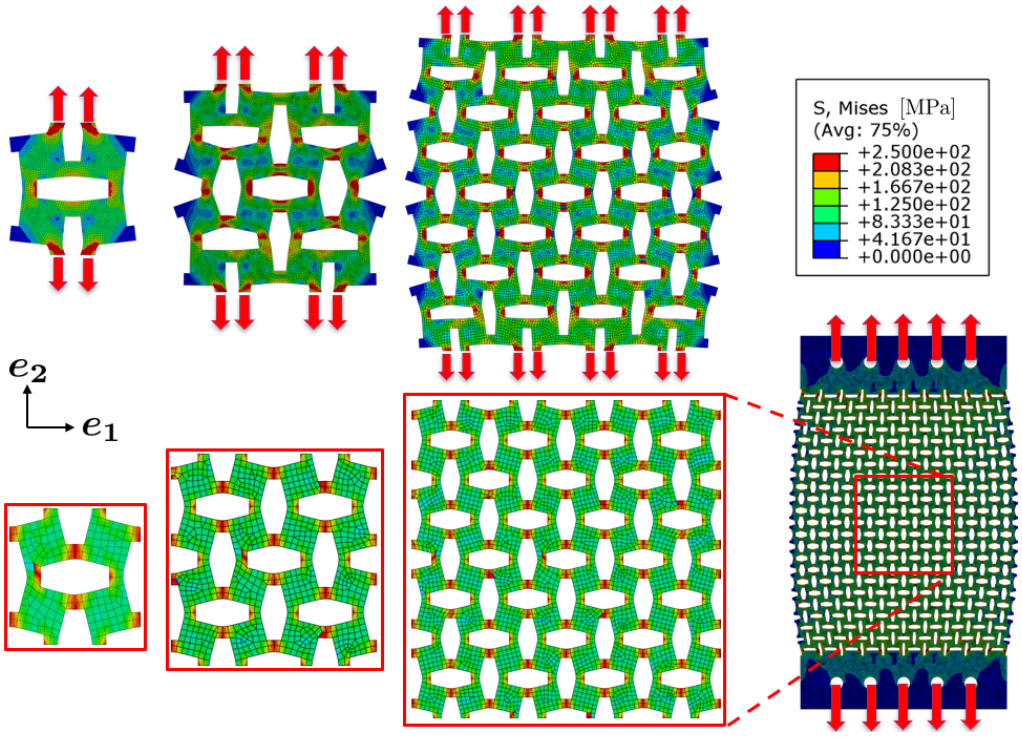

Figure 5.11: Influence of boundary conditions on local deformation. Top: specimens with standard boundaries; bottom: corresponding cut-outs from the full sheet under tensile load.

5.4.2 Periodic Boundary Conditions (PBCs)

Periodic Boundary Conditions (PBCs) are actually a set of boundary conditions in the form of linear equations between the pairs of nodes lying in opposite positions on the boundary. In ABAQUS® these equations can either be written directly in the ABAQUS-Input file or as "SETS" via ABAQUS-CAE in the interaction module under the constraint equations. Depending on how the loads and corresponding deformations should look like, these linear equations have to be adjusted. To implement PBCs, all edge nodes must first be selected and stored in the various SETS. The edge nodes, which are opposite to each other, should be easily identified by a meaningful naming as in Fig. 5.12. Then we need to define a reference point (RP) somewhere outside the model where the prescribed global displacement of the unit cell is to be applied. To avoid rigid body motion of the whole part, one point in the center of the model must be fixed.

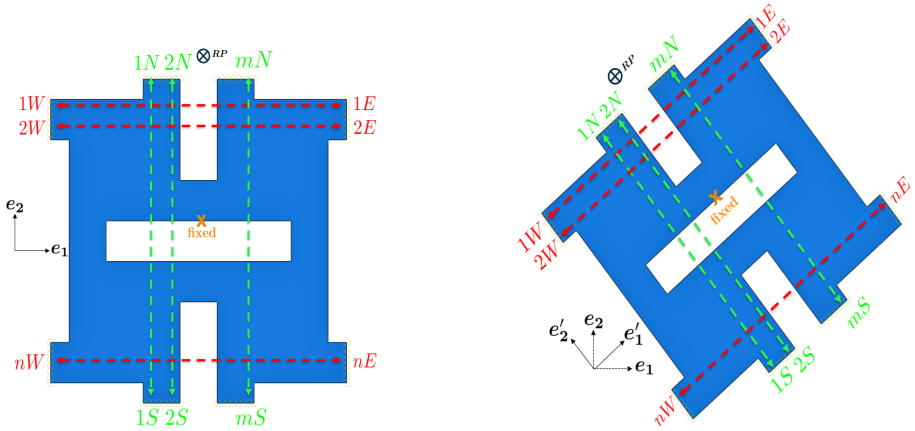

Figure 5.12: Typical way of numbering the node sets at the edges that appear in pairs in the equations when implementing PBCs in case of the standard unit cell (left) and the rotated unit cell (right).

So finally after the above steps we are able to establish the linear equations based on the loading scenario. In general, the equations in the 2D case can be written in four columns, where two columns refer to the node pairs in the loading direction and the other two columns refer to the node pairs perpendicular to the loading direction. The necessary number of equations depends on the number of the edge nodes, or in other words, it depends on the discretization of the model. The finer the model, the more equations have to be set up. The exact number of equations is equal to $n + m$, where 'n' and 'm' correspond to the total number of the nodes on a horizontal and vertical boundary.
For a uniaxial tensile test, the typical equations used to implement the Periodic Boundary Conditions (PBCs) are illustrated in Figure 5.13. In this setup, the displacement vector of the reference point is given as $\boldsymbol{u}^{RP} = [0\ ,\ u_2]$, as represented in Figure 5.14. It should be noted that the relative displacement of the lateral node pairs (nodes on the East-West edges) regarding the $\boldsymbol{u}_1$-direction must remain constant and non-zero. Otherwise, the transverse strain will be zero, preventing the representation of any auxetic effect. This constant (l_1) should be formulated as $l_1 = u_1^{rE} - u_1^{rW}$, where the node number 'r' refers to a random pair of nodes in the East-West direction.

$u_1^{1N} - u_1^{1S} = u_1^{RP}$	$u_2^{1N} - u_2^{1S} = u_2^{RP}$	$u_1^{1E} - u_1^{1W} = l_1$	$u_2^{1E} - u_2^{1W} = 0$
$u_1^{2N} - u_1^{2S} = u_1^{RP}$	$u_2^{2N} - u_2^{2S} = u_2^{RP}$	$u_1^{2E} - u_1^{2W} = l_1$	$u_2^{2E} - u_2^{2W} = 0$
⋮	⋮	⋮	⋮
$u_1^{nN} - u_1^{nS} = u_1^{RP}$	$u_2^{nN} - u_2^{nS} = u_2^{RP}$	$u_1^{nE} - u_1^{nW} = l_1$	$u_2^{nE} - u_2^{nW} = 0$

Figure 5.13: Implementation of PBCs equations for a tensile test based on the numbering in Fig. 5.12.

After applying the PBCs, the simulation results are presented in Figures 5.14 and 5.15. To provide a clearer comparison between homogenized and non-homogenized unit cells, the corresponding simulation results for conventional boundary conditions (without PBCs) are also included. As can be clearly seen in Figure 5.14, the edges of the samples with PBCs remain straight during deformation. Consequently, the stress distribution at the edges is no longer close to zero, as is the case for a unit cell without PBCs. This behavior reflects a unit cell embedded within a larger sheet surrounded by many other unit cells, and accordingly influences the global behavior of the unit cell in such a way that it is more close to the global behavior of the entire sheet. This consideration is crucial for identifying an appropriate RVE, which will be discussed in the next section.

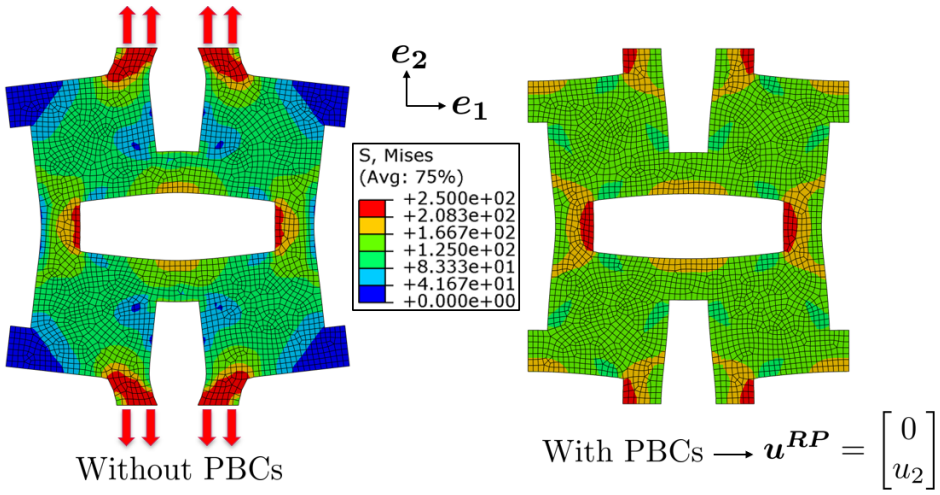

Figure 5.14: The deformed unit cell subjected to uniaxial tensile test with conventional boundary conditions (without PBC) and with Periodic Boundary Conditions (PBCs).

To ensure correct implementation of PBCs, the displacement fields along the two coordinate axes are also shown in Fig. 5.15. It illustrates that the pairs of east-west nodes along the edges of the unit cell with PBCs exhibit minimal relative u_1-displacements, whereas the unit cell without PBCs shows significantly larger relative u_1-displacements. In contrast, the transverse displacements at the center of the unit cell behave differently, showing greater relative displacements in the case of PBCs. This behavior arises from boundary effects rather than the intrinsic deformation of the unit cell. However, the equal transverse displacements observed across all east-west node pairs at the edges confirm the correct implementation of PBCs in the transverse direction.
Observing the u_2-displacements indicates that in both cases, the North-South edge nodes exhibit the same relative axial displacement (approximately 0.32 mm). However, in the case without PBCs, the displacements of the north and south nodes are completely symmetrical in contrast to the unit cell with PBCs. Implementation of PBCs ensures only that the relative movement of the node pairs is consistent and follows the prescribed conditions, but it does not necessarily result in symmetric manner.

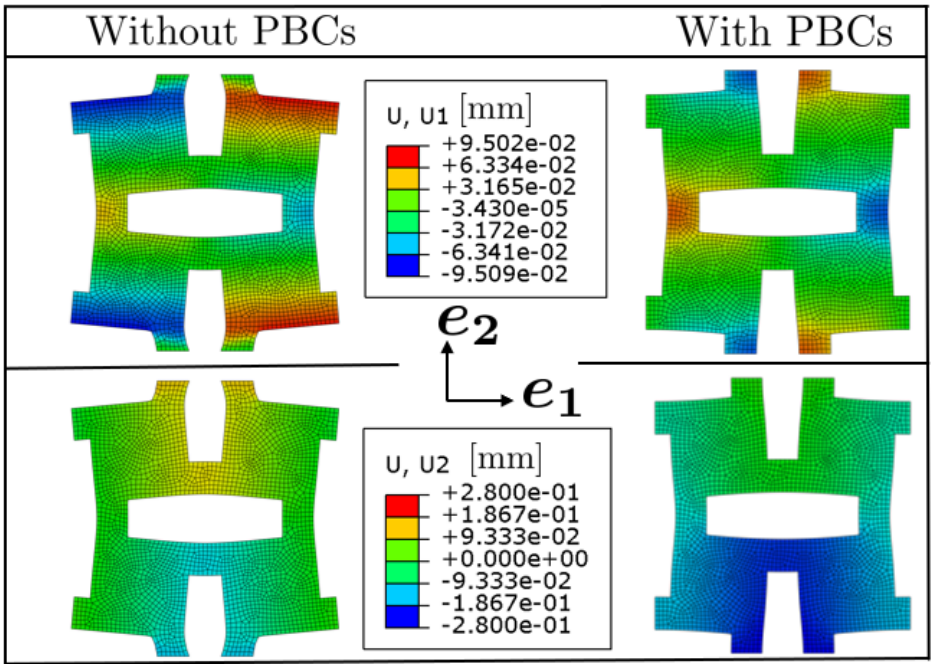

Figure 5.15: The deformed unit cell subjected to uniaxial tensile test with conventional boundary conditions (without PBC) and with Periodic Boundary Conditions (PBCs). The contours refer to the axial (u_2) and transverse (u_1) displacement.

Implementing PBCs for unit cells with local orientation is more challenging, because they must be homogenized in their local orientation. This means that the typical PBCs equations must be valid in local coordinate systems. However, since all equations and relationships should ultimately be expressed consistently in the global coordinate system, a coordinate transformation is necessary. The theory behind these coordinate transformation relationships has been thoroughly discussed in Section 4.3.1. Hence, they are just applied here without going into details.
The corresponding PBCs equations for a unit cell with local orientation angle θ subjected to a uniaxial tensile test in global $\boldsymbol{e_2}$-direction are shown in Figure 5.16 for an arbitrary North-South node pair and in Figure 5.17 for an arbitrary East-West node pair.

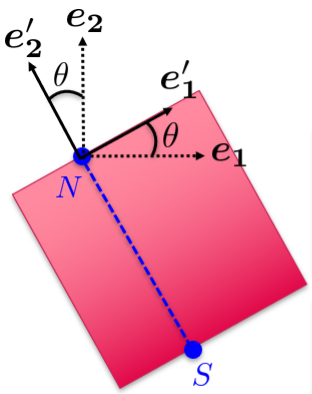

$$\boldsymbol{u^{RP}} = \begin{bmatrix} 0 \\ u \end{bmatrix} \qquad \boldsymbol{u'^{RP}} = \begin{bmatrix} u'_1 \\ u'_2 \end{bmatrix} = \begin{bmatrix} u\,sin(\theta) \\ u\,cos(\theta) \end{bmatrix}$$

$$u_1'^N - u_1'^S = u_1'^{RP}$$
$$[u_1^N\,cos(\theta) - u_2^N\,sin(\theta)] - [u_1^S\,cos(\theta) - u_2^S\,sin(\theta)] = u^{RP}\,sin(\theta)$$

$$u_2'^N - u_2'^S = u_2'^{RP}$$
$$[u_1^N\,sin(\theta) + u_2^N\,cos(\theta)] - [u_1^S\,sin(\theta) + u_2^S\,cos(\theta)] = u^{RP}\,cos(\theta)$$

Figure 5.16: Typical equations to implementing PBCs for a unit cell with local orientation of θ for an arbitrary Nord-South node pair subjected to uniaxial tensile test in global $\boldsymbol{e_2}$-direction.

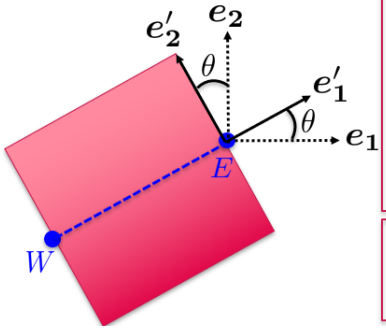

$$u_1'^E - u_1'^W = l_1$$
$$[u_1^E\,cos(\theta) - u_2^E\,sin(\theta)] - [u_1^W\,cos(\theta) - u_2^W\,sin(\theta)] = l_1$$

$$l_{1=} u_1'^{E_n} - u_1'^{W_n}$$
$$l_1 = [u_1^{E_n}\,cos(\theta) - u_2^{E_n}\,sin(\theta)] - [u_1^{W_n}\,cos(\theta) - u_2^{W_n}\,sin(\theta)]$$

$$u_2'^E - u_2'^W = 0$$
$$[u_1^E\,sin(\theta) + u_2^E\,cos(\theta)] - [u_1^W\,sin(\theta) + u_2^W\,cos(\theta)] = 0$$

Figure 5.17: Typical equations to implementing PBCs for a unit cell with local orientation of θ for an arbitrary East-West node pair subjected to uniaxial tensile test in global $\boldsymbol{e_2}$-direction.

Such implementations are more straightforward in ABAQUS®-CAE. All that is required is to define a local coordinate system and write the equations in the local framework. ABAQUS® then automatically handles the necessary transformations from the local to the global coordinate system.
As an example, a unit cell with a local orientation of $\theta = 30°$ was considered. The unit cell was subjected to a uniaxial tensile test in the global $\boldsymbol{e_2}$-direction using the PBC implementation, with a prescribed global displacement of $\boldsymbol{u^{RP}}$

=[0 , 0.32] in mm along the $\boldsymbol{e_2}$-direction.
Figure 5.18 illustrates the local von Mises stress distribution in the unit cell with PBCs with a 30° orientation. As shown, all free edges are already under stress, which is expected due to the homogenization process. In the center of the squares, the stress is lower compared to the unit cell without a local orientation, as shown in Figure 5.14. This difference arises because the squares in the oriented unit cell can rotate due to the local orientation, unlike those in the unit cell without orientation.

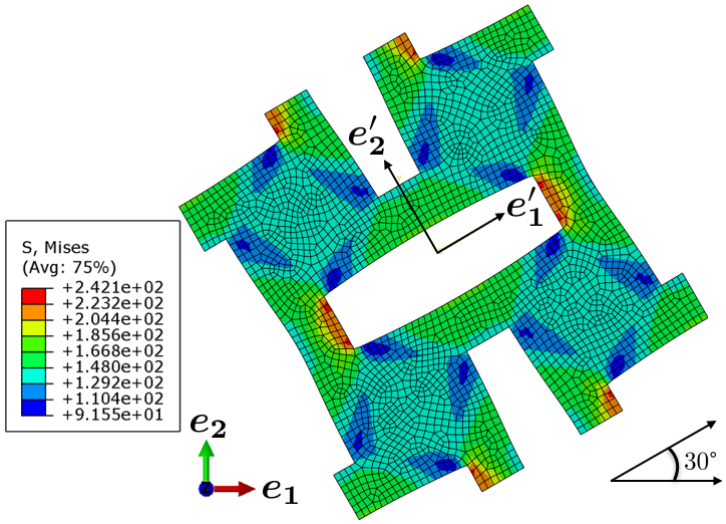

Figure 5.18: The deformed unit cell with $\theta = 30°$ local orientation subjected to uniaxial tensile test with Periodic Boundary Conditions (PBCs). The contours refer to the von Mises stress in [MPa] after approx. 4% global strain.

The corresponding displacement fields are also illustrated in Figure 5.19. It should be noted that the contours u_1 and u_2 are based on the local coordinate system ($\boldsymbol{e'_1}$,$\boldsymbol{e'_2}$) and not on the global coordinate system ($\boldsymbol{e_1}$,$\boldsymbol{e_2}$). As shown in Figure 5.19, the East-West edges of the unit cell have remained straight during the deformation. This indicates that the corresponding pairs of nodes on these edges have the same relative displacements from each other in both directions.
Regarding the North-South nodes, the relative displacements u_1 and u_2 for all node pairs correspond to the displacement vector $\boldsymbol{u'^{RP}}$, derived from the transformation of the global displacement vector $\boldsymbol{u^{RP}}$, as explained in Fig. 5.16, where $\boldsymbol{u^{RP}}$ =[0 0.32].

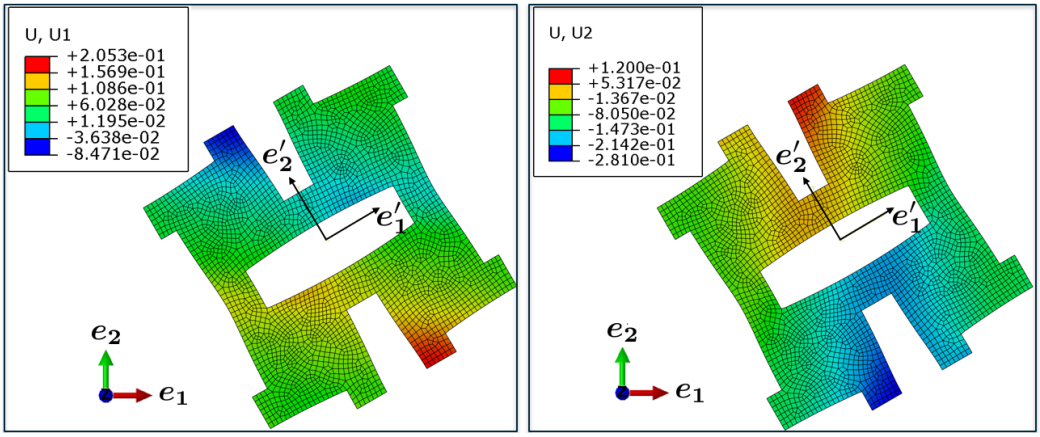

Figure 5.19: The deformed unit cell with $\theta = 30°$ local orientation subjected to uniaxial tensile test with Periodic Boundary Conditions (PBCs). The contours refer to the local displacement fields U_1 and U_2 in [mm] after approx. 4% global strain.

To provide a better understanding of the form of the PBCs equations, another example is presented here as well, illustrating the implementation of PBCs for a simple shear test. The equations are shown in Figure 5.20. In this case, the equations are nearly identical to those for the uniaxial tensile test, except that the relative displacement of the lateral node pairs (node pairs on the East-West edges) in the $\boldsymbol{e_1}$-direction must also be zero. This ensures that pure shear does not induce a normal strain $\boldsymbol{\varepsilon_{11}}$ locally.

$$
\begin{array}{cccc}
u_1^{1N} - u_1^{1S} = u_1^{RP} & u_2^{1N} - u_2^{1S} = u_2^{RP} & u_1^{1E} - u_1^{1W} = 0 & u_2^{1E} - u_2^{1W} = 0 \\
u_1^{2N} - u_1^{2S} = u_1^{RP} & u_2^{2N} - u_2^{2S} = u_2^{RP} & u_1^{2E} - u_1^{2W} = 0 & u_2^{2E} - u_2^{2W} = 0 \\
\vdots & \vdots & \vdots & \vdots \\
u_1^{nN} - u_1^{nS} = u_1^{RP} & u_2^{nN} - u_2^{nS} = u_2^{RP} & u_1^{nE} - u_1^{nW} = 0 & u_2^{nE} - u_2^{nW} = 0
\end{array}
$$

Figure 5.20: Implementation of PBCs equations for a simple shear test based on the numbering in Fig. 5.12.

Finally, the simulation results for the simple shear test, both with and without PBCs, are presented in Figure 5.21. It can be observed that the edges remain straight during shearing, which also represents the deformation of a unit cell within a larger sheet surrounded by multiple other unit cells.

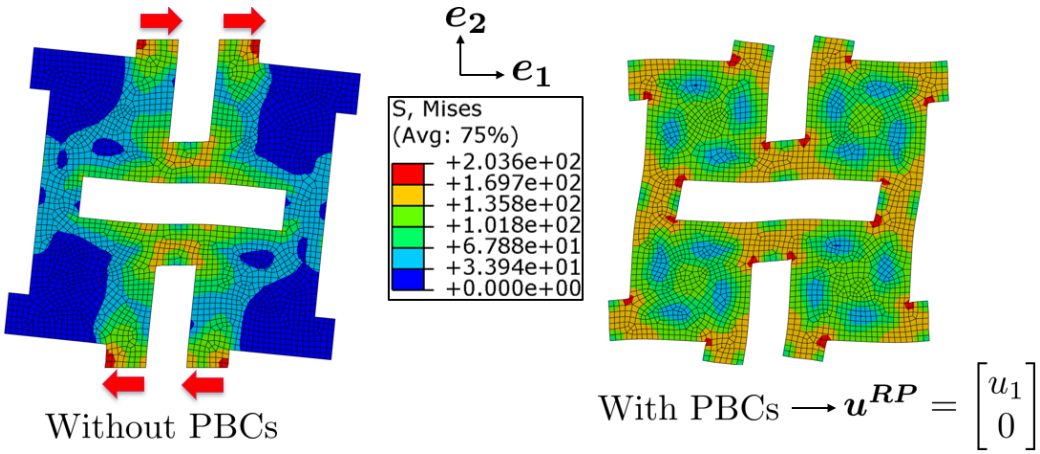

Figure 5.21: The deformed unit cell subjected to simple sshear test with conventional boundary conditions (without PBC) and with Periodic Boundary Conditions (PBCs).

5.4.3 Representativ Volume Element (RVE)

As discussed in section 5.4, the RVE generally is the smallest volume fraction that represents the properties of the whole system. For periodic systems like auxetics, the RVE may consists of one or more unit cells. As demonstrated in Section 5.3.2, the auxetic structure studied in this work exhibits tetragonal symmetry in terms of anisotropy. The RVE we aim to identify must also exhibit this property. Furthermore, other mechanical properties, such as Poisson's ratio and Young's modulus, must align closely with those of the entire system.
As discussed in the last Section (5.4.2), in order to identify suitable RVE, the RVE candidates must be examined with the periodic boundary conditions (PBCs) and not under the conventional boundary conditions. This ensures that the results are not affected by the detrimental boundary effects. As potential candidates for the RVE, both a 1x1 (single) unit cell and 2x2 cells were considered. To ensure that the volume elements also satisfy the requirement for tetragonal symmetry, they were additionally evaluated in their

rotated states of 45° and 90°. All volume elements considered were subjected to uniaxial tensile tests, where a total displacement of 0.5 mm and 1 mm in the $\boldsymbol{e_2}$-direction is specified for the 1x1 and 2x2 cells, respectively, which corresponds to approximately 6% of global strain for both cases.
The simulation results for the transverse displacement fields (u_1) are presented in Figure 5.22. For the 1x1 unit cell, a clear difference in transverse displacement is observed between $\theta = 0°$ and $\theta = 90°$. At $\theta = 0°$, the results indicate that the sample tends to contract, exhibiting behavior opposite to typical auxetic properties. In contrast, at $\theta = 90°$, the unit cell demonstrates auxetic behavior by expanding in the transverse direction. However, in contrast to the 1x1 unit cell, 2x2 cells have the same transverse displacement field in the case of $\theta = 0°$ and $\theta = 90°$, exibithing auxetic behavior in both cases.

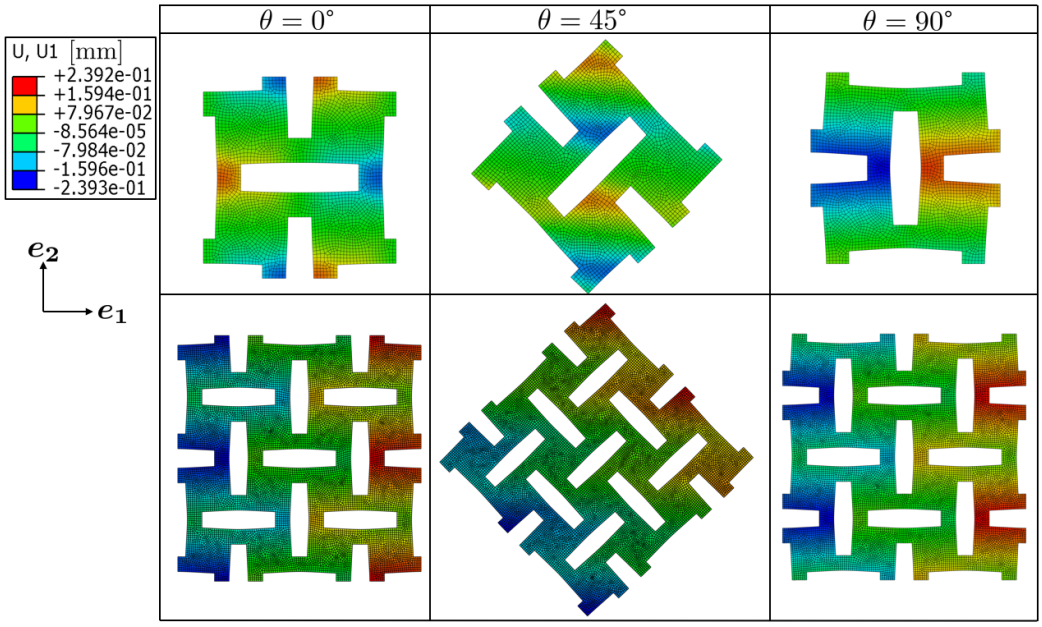

Figure 5.22: The transverse displacement fields (u_1) of the 1x1 unit cell and 2x2 cells subjected to uniaxial tensile loading in $\boldsymbol{e_2}$-direction after 6% global strain.

The next step involved analyzing the stress distributions in terms of von Mises equivalent stress in each volume elements, as shown in Figure 5.23. As expected from the results of the displacement field, the stress distributions for the 1x1 unit cell also differ between $\theta = 0°$ and $\theta = 90°$. At $\theta = 0°$, apart

from a few very small local stress concentrations, the unit cell exhibits nearly uniform stress everywhere. In this case, the local von Mises stresses exceed the yield strength of AlMg3 (approximately 119 MPa) almost everywhere, indicating that the entire unit cell undergoes plastic deformation. However, at $\theta = 90°$, this is not the case and the stress distribution looks exactly like that of every unit cell in the entire sheet, where the squares undergo pure rigid body rotation instead of plastic deformation. In contrast, the 2x2 cells exhibit the same stress distribution at $\theta = 0°$ and $\theta = 90°$, namely in both cases the stress distributions are the same as those in the whole sheet.

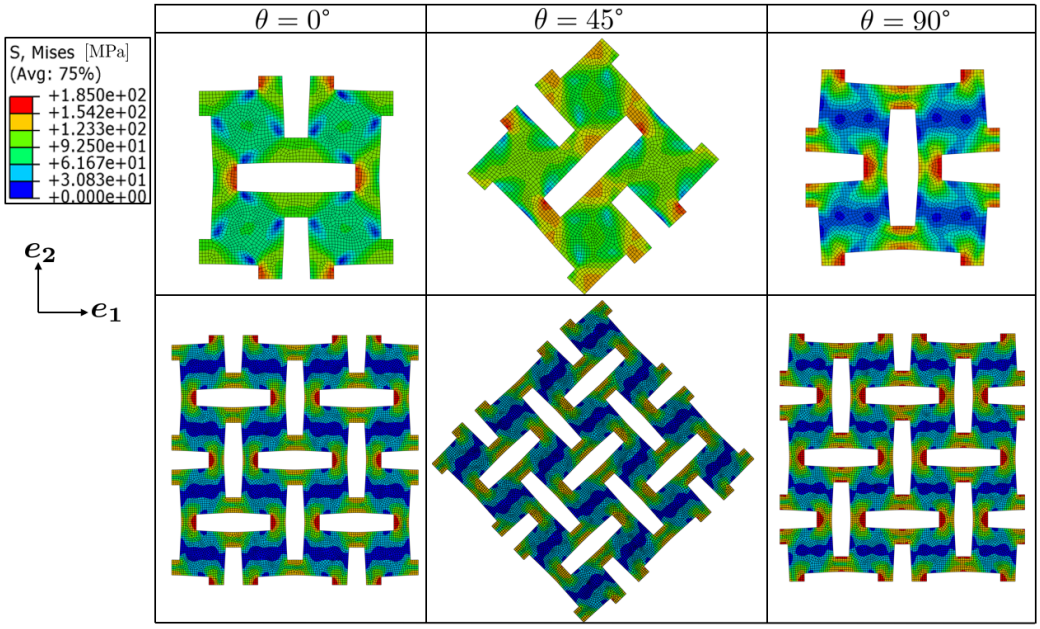

Figure 5.23: The stress distribution of the 1x1 unit cell and 2x2 cells subjected to uniaxial tensile loading in $\boldsymbol{e_2}$-direction after 6% global strain.

Finally, the effective stress-strain curves extracted from macroscopic boundary conditions for each volume element were analyzed and presented in Figure 5.24. As expected from the local field variables, the effective stress-strain curve for the 1x1 unit cell also differed between $\theta = 0°$ and $\theta = 90°$, failing to meet the requirement for tetragonal symmetry in the structure. In contrast, 2x2 cells demonstrated identical local and effective properties for both $\theta = 0°$ and $\theta = 90°$. Furthermore, the effective stress-strain curves for the 2x2 cells at $\theta = 0°$ and $\theta = 90°$ align closely with the curve of the fully resolved sheet, as can be seen in Figure 5.24.

All these reasons mentioned above indicate that the 2x2 cells are identified as a suitable RVE for the auxetic structure investigated.

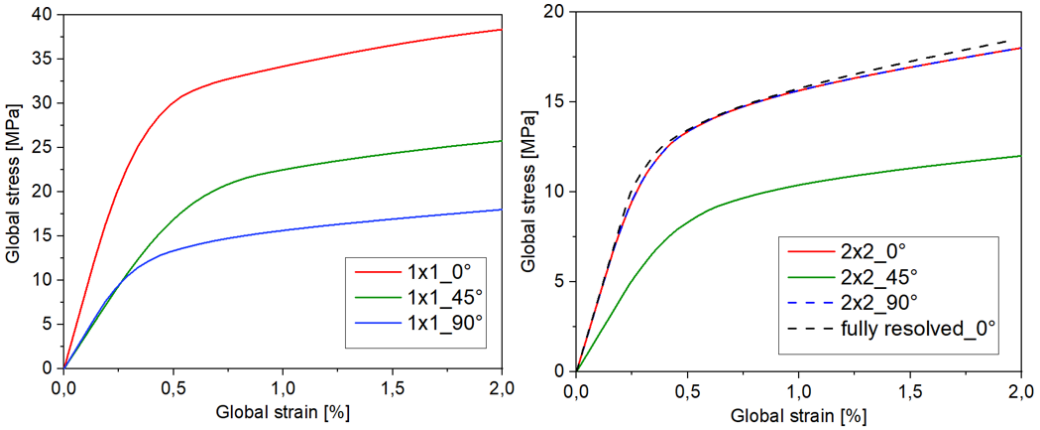

Figure 5.24: The effective stress-strain curves of the 1x1 unit cell and 2x2 cells subjected to uniaxial tensile loading until 2% global strain.

5.4.4 Effective Mechanical Properties

Following the identification of a representative volume element (RVE), the effective properties of the auxetic structure could be evaluated by homogenization of the micromechanical model defined within the RVE. For this purpose, Eq. 5.2 and 5.3 were applied in the corresponding two-dimensional context. In this setting, the boundaries are confined to the edges of the RVE, and consequently, the surface elements da of the integrals are reduced to the line elements dx.
To compute the effective strain $\bar{\boldsymbol{\varepsilon}}$, Eq. 5.2 is reformulated into Eq. 5.6, where the integral is replaced by a discrete summation over the nodal displacements located at the RVE boundaries.

$$\bar{\boldsymbol{\varepsilon}} = \sum_{j=1}^{4} [\frac{1}{N_j} \sum_{i=1}^{N_j} \boldsymbol{u}^{(i,j)} \otimes \boldsymbol{n}^{(j)}] \tag{5.6}$$

In this Equation (Eq. 5.6), the index i denotes the node number, j refers to the corresponding edge, and N_j represents the total number of nodes along that edge. Due to the imposed periodic boundary conditions (PBCs) and the associated symmetry between opposing edges, Eq. 5.6 reduces to Eq. 5.7, where the superscripts r and t refer to the right and top edges,

respectively, and N and M denote the total number of nodes located along the corresponding edges.

$$\bar{\boldsymbol{\varepsilon}} = 2\left(\frac{1}{N}\sum_{i=1}^{N}\boldsymbol{u}^{(i,r)} \otimes \boldsymbol{n}^{(r)} + \frac{1}{M}\sum_{i=1}^{M}\boldsymbol{u}^{(i,t)} \otimes \boldsymbol{n}^{(t)}\right) \tag{5.7}$$

Figure 5.25 shows the displacement fields u_1 and u_2 of the RVE with periodic boundary conditions (PBCs) under uniaxial tensile loading in the $\boldsymbol{e_2}$-direction, which are used to compute the effective strain $\bar{\boldsymbol{\varepsilon}}$.

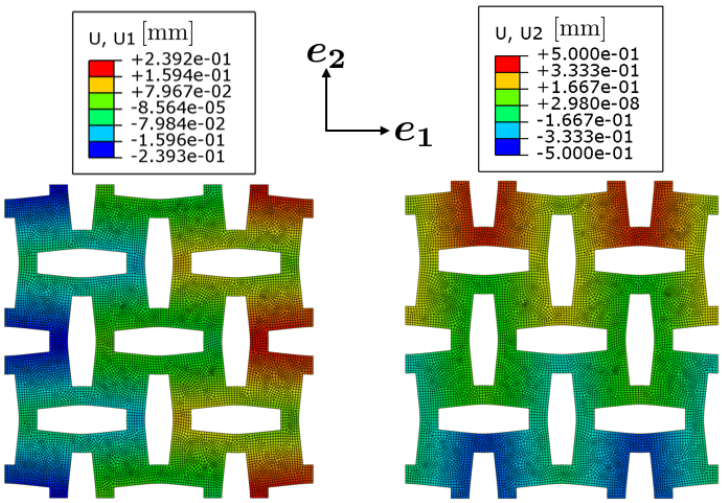

Figure 5.25: Resulting micro model of the RVE in terms of displacement fields with PBCs subjected to the uniaxial tensile load in $\boldsymbol{e_2}$-direction.

For the purpose of calculating the effective stress $\bar{\boldsymbol{\sigma}}$ from the local stresses illustrated in Fig. 5.26, the volume integral proved to be more suitable than the edge integral within the homogenization framework. This is because, in perforated microstructures such as the auxetic sheet, significant local variations occur within the interior of the material that are not captured at the boundaries. In other words, relying solely on the edge integral to compute the effective stress may result in loss of critical information. So, by applying Eq. 5.1

$$\bar{\boldsymbol{\sigma}} = \frac{1}{|V|}\int_V \boldsymbol{\sigma}(\mathbf{x})\,\mathrm{d}V \tag{5.8}$$

where V represents the volume (or area in 2D) of the RVE and $\boldsymbol{\sigma}(\mathbf{x})$ is the

microscopic stress at the point $\mathbf{x}$ within RVE. With the numerical implementation, Eq. 5.8 can be formulated as

$$\bar{\boldsymbol{\sigma}} \approx \frac{1}{|V|} \sum_{e=1}^{N} \int_{V_e} \boldsymbol{\sigma}(\mathbf{x}) \, \mathrm{d}V \tag{5.9}$$

Using numerical quadrature (e.g., Gauss integration), this becomes:

$$\bar{\boldsymbol{\sigma}} \approx \frac{1}{|V|} \sum_{e=1}^{N} \sum_{q=1}^{N_q} \boldsymbol{\sigma}^{(e,q)} \, w_q \, |J^{(e,q)}| \tag{5.10}$$

where

- $\bar{\boldsymbol{\sigma}}$ is the effective (homogenized) stress tensor,
- V is the total volume (or area in 2D) of the RVE,
- N is the total number of finite elements in the mesh,
- N_q is the number of integration points per element,
- $\boldsymbol{\sigma}^{(e,q)}$ is the stress tensor at integration point q in element e,
- w_q is the quadrature weight at point q,
- $|J^{(e,q)}|$ is the Jacobian determinant at point q in element e, representing the local volume (or area in 2D).

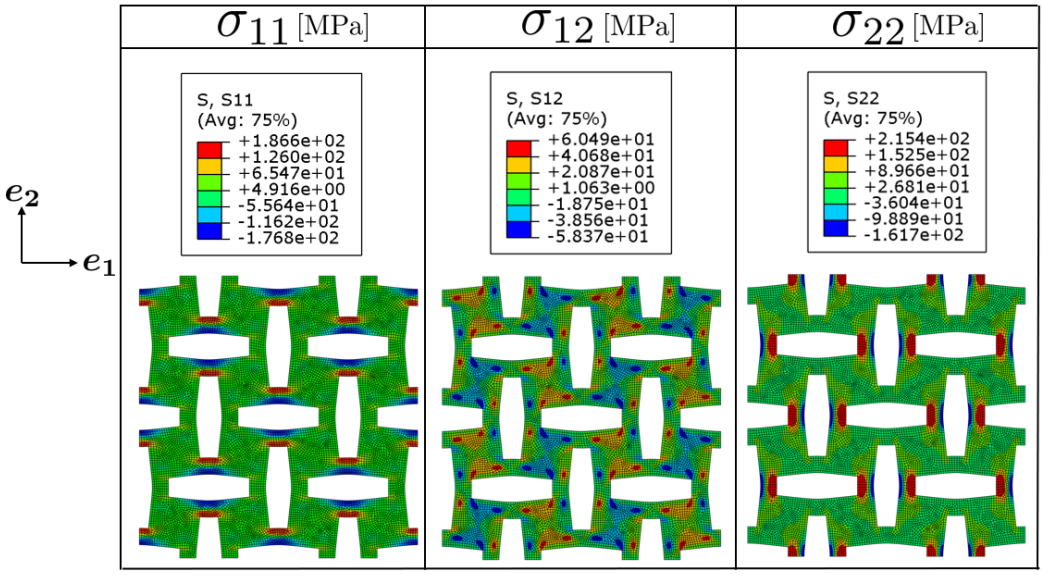

Figure 5.26: Resulting micro model of the RVE in terms of stress fields with PBCs subjected to the uniaxial tensile load in $\boldsymbol{e_2}$ direction.

The effective stress $\bar{\boldsymbol{\sigma}}$ and strain $\bar{\boldsymbol{\varepsilon}}$ were computed at each load increment, enabling the determination of the effective Young's modulus as the ratio $\frac{\bar{\sigma}_{22}}{\bar{\varepsilon}_{22}}$. Similarly, the effective Poisson's ratio was evaluated as $-\frac{\bar{\varepsilon}_{11}}{\bar{\varepsilon}_{22}}$. These calculations were carried out also for RVEs with orientation angles at $\theta = 5°, 10°, 15°, ..., 90°$.
The results were subsequently respresented as polar diagrams in terms of Young's modulus, Poisson's ratio and yield strength. Figure 5.27 presents the polar diagram of Young's modulus for the homogenized RVE. The maximum Young's modulus is approximately 3.2 GPa for samples oriented at 0° and repeated at 90° intervals, while the minimum is around 2.2 GPa for samples oriented at 45°, also repeated at 90° intervals. The polar diagram clearly exhibits five axes of symmetry: four within the plane at 45° intervals (indicated by the blue dashed lines) and one perpendicular to the plane. This configuration reflects the tetragonal symmetry of the material, as discussed in Section 5.3.2.

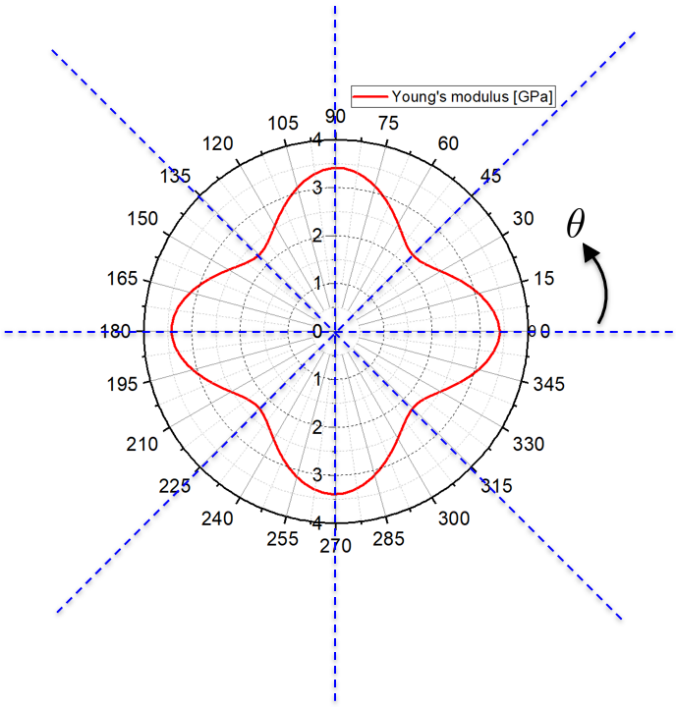

Figure 5.27: Polar diagram of effective Young's modulus for the homogenized RVE with the symmetry axes depicted in blue.

Finally, analogously to Young's modulus, the polar diagrams of Poisson's

ratio and yield strength were also plotted and presented in Figure 5.28.

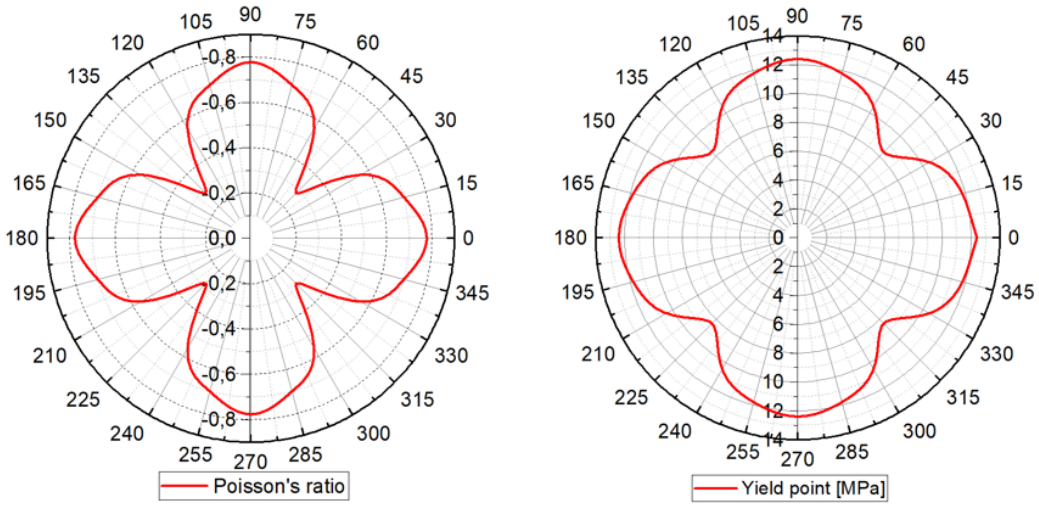

Figure 5.28: Polar diagrams of Poisson's ratio and yield strength for the homogenized RVE.

6

Material Model

6.1 Tetragonal Elastic Model

Using the procedure explained in Section 4.3.1, the corresponding elastic tensor for the auxetic structure studied in this work with tetragonal symmetry can now be determined. It should be noted that in tetragonal materials the orthotropic properties are already included, since $\theta = 0°$ and $\theta = 90°$ also build symmetry planes in these structures. In other words, tetragonal symmetry can be interpreted as a special case of orthotropy. The difference is that in tetragonal materials there exists an additional symmetry plane at $\theta = 45°$, which leads to further restrictions in the elastic tensor compared to orthotropic materials. This means that we assume the orthotropic elastic tensor as the initial situation and now we consider the transformation (4.28) using the orthogonal tensor $\mathbf{R}$ in (4.33) with respect to $\theta = 45°$, thus:

$$\mathbf{R}(\pi/4) \hat{=} \begin{bmatrix} 0 & -1 & 0 \\ -1 & 0 & 0 \\ 0 & 0 & 1 \end{bmatrix} \tag{6.1}$$

The transformation (4.28) can be written in index notation as follows:

$$C_{ijkl} = R_{ip}R_{jq}R_{kr}R_{lt}C_{pqrt} \tag{6.2}$$

The zeros in tensor (6.1) do not contribute to the corresponding summation using the transformation (6.2). Therefore, only the components C_{12}, C_{21} and C_{33} have to be taken into account. Due to the symmetry properties of the elasticity tensor $\overset{4}{\mathbf{C}}$ and also the orthogonal tensor $\mathbf{R}$, the number of components to be considered is reduced to two, that is, only C_{12} and C_{33}, which correspond to -1 or $+1$, respectively. Now we consider all possible cases in the transformation (6.2) in which these two components can appear:

$$C_{1111} = R_{12}R_{12}R_{12}R_{12}C_{2222} \longrightarrow C_{1111} = C_{2222} \xrightarrow{\text{Voigt}} C_{11} = C_{22} \tag{6.3}$$

$$C_{1113} = R_{12}R_{12}R_{12}R_{33}C_{2223} \longrightarrow C_{1113} = -C_{2223} \xrightarrow{\text{Voigt}} C_{15} = -C_{25} \tag{6.4}$$

$$C_{1133} = R_{12}R_{12}R_{33}R_{33}C_{2233} \longrightarrow C_{1133} = C_{2233} \xrightarrow{\text{Voigt}} C_{13} = C_{23} \tag{6.5}$$

$$C_{1333} = R_{12}R_{33}R_{33}R_{33}C_{2333} \longrightarrow C_{1333} = -C_{2333} \xrightarrow{\text{Voigt}} C_{53} = -C_{43} \tag{6.6}$$

$$C_{1313} = R_{12}R_{33}R_{12}R_{33}C_{2323} \longrightarrow C_{1313} = C_{2323} \xrightarrow{\text{Voigt}} C_{44} = C_{55} \tag{6.7}$$

The transformation results according to (6.4) and (6.6) do not give any new information since these components are already zero in the orthotropic tensor shown in section (4.3.1) and therefore they can be treated as trivial equations. However, the remaining relations (6.3), (6.5) and (6.7) further restrict the orthotropic tensor, requiring the corresponding components to be pairwise identical, as indicated by the color-coded compliance tensor below. Finally, the tetragonal compliance tensor $\overset{4}{\mathbf{S}}$ based on the results of (6.3), (6.5) and (6.7) looks like this:

$$\mathbf{S}_{\text{ort}} \hat{=} \begin{bmatrix} \frac{1}{E_1} & \frac{-\nu_{21}}{E_2} & \frac{-\nu_{31}}{E_3} & 0 & 0 & 0 \\ \frac{-\nu_{21}}{E_2} & \frac{1}{E_2} & \frac{-\nu_{32}}{E_3} & 0 & 0 & 0 \\ \frac{-\nu_{31}}{E_3} & \frac{-\nu_{32}}{E_3} & \frac{1}{E_3} & 0 & 0 & 0 \\ 0 & 0 & 0 & \frac{1}{G_{13}} & 0 & 0 \\ 0 & 0 & 0 & 0 & \frac{1}{G_{23}} & 0 \\ 0 & 0 & 0 & 0 & 0 & \frac{1}{G_{12}} \end{bmatrix} \quad \mathbf{S}_{\text{tet}} \hat{=} \begin{bmatrix} \frac{1}{E_1} & \frac{-\nu_{21}}{E_1} & \frac{-\nu_{31}}{E_3} & 0 & 0 & 0 \\ \frac{-\nu_{21}}{E_1} & \frac{1}{E_1} & \frac{-\nu_{31}}{E_3} & 0 & 0 & 0 \\ \frac{-\nu_{31}}{E_3} & \frac{-\nu_{31}}{E_3} & \frac{1}{E_3} & 0 & 0 & 0 \\ 0 & 0 & 0 & \frac{1}{G_{13}} & 0 & 0 \\ 0 & 0 & 0 & 0 & \frac{1}{G_{13}} & 0 \\ 0 & 0 & 0 & 0 & 0 & \frac{1}{G_{12}} \end{bmatrix}$$

Based on the results, the number of independent elastic constants that

appear in the compliance tensor $\overset{4}{\mathbf{S}}$ is reduced from 9 (orthotropic) to 6 (tetragonal).
In the plane stress state, the number of independent engineering constants is reduced to 3 in the case of tetragonal symmetry, namely the Young modulus E_1, the Poisson's ratio ν_{21} and the shear modulus G_{12}. The corresponding compliance tensor is expressed as:

$$\mathbf{S}_{\text{tet}} \hat{=} \begin{bmatrix} \frac{1}{E_1} & \frac{-\nu_{21}}{E_1} & 0 \\ \frac{-\nu_{21}}{E_1} & \frac{1}{E_1} & 0 \\ 0 & 0 & \frac{1}{G_{12}} \end{bmatrix}$$

6.1.1 Elastic Parameters

To model the elastic behavior of auxetic sheet metal, three parameters are required, namely E_1 (Young's modulus), G_{12} (shear modulus) and ν_{21} (Poisson's ratio). These parameters were determined through numerical simulations conducted on a homogenized representative volume element (RVE), including a uniaxial tensile test to obtain Young's modulus and Poisson's ratio, and a simple shear test to evaluate the shear modulus.
The values of Young's modulus and Poisson's ratio were obtained directly from the polar diagrams of the RVE (5.27) and (5.28). To determine the shear modulus, an independent shear test was carried out, with the resulting curves presented in Fig. 6.3. The shear modulus was then determined as the slope of the linear region of the global shear stress-slip curve, expressed as:

$$G_{12} = \frac{\tau_{12}}{\gamma_{12}} = 1.9\,\text{GPa} \tag{6.8}$$

Finally, the three essential parameters required for modeling the elastic behavior of the auxetic sheet are summarized in Table 6.1.

E_1	ν_{21}	G_{12}
3.3 GPa	-0.78	1.9 GPa

Table 6.1: The elastic parameters of the reference auxetic sheet with AR=5.

6.2 Pressure Sensitive Plastic Model

As mentioned in Section 4.3.2, the plastic behavior of the auxetic sheet, influenced by the perforations, can be characterized using a pressure-dependent yield criterion. Given the sheet's thin thickness of 1 mm, a plane stress condition can be assumed for simplification. In the first step, an isotropic Drucker-Prager yield criterion was formulated in the primary direction ($\theta = 0°$). Subsequently, the model was extended to anisotropy, taking into account the existing tetragonal symmetry.

6.2.1 Initial Yield Surface

In order to calibrate the yield surface, various tests must be carried out. Analogously to the elastic part, numerical simulations on homogenized RVE were also used to identify the resulting yield surface. All effective stress-strain curves have already been determined by the homogenization procedure using Eq. 5.7 and Eq. 5.10 explained in Section 5.4.4. To ensure that all results are consistent, $R_{P0.1}$ was taken as the yield point for all tests.
Due to the plane stress condition, the tests were restricted to 2D tests, specifically uniaxial tensile test, simple shear test, combined shear-tension and biaxial tensile tests. Biaxial tensile tests were conducted using both uniform (balanced biaxial test) and non-uniform loading along two axes. Since the superimposed tensile-shear test was difficult to perform experimentally and because of the consistency of the results, all tests were treated numerically here. All simulation parameters are the same as those used in section 5.3. As mentioned previously, this section focuses solely on the homogenized RVE oriented at 0° (reference direction) to identify an isotropic yield surface. The next step involves extending the identified yield function to account for anisotropy.

Uniaxial Tensile Test

Numerical uniaxial tensile test was performed on the RVE. The resulting local stress components are already presented in Fig. 5.26. The corresponding effective stress tensor was obtained by homogenizing the local stresses using Eq. 5.10. This calculation revealed that the effective values of $\bar{\sigma}_{11}$ and $\bar{\sigma}_{12}$ are negligible compared to $\bar{\sigma}_{22}$, as they are nearly zero. This observation

can also be qualitatively inferred from the local stress distributions shown in the Fig. 5.26, where symmetry in the contour patterns and the relative magnitudes of the values of σ_{11} and σ_{12} indicate a mutual cancellation. The effective Strain $\bar{\varepsilon}$ was also obtained by homogenization the local strains according to Eq. 5.7. By calculating the effective stress and strain in each time step, the effective stress-strain curve could then be determined. The yield stress was identified from the effective $\bar{\sigma}_{22} - \bar{\varepsilon}_{22}$ curve as the only stress component with a non-zero value using the $Rp_{0.1}$ line (dashed blue line) as shown in Fig. 6.1.

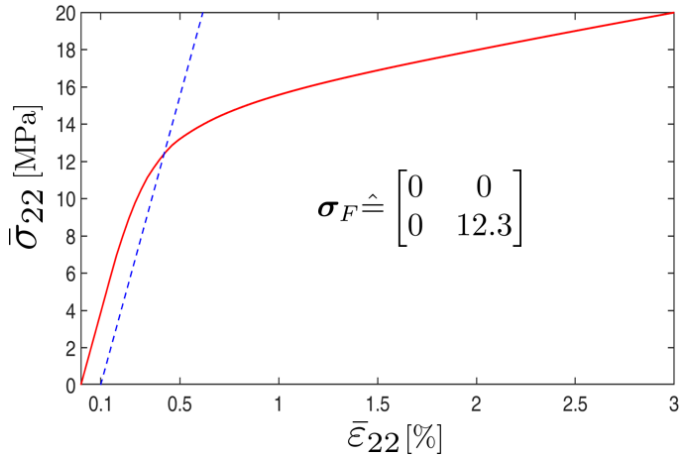

Figure 6.1: Effective $\bar{\sigma}_{22} - \bar{\varepsilon}_{22}$ curve obtained from a uniaxial tensile test, based on the homogenization of local stresses within the RVE, including the $R_{p0.1}$ offset line for yield point identification.

Shear Test

Numerical simple shear test was also performed on the RVE by applying a tangential force to the upper and lower edges of the RVE. Here, effective stresses and strains were also determined by homogenizing the local values according to Eq. 5.10 and Eq. 5.7. The resulting local stress fields are shown in Fig. 6.2. The local shear stress σ_{12} induced by the applied shear load within the RVE is significantly more pronounced than the local normal stresses σ_{11} and σ_{22}. This is also visually evident, as the effective stresses $\bar{\sigma}_{11}$ and $\bar{\sigma}_{22}$ are nearly zero, a result of the perfect symmetry observed in their corresponding local distributions.

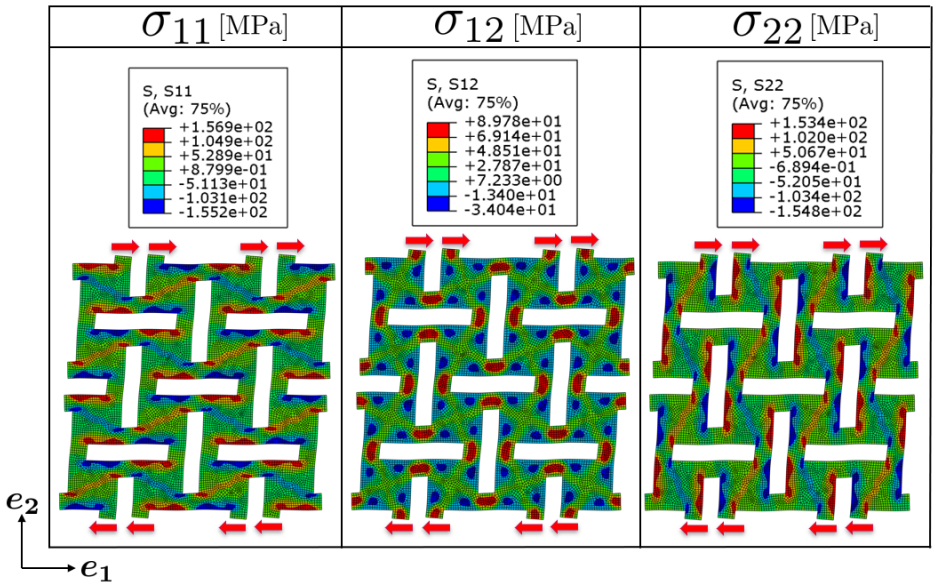

Figure 6.2: Microstructural stress response of the RVE subjected to simple shear load in the $\boldsymbol{e_1}$ direction, using PBCs.

Finally, the corresponding shear yield stress was identified from the $\bar{\sigma}_{12} - \bar{\gamma}_{12}$ curve as the only stress component with a non-zero value using the $Rp_{0.1}$ line as shown in Fig. 6.3.

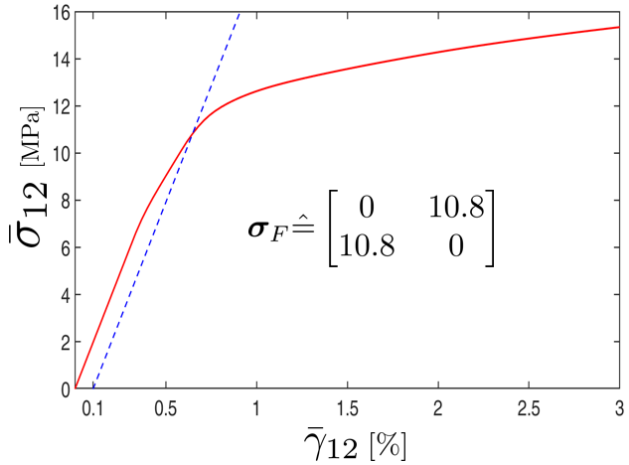

Figure 6.3: Effective $\bar{\sigma}_{12} - \bar{\gamma}_{12}$ curve obtained from a simple shear test, based on the homogenization of local stresses within the RVE, including the $R_{p0.1}$ offset line for yield point identification.

Combined Tensile-Shear Loading

To identify multiple points on the yield surface, an additional superimposed tension-shear loading was applied.
To generate the superimposed tension–shear stress state in the RVE, the applied force can be oriented at any angle of inclination relative to the $\boldsymbol{e}_1$-axis on the upper edge. As an example in this work, the applied force was oriented at an angle of 20° from the $\boldsymbol{e}_1$ axis to induce a combined tension–shear loading condition, as shown in Fig. 6.4.
The effective stress and strain were obtained by homogenizing the local field values, with $\bar{\sigma}_{11}$ being the only stress component that remained nearly zero.

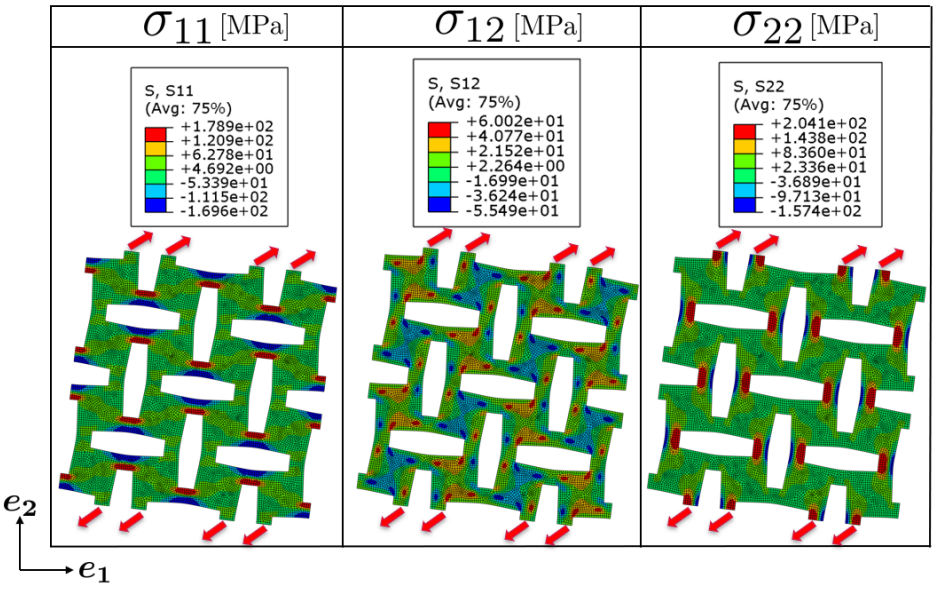

Figure 6.4: Microstructural stress response of the RVE subjected to combined tensile-shear load, using PBCs.

First, $\bar{\sigma}_{22}$ was plotted against $\bar{\varepsilon}_{22}$, as it is the dominant stress component compared to $\bar{\sigma}_{12}$. The yield stress was then determined using the $Rp_{0.1}$ offset method. This allowed for the identification of the corresponding time step at which yielding begins.

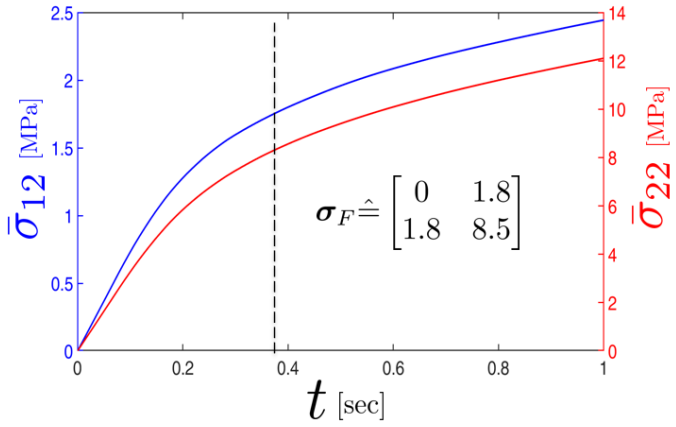

Figure 6.5: Effective normal ($\bar{\sigma}_{22}$, red) and shear ($\bar{\sigma}_{12}$, blue) stress curves versus time, obtained from combined tensile–shear loading based on the homogenization of local stresses within the RVE. The dashed offset line indicates the yield points.

Subsequently, both $\bar{\sigma}_{22}$ and $\bar{\sigma}_{12}$ were plotted as functions of time, enabling the determination of the $\bar{\sigma}_{12}$ value at the onset of yielding, as illustrated in Fig. 6.5.

Biaxial Tensile Tests

In the next step, biaxial tensile tests were performed by applying normal forces (tensions) to the RVE along the $\boldsymbol{e}_1$- and $\boldsymbol{e}_2$-axes, both uniformly and at varying rates. An equibiaxial tensile test, where both axes are stretched equally, along with two additional biaxial tensile tests with strain rate ratios $\frac{\dot{\varepsilon}_{11}}{\dot{\varepsilon}_{22}}$ of 0.9 and 0.8, were conducted.
The local stress fields resulting from the balanced biaxial tensile test are shown in Fig. 6.6. It can be observed that the local shear stresses σ_{12} effectively cancel out due to the inherent symmetry of the setup, resulting in an almost zero effective shear stress $\bar{\sigma}_{12}$.

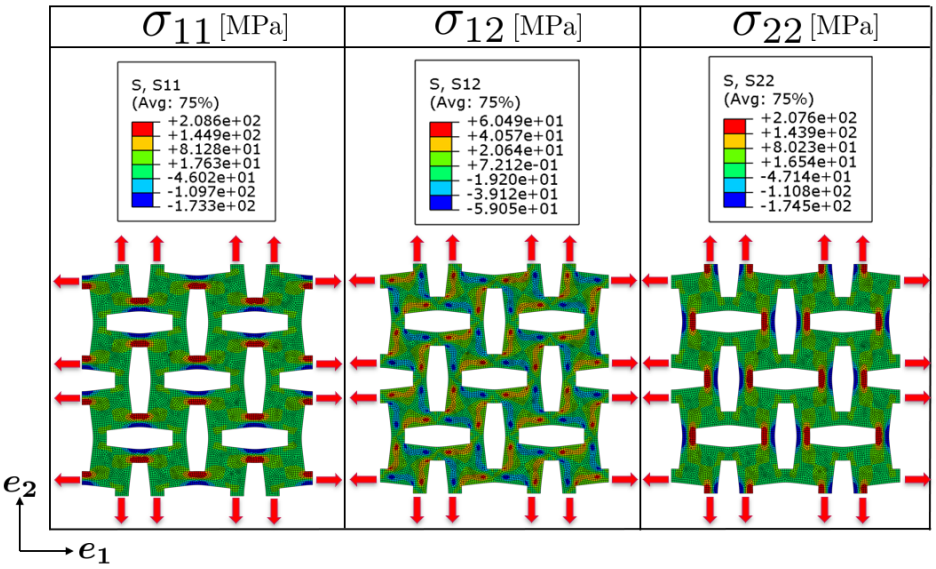

Figure 6.6: Microstructural stress response of the RVE subjected to balanced biaxial tensile load, using PBCs.

In contrast, this symmetry does not apply to the normal stresses σ_{11} and σ_{22}, where a noticeable difference in the peak values of the corresponding local stress fields is evident. The homogenized effective stresses $\bar{\sigma}_{11}$ and $\bar{\sigma}_{22}$ and strains $\bar{\varepsilon}_{11}$ and $\bar{\varepsilon}_{22}$ were calculated from the micromodel and the corresponding effective stress-strain curves are shown in Fig. 6.7.

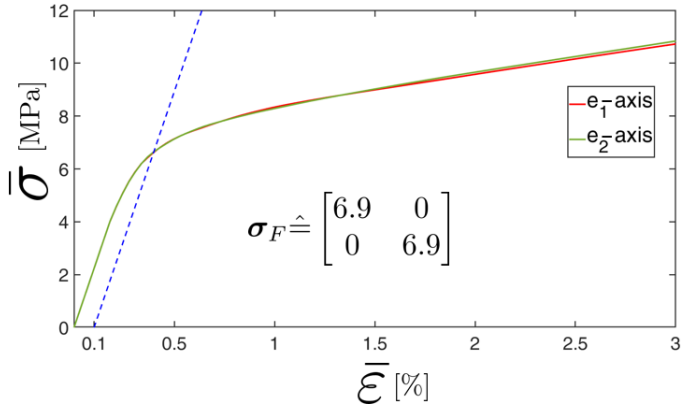

Figure 6.7: Effective $\bar{\sigma} - \bar{\varepsilon}$ curves with respect to the both axes obtained from a biaxial tensile test, based on the homogenization of local stresses within the RVE, including the $R_{p0.1}$ offset line for yield point identification.

As shown in Fig. 6.7, both curves exhibit identical trends, confirming the accuracy of the simulation and homogenization procedures. The corresponding yield stress was subsequently determined using the $R_{p0.1}$ offset method.
To identify multiple points on the yield surface, two additional biaxial tensile tests were conducted on the RVE, this time using different strain rates along the two principal axes—specifically, strain rate ratios of 0.9 and 0.8. As in the balanced biaxial test, the effective stresses and strains were obtained by homogenizing the local field values. In both cases, the effective shear stress remained nearly zero due to the symmetry of the loading conditions.

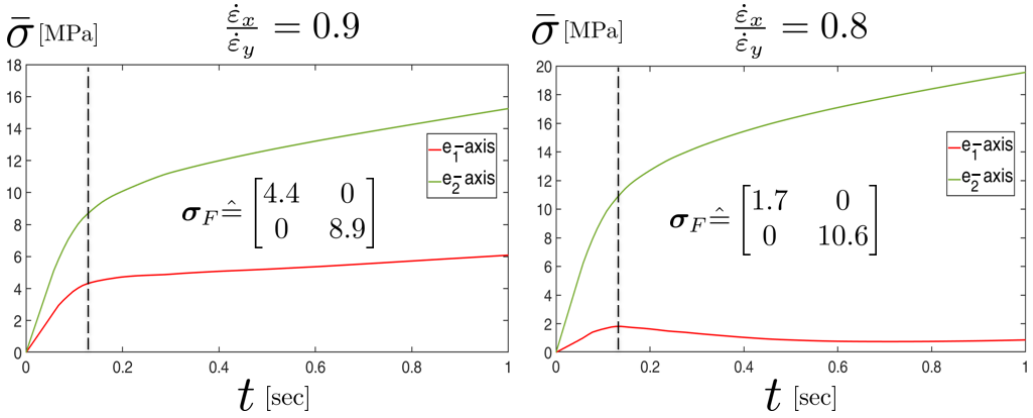

Figure 6.8: Effective normal stress curves versus time, obtained from inhomogeneous biaxial tensile loading with two different strain rate ratios based on the homogenization of local stresses within the RVE. The dashed offset line indicates the yield points.

Because of the differing strain rates, the effective stress–strain responses along the two axes had to be evaluated independently. The onset of yielding was first determined from the curve corresponding to the dominant stress component. This allowed identification of the time step at which yielding began. Finally, by plotting both stress components as functions of time, the corresponding yield onset point for the second axis could also be identified, as shown in Fig. 6.8.

$p - q$ plane

In the context of continuum mechanics and material modeling, the $p - q$ plane is commonly used to represent yield criteria for pressure-sensitive materials such as soils, rocks and porous metals. It provides a convenient two-dimensional space for visualizing yield surfaces, especially when analyzing complex multiaxial stress states. Yield functions expressed in this plane, such as the Drucker–Prager model, describe the material's transition from elastic to plastic behavior based on the combined effects of hydrostatic pressure and shear stress.
After analyzing the tests described in the previous section, six different yield states were identified. Based on these yield stresses, the corresponding p and q values were calculated, which are derived from the first invariant I_1 of the Cauchy stress tensor and the second invariant J_2 of the deviatoric stress tensor as follows:

$$p = -\frac{1}{2}I_1 = -\sigma_m = -\frac{(\sigma_{11} + \sigma_{22})}{2} \tag{6.9}$$

$$q = \sqrt{3J_2} = \sqrt{\sigma_{11}^2 - \sigma_{11}\sigma_{22} + \sigma_{22}^2 + 3\sigma_{12}^2} \tag{6.10}$$

All calculated p and q values from the various experiments are presented in Table 6.2.

Test	$\boldsymbol{\sigma_F}$	$\boldsymbol{p}$	$\boldsymbol{q}$
uni-tensile	$\begin{bmatrix} 0 & 0 \\ 0 & 12.3 \end{bmatrix}$	-6.15 MPa	12.3 MPa
shear	$\begin{bmatrix} 0 & 10.8 \\ 10.8 & 0 \end{bmatrix}$	0 MPa	18.7 MPa
tensile-shear	$\begin{bmatrix} 0 & 1.8 \\ 1.8 & 8.5 \end{bmatrix}$	-4.25 MPa	9.6 MPa
biax_1	$\begin{bmatrix} 6.9 & 0 \\ 0 & 6.9 \end{bmatrix}$	-6.9 MPa	6.9 MPa
biax_0.9	$\begin{bmatrix} 4.4 & 0 \\ 0 & 8.9 \end{bmatrix}$	-6.65 MPa	7.7 MPa
biax_0.8	$\begin{bmatrix} 1.7 & 0 \\ 0 & 10.6 \end{bmatrix}$	-6.15 MPa	9.86 MPa

Table 6.2: The varying p and q values obtained from different test types for yield surface calibration in the p–q plane.

After determining the values of p and q, they were plotted against each other to approximate the optimal yield function. As shown in Fig. 6.9, the plotted points exhibit the best linear relationship. The trend was then fitted linearly using MATLAB's fit function.

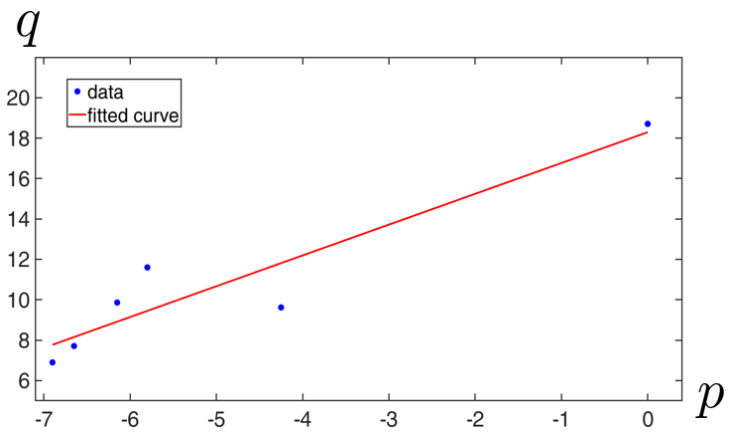

Figure 6.9: Plotting the p and q values along with the corresponding linear fit curve.

By reformulating the Drucker-Prager yield function (4.56) in terms of p and q, the parameter a was identified as follows:

$$q - ap - b(\sigma_F) = 0 \qquad a = 1.53 \text{ [-]} \tag{6.11}$$

6.2.2 Hardening

In this study, we assume isotropic hardening, where the yield surface expands uniformly with increasing load. Since the auxetic sheets cannot be in a compressive state in reality (as buckling would occur), no conclusions could be drawn regarding the existence of kinematic hardening. To model the hardening behavior of auxetic sheets, the true stress-true plastic strain curve (also known as the flow curve) was derived from the effective engineering stress-strain curve using Eq. 3.5 and 3.6. As shown in Fig. 6.10, the flow curve exhibits a relatively good linear trend, which was interpolated using MATLAB's fit function.

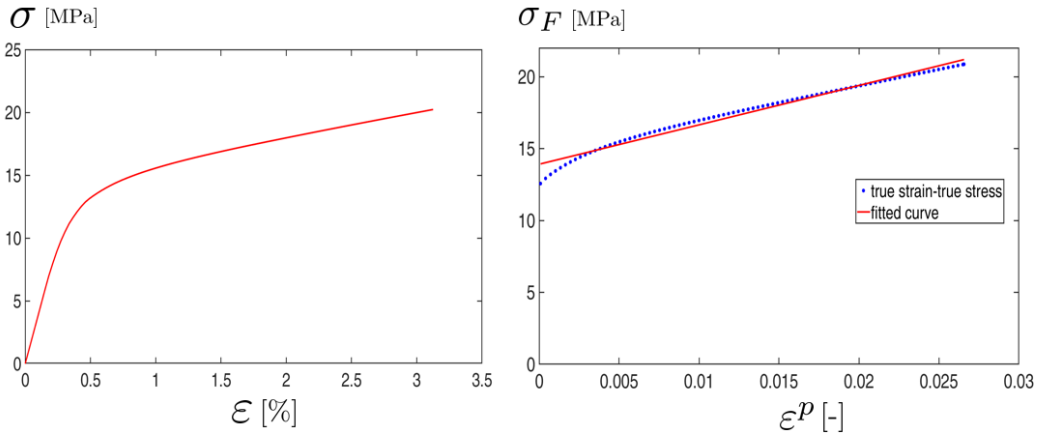

Figure 6.10: Engineering stress-strain curve (left) and true stress-plastic strain curve or so-called flow curve (right).

After interpolation of the hardening behavior, the linear hardening modulus k could be identified as follows:

$$\sigma_F = \sigma_0 + k\varepsilon^p \qquad k = 274\,[\text{MPa}] \tag{6.12}$$

By inserting the yield stress σ_F, obtained from the uniaxial tensile test, into the yield function (Eq. 6.11), the parameter b was determined as a function of the yield stress σ_F as follows:

$$b = \sigma_F + \frac{a}{2}\sigma_F \tag{6.13}$$

Finally, by substituting Eq. 6.13 into Eq. 6.11, the final form of the flow function f, incorporating hardening, is obtained as follows:

$$f = q - ap - (\sigma_F + \frac{a}{2}\sigma_F) = q - ap - \sigma_F(1 + \frac{a}{2}) = 0 \tag{6.14}$$

A qualitative illustration of the yield criterion 6.14, incorporating linear isotropic hardening, is presented in Fig. 6.11. As the accumulated equivalent plastic strain ε^p increases, the $p - q$ curve shifts upward without any change in slope, which consequently results in a corresponding shift of the intercept on the p-axis.

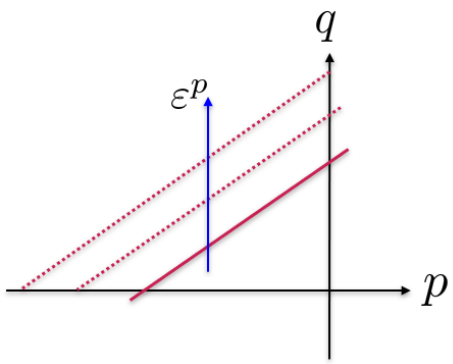

Figure 6.11: Qualitative representation of the evolution of the $p - q$ curve with increasing equivalent accumulated plastic strain ε^p.

6.3 Extension to Anisotropic Plasticity

The previously developed plasticity model is based on isotropy assumptions. However, the material under investigation exhibits anisotropic behavior with tetragonal symmetry, as demonstrated in Section 5.3.2. It has been observed that the tensor transformation relationships with respect to rotation adequately capture the existing anisotropy. This suggests that the given tetragonal symmetry leads to a form of functional anisotropy, rather than a fixed directional dependence. Consequently, an extension of the existing model is necessary to explicitly account for the anisotropic properties of the material. In the following, homogenized RVE with orientation angles of $\theta = 0°$, $15°$, $30°$ and $45°$ were subjected to a uniaxial tensile test in the $e_{gl.}$-direction, as shown in Fig. 6.12.

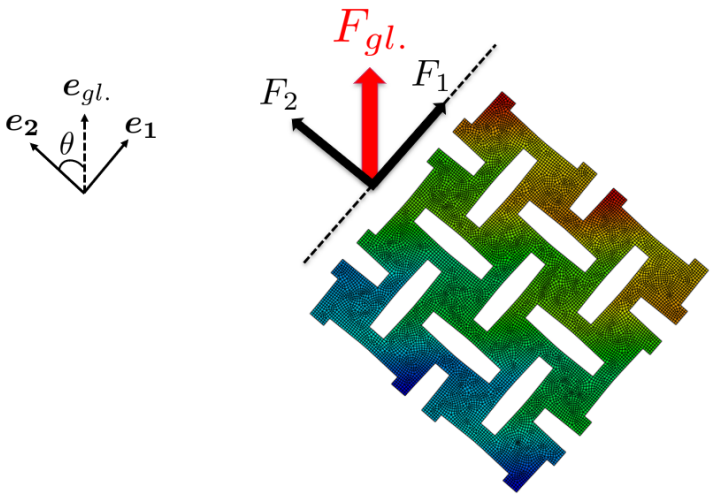

Figure 6.12: Schematic depiction of the global ($\boldsymbol{e}_{gl.}$) and local cartesian ($\boldsymbol{e_1} - \boldsymbol{e_2}$) directions.

The corresponding force-displacement curves are presented in Fig. 6.13. The resulting curves were observed to gradually decrease as the orientation angle θ increases. Moreover, the trend becomes more pronounced at higher angles, as reflected in the greater difference between the curves at $\theta = 30°$ and $\theta = 45°$ compared to those at $\theta = 0°$ and $\theta = 15°$.

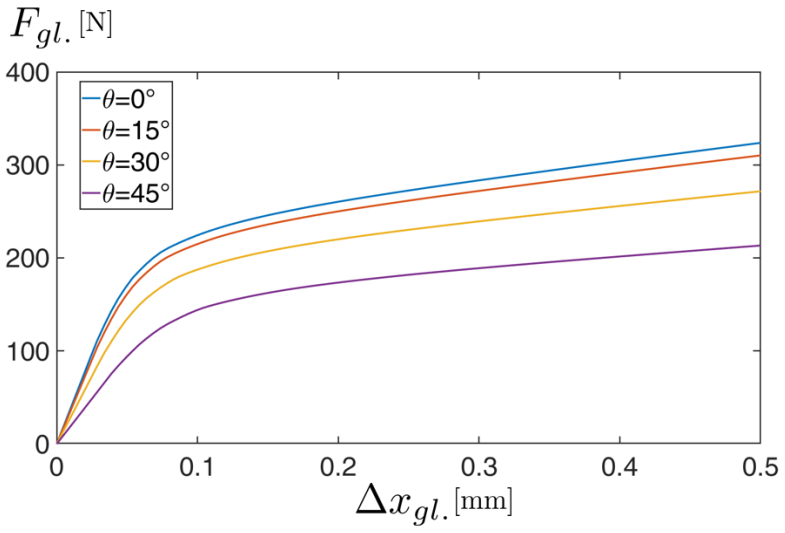

Figure 6.13: Global force-displacement curves for the RVEs with various θ subjected to uniaxial tensile tests.

To have a more precise interpretation, the resulting global forces $F_{gl.}$ were projected into normal and shear components F_2 and F_1 within the local coordinate system using these equations:

$$F_1 = F_{gl.} \sin(\theta) \tag{6.15}$$
$$F_2 = F_{gl.} \cos(\theta) \tag{6.16}$$

and then converted into corresponding normal and shear stresses σ_{22} and τ_{12} by dividing them by the reference area. In the next step, normal and shear stresses were plotted against time and then the corresponding yield stress tensor was determined, as shown in Fig. 6.14 for samples with θ =15° and θ =30° respectively. It should be emphasized that plotting the stresses against time is not related to any rate dependency. This approach was used solely for visualization purposes, as the σ_{22} and σ_{12} values correspond to different strain levels and could therefore not be plotted directly against a common strain axis.

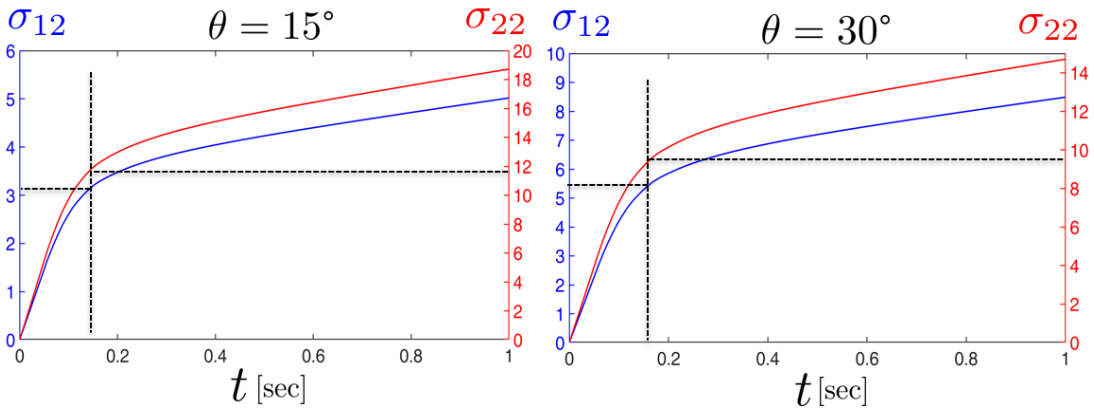

Figure 6.14: Normal and shear stress curves vs time for the RVEs with θ=15° and 30° with dashed lines indicating the onset of yielding ($R_{p0.1}$).

All yield stress tensors for the samples with θ=15°, 30° and 45° determined by this method are listed in Tab. 6.3.

Sample	$\boldsymbol{\sigma_F}$
$\theta = 15°$	$\begin{bmatrix} 0 & 3.10 \\ 3.10 & 11.66 \end{bmatrix}$
$\theta = 30°$	$\begin{bmatrix} 0 & 5.40 \\ 5.40 & 9.35 \end{bmatrix}$
$\theta = 45°$	$\begin{bmatrix} 0 & 6.30 \\ 6.30 & 6.30 \end{bmatrix}$

Table 6.3: Yield stress tensors for the RVEs with various θ within the local coordinate system.

Subsequently, the values in Table 6.3 were compared with the yield stress tensors obtained through the transformation of the yield stress with respect to the global coordinate system. That means we consider the yield stress of the RVE at $\theta = 0°$ i.e. $\boldsymbol{\sigma}_F = \begin{bmatrix} 0 & 0 \\ 0 & 12.3 \end{bmatrix}$ MPa and transform it into the corresponding local coordinate system using the rotation transformation tensor $\mathbf{R}(\theta)_{rot}$ in Eqs. 4.34 and 4.27.
It was observed that the yield stresses from Table 6.3 were quite identical with corresponding yield stresses obtained from the transformation of the yield stress tensor of the RVE at reference direction i.e. $\theta = 0°$. These findings suggest that the developed isotropic plasticity model is also applicable to the local coordinate system through established transformation relationships.
Now, let us return to the yield function developed (Eq. 6.11) for the isotropic case. For this equation to be valid in the local coordinate system, the individual terms must be transformed accordingly. The terms p and q are functions of stress invariants, which means that they are inherently independent of the coordinate system. As a result, they remain unchanged under any rotation transformation. However, the term $b(\sigma_F)$, or more precisely, the yield stress σ_F, is the only component of the yield function f that undergoes transformation based on the given pattern orientation angle θ. It leads to:

$$f = q - ap - b'(\sigma_F) = 0 \tag{6.17}$$

applying Eq. 6.13:

$$b'(\sigma_F) = (\sigma_F(1 + \frac{a}{2}))' = \sigma'_F(1 + \frac{a}{2}) \tag{6.18}$$

In this equation, σ_F represents the yield stress obtained from the uniaxial tensile test and, based on Fig. 6.12, is defined as

$$\sigma_F = \frac{F_{(gl.)}}{A} \tag{6.19}$$

where $F_{gl.}$ is the yield force and A is the reference area. When the sample (pattern) rotates by $\theta°$, the corresponding yield stress transforms accordingly. The new yield stress is given by

$$\sigma'_F = \frac{F_2}{A} = \frac{F_{gl}\cos(\theta)}{A} = \sigma_F \cos(\theta) \tag{6.20}$$

Applying the linear hardening relationship Eq. 6.12 in Eq. 6.20 leads to

$$\sigma'_F = \sigma_0 \cos(\theta) + k \cos(\theta)\, \varepsilon^p \tag{6.21}$$

The relationship 6.21 could be also confirmed by the corresponding hardening behavior. Fig. 6.15 shows the hardening curves for the RVE with $\theta = 0°$, 15°, 30° and 45°. All curves were effectively approximated using linear interpolation in MATLAB, each characterized by the linear hardening modulus k.

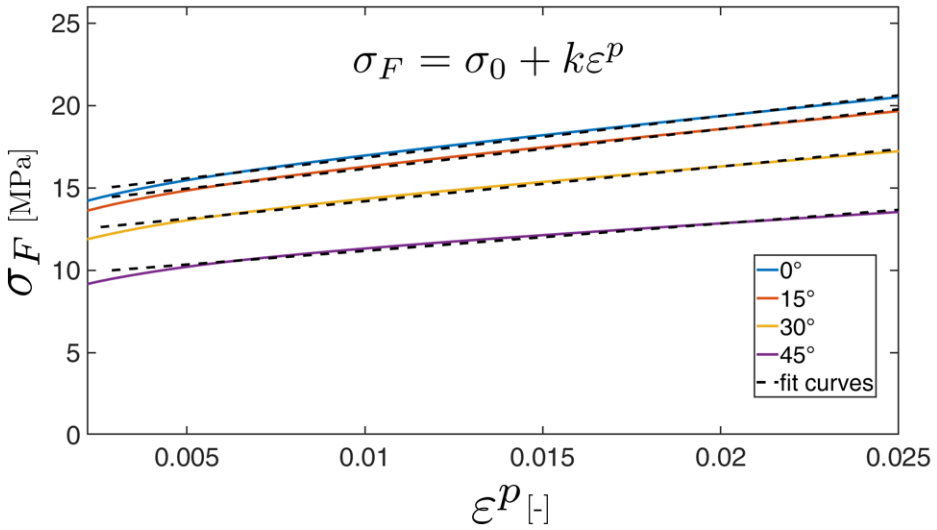

Figure 6.15: True stress-true strain curves (hardening curves) for the RVE with different θ, along with the corresponding linear fits for each curve.

Tab. 6.4 presents both the values k directly obtained from the curves and those calculated using the relationship $k' = k_0 \cos(\theta)$. A comparison of these results demonstrates the validity of the relationship 6.21, as the differences between the k values from the curves and the corresponding $k\cos(\theta)$ values were less than 2%. The same results were also observed for the first term of Eq. 6.21, i.e. $\sigma'_0 = \sigma_0 \cos(\theta)$.

Sample	k	$k_0 \cos(\theta)$
$\theta = 0°$	274	274
$\theta = 15°$	260	264
$\theta = 30°$	232	237
$\theta = 45°$	188	193

Table 6.4: Comparison of the linear hardening modulus k obtained from the hardening curves with their corresponding values from the relationship $k' = kcos(\theta)$, where k_0 denotes the k-value of $\theta = 0°$

These results lead to the extension of the isotropic yield function (Eq. 6.14) to the corresponding functional anisotropic yield function as follows

$$f = q - ap - \sigma_F \cos(\theta)(1 + \frac{a}{2}) = 0 \tag{6.22}$$

Finally to ensure that the anisotropic flow function satisfies the tetragonal symmetry condition, it must hold that

$$f(\theta) = f(90° - \theta) = 0 \tag{6.23}$$

This means that if the specified orientation angle θ lies between 45° and 90°, $90° - \theta$ must be used in Eq. 6.22 instead of θ.

7

Numerical Implementation

The fundamentals of the finite element method and particularly spatial discretization have already been discussed to some extent in Chapter 5. In this chapter, more attention is given to the temporal discretization and other aspects of numerical implementation that are more relevant and challenging in the context of this work.

7.1 Time Integration

Time integration methods play a crucial role in finite element analysis (FEA), especially when solving time-dependent problems such as dynamic structural simulations, heat transfer, and fluid flow. These methods discretize the time domain, transforming differential equations into algebraic equations that can be solved numerically. Time integration methods can be broadly classified into ***explicit*** and ***implicit*** schemes.
Explicit Methods, such as the Forward Euler or central difference scheme, calculate the state at the next time step directly from the previous step, as

follows:

$$u_{n+1} = u_n + \left(\frac{\mathrm{d}u}{\mathrm{d}t}\right)_n \cdot \Delta t = u_n + \Delta u_n \tag{7.1}$$

where n denotes the time step index and Δt represents the time step size. They are computationally efficient, but require small time steps to maintain stability.
The implicit method is a time-stepping approach in which the unknown future state of a system depends on itself. This requires solving a system of equations at each time step iteratively, making it more computationally expensive but also more stable than explicit methods. The Backward Euler method is a common implicit integration scheme, described as follows:

$$u_{n+1} = u_n + \left(\frac{\mathrm{d}u}{\mathrm{d}t}\right)_{n+1} \cdot \Delta t = u_n + \Delta u_{n+1} \tag{7.2}$$

Unlike the explicit method, where u_{n+1} is computed directly from known values u_n, this equation contains u_{n+1} on both sides. This means that we need to solve for u_{n+1} at each step, often requiring iterative methods like Newton-Raphson.

7.1.1 Implicit Methods

Plasticity models are governed by differential-algebraic equations (DAE), meaning they consist of both time-dependent differential equations and algebraic constraints such as the yield condition $F = 0$, which must be enforced concurrently during the solution process. In such problems, implicit methods are preferred because they ensure stability and allow larger time steps, making them ideal for quasistatic loading and highly nonlinear material behavior. Unlike explicit methods, which require very small time steps due to the stability criterion for time step size, known as Courant-Friedrichs-Lewy (CFL) condition, implicit methods are far less sensitive to time-step size. The trial stress approach is commonly used in implicit plasticity solvers, where an initial elastic predictor (trial stress) is computed. If this stress exceeds the yield criterion, a plastic corrector is applied using iterative methods (e.g., Newton-Raphson) to enforce plastic consistency and update internal variables like plastic strain and hardening parameters.
Fig. 7.1(a) illustrates a von Mises yield surface alongside a schematic of the explicit integration method described earlier. In this method, the updated stresses are pushed outside the yield surface after a time step. In contrast,

Fig. 7.1(b) shows the implicit integration approach. Here, a trial stress increment is chosen that initially moves the updated stresses, $\boldsymbol{\sigma}^{\mathrm{tr}}_{t+\Delta t}$, outside the yield surface. Then a plastic correction is applied to adjust the stress and bring it back to the yield surface at the new time $t + \Delta t$.

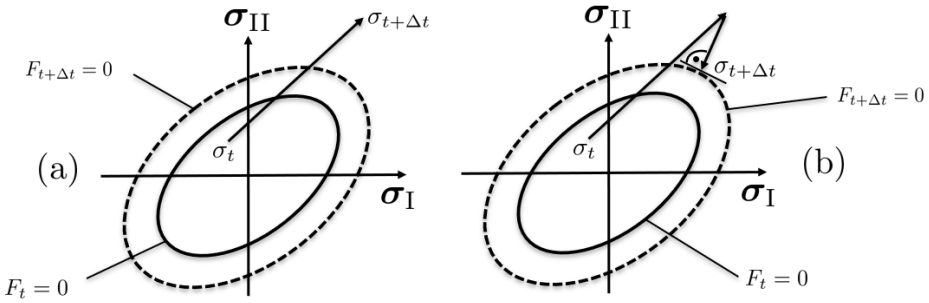

Figure 7.1: Schematic illustrations of (a) explicit integration and (b) implicit integration using the radial return method for the von Mises plasticity equations.

Finite Element Analysis (FEM) is always treated incrementally, where the problem is solved step by step by considering small changes in load or time at each stage. Unless stated otherwise, for simplicity, we will assume that all quantities refer to the values at the end of a time step, $t + \Delta t$. Therefore, the stress at $t + \Delta t$ is simply denoted as $\boldsymbol{\sigma}$, while the stress at the beginning of the time step, at time t, is $\boldsymbol{\sigma}_t$.
The elastic strain at the end of the time step may be written as

$$\boldsymbol{\varepsilon}^e = \boldsymbol{\varepsilon}^e_t + \Delta\boldsymbol{\varepsilon}^e = \boldsymbol{\varepsilon}^e_t + \Delta\boldsymbol{\varepsilon} - \Delta\boldsymbol{\varepsilon}^p \tag{7.3}$$

after inserting Eq. 7.3 into Hooke's law (Eq. 4.24) we get

$$\boldsymbol{\sigma} = \boldsymbol{C} : (\boldsymbol{\varepsilon}^e_t + \Delta\boldsymbol{\varepsilon} - \Delta\boldsymbol{\varepsilon}^p) \tag{7.4}$$

so that

$$\boldsymbol{\sigma} = \underbrace{(\boldsymbol{C} : \boldsymbol{\varepsilon}^e_t + \boldsymbol{C} : \Delta\boldsymbol{\varepsilon})}_{\text{Trial stress}} - \underbrace{(\boldsymbol{C} : \Delta\boldsymbol{\varepsilon}^p)}_{\text{Plastic corrector}} \tag{7.5}$$

so then

$$\boldsymbol{\sigma} = \boldsymbol{\sigma}^{tr} - \boldsymbol{C} : \Delta\boldsymbol{\varepsilon}^p. \tag{7.6}$$

With applying Eq. 4.59 into Eq. 7.6 gives

$$\boldsymbol{\sigma} = \boldsymbol{\sigma}^{tr} - \Delta\lambda \boldsymbol{C} : \frac{\partial f}{\partial \boldsymbol{\sigma}} \tag{7.7}$$

where using the flow function f according to Eq. 6.17

$$\frac{\partial f}{\partial \boldsymbol{\sigma}} = \frac{3}{2}\frac{\boldsymbol{\sigma}'}{q} + \frac{a}{2}\boldsymbol{I} \tag{7.8}$$

where $\boldsymbol{\sigma}'$ refers to the stress deviator and $\boldsymbol{I}$ to the identity tensor.
Due to the definition of J_2, the following identity holds [29]

$$\frac{\boldsymbol{\sigma}'}{J_2(\boldsymbol{\sigma}')} = \frac{\boldsymbol{\sigma}'^{\,tr}}{J_2(\boldsymbol{\sigma}'^{\,tr})} \tag{7.9}$$

which leads to this equality

$$\frac{\partial f}{\partial \boldsymbol{\sigma}} = \frac{\partial f}{\partial \boldsymbol{\sigma}^{tr}} = \boldsymbol{n} \tag{7.10}$$

its substitution into the stress update formula (Eq. 7.7) gives

$$\boldsymbol{\sigma} = \boldsymbol{\sigma}^{tr} - \Delta\lambda \boldsymbol{C} : \frac{\partial f}{\partial \boldsymbol{\sigma}^{tr}} = \boldsymbol{\sigma}^{tr} - \underbrace{(\Delta\lambda \boldsymbol{C} : \boldsymbol{n})}_{\Delta\boldsymbol{\sigma}^{pl}} \tag{7.11}$$

so finally we obtain

$$\boldsymbol{\sigma} = \boldsymbol{\sigma}^{tr} - \Delta\boldsymbol{\sigma}^{pl} \tag{7.12}$$

which actually means

$$\boldsymbol{\sigma}_{t+\Delta t} = \boldsymbol{\sigma}^{tr}_{t+\Delta t} - \Delta\boldsymbol{\sigma}^{pl}_{t+\Delta t} \tag{7.13}$$

Thus, from Eq. 7.13, it is evident that the updated stress at the end of the time step depends on both the initial values at the beginning of the time step t, which are implicitly included in the trial stress, and the values at the end of the time step $t + \Delta t$.

7.2 Implementation in ABAQUS®

In this Section, the implementation of the developed material model within the finite element software ABAQUS® is presented. Although the ABAQUS® library provides various material models that can be easily applied through the ABAQUS®-CAE (Abaqus user interface), more complex material models require custom implementation. This can be achieved in ABAQUS® using the so-called Material User Subroutine **UMAT**, which allows users to define a custom constitutive behavior by specifying the stress-strain relationship at the integration point level. This flexibility is particularly useful for advanced material models that cannot be accurately represented using the built-in options. In UMAT, users provide the algorithm for updating stress and state variables based on the strain increment, enabling the simulation of complex phenomena such as anisotropy, nonlinearity, and rate dependence. Since the UMAT code must be written in Fortran, ABAQUS® first needs to be linked to a Fortran compiler. This linkage ensures that the custom subroutine is correctly compiled and integrated into the ABAQUS® simulation environment. Proper configuration of the compiler settings and environment variables is crucial to avoid compatibility issues and compilation errors. Additionally, the version compatibility between Abaqus and the Fortran compiler must be carefully checked to ensure seamless execution of the user-defined material model. Fig. 7.2 shows a schematic representation of where exactly the UMAT is called in a non-linear FE analysis.

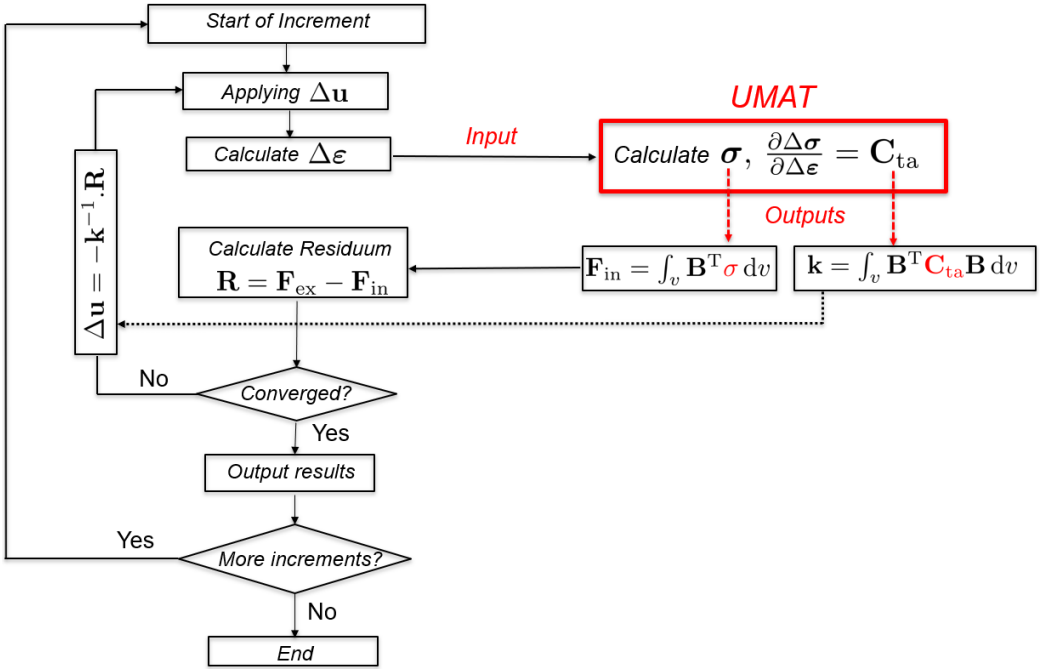

Figure 7.2: Schematic representation of a typical non-linear FE analysis hierarchy, highlighting the specific location where the UMAT is called.

Basically, within the UMAT, the strain increment $\Delta\boldsymbol{\varepsilon}$ at the beginning of the increment is provided as an input, along with the stress $\boldsymbol{\sigma}$ and the material Jacobian matrix $\dfrac{\partial\Delta\boldsymbol{\sigma}}{\partial\Delta\boldsymbol{\varepsilon}}$ from the previous increment. These quantities are updated through the user-defined algorithm. At the end of the increment, the updated stress and Jacobian are returned to ABAQUS® as output variables. This process ensures the consistent transfer of information between the custom material model and the finite element solver, allowing ABAQUS® to accurately compute the global equilibrium. In the hierarchy illustrated in Fig. 7.2, $\mathbf{k}$ represents the tangential element stiffness matrix, and $\mathbf{F}_{\mathrm{in}}$ denotes the vector of internal forces. In this context, the matrix $\mathbf{B}$ is defined as the product of the shape function matrix $\mathbf{N}$ and the differential operator $\mathbf{D}$, i.e., $\mathbf{B} = \mathbf{DN}$. The vector of external forces is denoted by $\mathbf{F}_{\mathrm{ex}}$.
Fig. 7.3 provides a detailed overview of all ABAQUS® variables and their corresponding dimensions, as defined in the UMAT header for input and output purposes. Depending on the type of analysis that is performed, certain variables can be utilized within the UMAT code. In an elastoplastic material model, STRESS, DDSDDE (Material Jacobian), and STATEV (Solution-

dependent state variables) are the most important variables that need to be computed and updated. Accurate calculation and consistent updating of these variables are crucial for capturing the non-linear behavior of the material and ensuring the convergence of the finite element solution.

```
      SUBROUTINE UMAT(STRESS,STATEV,DDSDDE,SSE,SPD,SCD,
     1 RPL,DDSDDT,DRPLDE,DRPLDT,
     2 STRAN,DSTRAN,TIME,DTIME,TEMP,DTEMP,PREDEF,DPRED,CMNAME,
     3 NDI,NSHR,NTENS,NSTATV,PROPS,NPROPS,COORDS,DROT,PNEWDT,
     4 CELENT,DFGRD0,DFGRD1,NOEL,NPT,LAYER,KSPT,JSTEP,KINC)

      DIMENSION STRESS(NTENS),STATEV(NSTATV),
     1 DDSDDE(NTENS,NTENS),DDSDDT(NTENS),DRPLDE(NTENS),
     2 STRAN(NTENS),DSTRAN(NTENS),TIME(2),PREDEF(1),DPRED(1),
     3 PROPS(NPROPS),COORDS(3),DROT(3,3),DFGRD0(3,3),DFGRD1(3,3),
     4 JSTEP(4)
```

Figure 7.3: The UMAT header includes all variables and their corresponding dimensions that are passed from ABAQUS® into the UMAT.

STATEV is an array used to store state variables that are updated during each integration point at every step of the analysis. These state variables are used to track internal material states that evolve during the simulation, such as plastic strains, damage variables, etc. In order to update the aforementioned variables within each time increment in the UMAT, some material parameters such as Young's modulus, Poisson's ratio and others need to be input into the UMAT. These parameters are stored in the PRPOS array within the UMAT.
Within the framework of our developed anisotropic elastoplastic material model, seven material parameters need to be specified in the UMAT, as shown in Fig. 7.4. These include elastic parameters, plastic or hardening moduli and an additional parameter, the material orientation angle θ, to account for anisotropy. The material orientation angle θ must be entered separately, as ABAQUS® does not automatically pass it to the UMAT.

```
-----------------------------------------------
PROPS(1) - Young's Modulus (MPa)
PROPS(2) - Poisson's Ratio
PROPS(3) - Shear Modulus (MPa)
PROPS(4) - Initial Yield Stress (MPa)
PROPS(5) - Hardening Modulus
PROPS(6) - Parameter 'a' in Yield Function
PROPS(7) - Orientation Angle (Radian)


-----------------------------------------------
```

Figure 7.4: The list of all necessary material parameters for the developed material model, which are stored within the PROPS array in the UMAT.

The mentioned material parameters must first be defined in ABAQUS®-CAE within the "Material" modul under the Material Behaviors "User Material" as Mechanical Constants (see Fig. 7.5). This allows them to be accessed within the UMAT. Additionally, the number of state variables (STATEV) must also be specified, which is represented as "Depvar" in ABAQUS®-CAE under the Material Behaviors as well (see Fig. 7.5).

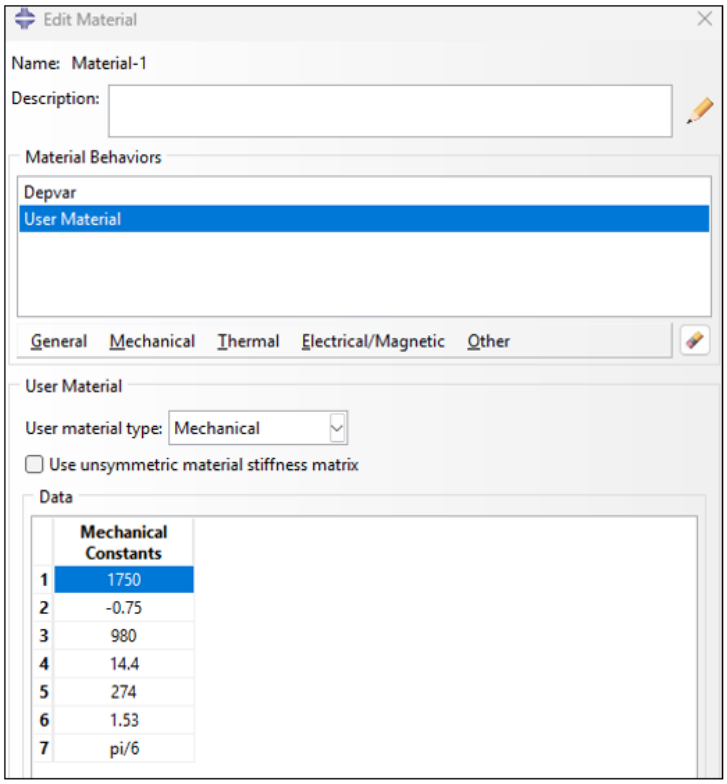

Figure 7.5: The corresponding material window in ABAQUS®-CAE, where the material parameters and the number of STATEV are defined.

In the developed material model, the accumulated plastic strain is the only STATEV within the UMAT. The material parameters listed in Fig. 7.5 are experimentally determined. This allows us to later compare and validate the model results against real experimental data.

7.3 Newton–Raphson Method

The Newton-Raphson method is a powerful and widely used iterative technique for solving non-linear equations in Finite Element analysis. It is particularly effective for handling complex, non-linear systems arising from material behavior, large deformations, and boundary conditions. The method involves linearizing the non-linear equilibrium equations through a Taylor series expansion, iteratively updating the solution by solving a sequence of

linearized equations. Each iteration refines the approximation by evaluating the residual and the tangent stiffness matrix, ultimately converging to an accurate solution. Its quadratic convergence rate makes it highly efficient, although convergence depends on a good initial guess and the nature of the non-linearity. The method is based on an iterative procedure used to find the roots of a non-linear equation $f(u) = 0$. The core idea is to approximate the non-linear function using its tangent line, which is a first-order Taylor series expansion. The iterative formula is:

$$u_{k+1} = u_k - \frac{f(u_k)}{f'(u_k)} \tag{7.14}$$

where k denotes the iteration number. The process begins with an initial guess u_0 and progressively refines the solution with each iteration until it reaches the specified tolerance.
In the context of the Finite Element Method (FEM), the Newton-Raphson method is used to solve the non-linear equilibrium equation

$$\mathbf{R}(\mathbf{u}) = \mathbf{F}_{\text{ex}} - \mathbf{F}_{\text{in}}(\mathbf{u}) = 0 \tag{7.15}$$

The update rule becomes

$$\mathbf{u}_{k+1} = \mathbf{u}_k - \mathbf{K}^{-1}\mathbf{R}(\mathbf{u}_k) \tag{7.16}$$

where:

- $\mathbf{u}$ is the vector of nodal displacements.
- $\mathbf{R}$ is the residual vector.
- $\mathbf{K} = \frac{\partial \mathbf{R}}{\partial \mathbf{u}}$ is the tangent stiffness matrix.

In ABAQUS®, the Newton's method algorithms for solving equilibrium equations are integrated into the program, so the user does not need to write the corresponding code manually.

7.4 Determination of Plastic Multiplier

The plastic multiplier λ plays a crucial role in the implementation of a plasticity model. It determines the magnitude of the plastic strain in each increment and, therefore, directly influences the stability of the numerical solution. In

implicit methods, trial stress is the central known quantity, which requires formulation of the increment of the plastic multiplier $\Delta\lambda$ as a function of the trial stress $\boldsymbol{\sigma}^{tr}$.
We begin with the developed yield function (Eq. 6.17) and analyze each term individually. From the definition of q (6.10) we can write

$$q = \sqrt{\frac{3}{2}\boldsymbol{\sigma}' : \boldsymbol{\sigma}'} = \sqrt{\frac{3}{2}(\boldsymbol{\sigma} - \frac{1}{2}\mathrm{tr}(\boldsymbol{\sigma})) : (\boldsymbol{\sigma} - \frac{1}{2}\mathrm{tr}(\boldsymbol{\sigma}))} \tag{7.17}$$

inserting Eq. 7.12 in Eq. 7.17

$$q = \sqrt{\frac{3}{2}(\boldsymbol{\sigma}^{tr} - \Delta\boldsymbol{\sigma}^{pl} - \frac{1}{2}\mathrm{tr}(\boldsymbol{\sigma})) : (\boldsymbol{\sigma}^{tr} - \Delta\boldsymbol{\sigma}^{pl} - \frac{1}{2}\mathrm{tr}(\boldsymbol{\sigma}))} \tag{7.18}$$

It has been derived in [29]

$$\boldsymbol{\sigma}^{tr} - \frac{1}{2}\mathrm{tr}(\boldsymbol{\sigma}) = \boldsymbol{\sigma}'^{\,tr} \tag{7.19}$$

Here, $\boldsymbol{\sigma}'^{\,tr}$ denotes the deviatoric part of the trial stress tensor. By inserting Eq. 7.19 into Eq. 7.18, we obtain

$$q = \sqrt{\frac{3}{2}(\boldsymbol{\sigma}'^{\,tr} - \Delta\boldsymbol{\sigma}^{pl}) : (\boldsymbol{\sigma}'^{\,tr} - \Delta\boldsymbol{\sigma}^{pl})} \tag{7.20}$$

Now, we expand the product in Eq. 7.20

$$q = \sqrt{(q^{tr})^2 - 3(\boldsymbol{\sigma}'^{\,tr} : \Delta\boldsymbol{\sigma}^{pl}) + \frac{3}{2}(\Delta\boldsymbol{\sigma}^{pl} : \Delta\boldsymbol{\sigma}^{pl})} \tag{7.21}$$

Next, we express $\Delta\boldsymbol{\sigma}^{pl}$ using its original components as defined in Eq. 7.11. This yields

$$q = \sqrt{(q^{tr})^2 - 3\lambda(\boldsymbol{\sigma}'^{\,tr} : \mathbf{C} : \mathbf{n}) + \frac{3}{2}\Delta\lambda^2(\mathbf{C} : \mathbf{n}) : (\mathbf{C} : \mathbf{n})} \tag{7.22}$$

In this equation, $\overset{4}{\mathbf{C}}$ denotes the fourth-order elasticity tensor, while $\mathbf{n}$ signifies the flow direction as a second-order tensor. Now, for the sake of clarity and simplification, we assume:

$$\overset{4}{\mathbf{C}} : \mathbf{n} = \mathbf{B} \tag{7.23}$$

where $\mathbf{B}$ represents a second-order tensor, which implies

$$q = \sqrt{(q^{tr})^2 - 3\Delta\lambda(\boldsymbol{\sigma}'^{\,tr} : \mathbf{B}) + \frac{3}{2}\Delta\lambda^2(\mathbf{B} : \mathbf{B})} \tag{7.24}$$

In Eq. 7.24 there are two tensor multiplications, each resulting in a scalar value

$$\boldsymbol{\sigma}'^{\,tr} : \mathbf{B} = \alpha \tag{7.25}$$

$$\mathbf{B} : \mathbf{B} = \beta \tag{7.26}$$

this leads to

$$q = \sqrt{(q^{tr})^2 - 3\Delta\lambda\alpha + \frac{3}{2}\Delta\lambda^2\beta} \tag{7.27}$$

so now the q is formulated as a function of $\boldsymbol{\sigma}'^{\,tr}$ and $\Delta\lambda$, which results in a scalar as well.
Next, we examine the second term in the yield function Eq. 6.17, i.e. *ap*. The same methodology applied to q is also used here, as outlined below.

$$ap = a(-\frac{\mathrm{Tr}(\boldsymbol{\sigma})}{2}) \tag{7.28}$$

$$\mathrm{Tr}(\boldsymbol{\sigma}) = \mathrm{Tr}(\boldsymbol{\sigma}^{tr} - \Delta\boldsymbol{\sigma}^{pl}) = \mathrm{Tr}(\boldsymbol{\sigma}^{tr}) - \mathrm{Tr}(\Delta\boldsymbol{\sigma}^{pl}) \tag{7.29}$$

$$\mathrm{Tr}(\Delta\boldsymbol{\sigma}^{pl}) = \mathrm{Tr}(\Delta\lambda(\mathbf{C} : \mathbf{n})) = \Delta\lambda\mathrm{Tr}(\mathbf{B}) \tag{7.30}$$

$$ap = -\frac{a}{2}[\mathrm{Tr}(\boldsymbol{\sigma}^{tr}) - \Delta\lambda\mathrm{Tr}(\mathbf{B})] \tag{7.31}$$

and finally the last component of yield function, i.e. $b'(\sigma_F)$ needs to be adjusted. From Eq. 6.22 the $b'(\sigma_F)$ was identified as

$$b'(\sigma_F) = \sigma_F \cos(\theta)(1 + \frac{a}{2}) \tag{7.32}$$

where

$$\sigma_F = \sigma_0 + k\bar{\varepsilon}^p \tag{7.33}$$

Relation 7.34 states that the plastic work done must be the same when the corresponding tensor multiplication is replaced by the equivalent (effective) values

$$\boldsymbol{\sigma} : \Delta\boldsymbol{\varepsilon}^p = \sigma_e \Delta\bar{\varepsilon}^p \tag{7.34}$$

where

$$\sigma_e = q - ap \tag{7.35}$$

After inserting the Eq. 7.35 and the flow rule Eq. 4.59 in Eq. 7.34, it can be derived that

$$\Delta\bar{\varepsilon}^p = \Delta\lambda \tag{7.36}$$

this leads to a definition of hardening equation in terms of plastic multiplier increment $\Delta\lambda$

$$\sigma_F = \sigma_0 + k\Delta\lambda \tag{7.37}$$

After all these steps, the yield function Eq. 6.17 was reformulated in such a way that a complex non-linear equation was created with respect to the plastic multiplier increment $\Delta\lambda$, which may be solved using the Newton–Raphson method.
Unlike the Newton method used for solving nonlinear equilibrium equations discussed in Sec. 7.3, the Newton iteration for computing the plastic multiplier $\Delta\lambda$ must be explicitly implemented by the user within the UMAT subroutine in form of the finite element code. In the last section, the yield function f could be expressed in terms of the plastic multiplier increment $\Delta\lambda$. Consequently, the corresponding Newton's equation, derived from Eq. 7.14, is as follows

$$\Delta\lambda_{k+1} = \Delta\lambda_k - \frac{f(\Delta\lambda_k)}{f'(\Delta\lambda_k)} \tag{7.38}$$

Therefore, to compute $\Delta\lambda$ in Eq. 7.38, the derivative of the yield function f (Eq. 6.17) with respect to $\Delta\lambda$ must be determined, which using the chain rule takes the following form

$$\frac{\partial f}{\partial \Delta\lambda} = \frac{\partial f}{\partial q}\frac{\partial q}{\partial \Delta\lambda} + \frac{\partial f}{\partial p}\frac{\partial p}{\partial \Delta\lambda} + \frac{\partial f}{\partial b'}\frac{\partial b'}{\partial \Delta\lambda} \tag{7.39}$$

From Eq. 7.27, we obtain

$$\frac{\partial f}{\partial q}, \frac{\partial q}{\partial \Delta\lambda} = \frac{3}{2\sqrt{q}} \left(\Delta\lambda, \beta - \alpha\right), \tag{7.40}$$

and from Eq. 7.31,

$$\frac{\partial f}{\partial p}, \frac{\partial p}{\partial \Delta\lambda} = -a \left(\frac{\mathrm{tr}(\beta)}{2}\right), \tag{7.41}$$

finally, using Eqs. 7.32 and 7.37,

$$\frac{\partial f}{\partial b'}, \frac{\partial b'}{\partial \Delta\lambda} = -k \cos\theta \left(\frac{a}{2} + 1\right). \tag{7.42}$$

where k refers to the linear hardening modulus.
So finally the increment of plastic multiplier $\Delta\lambda$ according to Eq. 7.38 results as follows

$$d\Delta\lambda = -\frac{q + \frac{a}{2}\mathrm{Tr}(\boldsymbol{\sigma}^{tr}) - \frac{a}{2}\Delta\lambda\mathrm{Tr}(\mathbf{B}) - b'}{\frac{3}{2\sqrt{q}}(\Delta\lambda\beta - \alpha) - a(\frac{\mathrm{Tr}(\mathbf{B})}{2}) - k\cos(\theta)(\frac{a}{2} + 1)} \tag{7.43}$$

where

$$\Delta\lambda_{k+1} = \Delta\lambda_k + d\Delta\lambda_k \tag{7.44}$$

7.5 Numerical Material Tangent

In implicit FEA, the material tangent (or stiffness matrix/Jacobian) defined as $\dfrac{\partial \boldsymbol{\sigma}}{\partial \boldsymbol{\varepsilon}}$ is essential for capturing non-linear material behavior. It linearizes the sensitivity of stress to strain changes, enabling rapid and accurate convergence in the iterative solution process to solve the global equilibrium equation system. The flowchart in Fig. 7.2 schematically illustrates where and how the material tangent $\mathbf{C}_{\mathrm{ta}}$ influences the global computation process. An inaccurate material tangent can hinder convergence and lead to unreliable results. Deriving the material tangent is challenging, particularly for complex material models with non-linear and path-dependent behaviors. Analytical derivation is often time-consuming and must be adjusted whenever constitutive equations change. To simplify this process, numerical methods such as finite difference methods or automatic differentiation can be used to ap-

proximate the tangent. However, these approaches may introduce numerical issues such as roundoff errors, truncation errors, step size sensitivity, and instability, especially due to floating point arithmetic [81].
Finite difference methods approximate derivatives by discretizing them over a finite interval, using forward, backward, or central differences. While they provide a simple way to compute derivatives numerically, they are susceptible to truncation errors and require careful step size selection to ensure accuracy and stability.
In this context, the numerical computation is demonstrated using a forward difference first-order scheme, characterized for its simplicity and straightforward implementation. This method approximates the derivative of a function $f(x)$ at a point x_i using the function values $f(x_i)$ and $f(x_{i+1})$. Mathematically, this can be written as:

$$f'(x_i) = \frac{f(x_{i+1}) - f(x_i)}{h} \tag{7.45}$$

where h represents the step size, also known as perturbation parameter. This method estimates the slope of the function over the interval $[x_i, x_{i+1}]$ and is first-order accurate, meaning the approximation error decreases linearly with the step size h. The goal is to compute the material Jacobian numerically using the forward difference method within ABAQUS® UMAT.
The constitutive law (Material model) defines the relationship between the applied strain $\boldsymbol{\varepsilon}$ (second-order tensor) and the resulting second-order stress tensor $\boldsymbol{\sigma}$. In ABAQUS®, the strain $\boldsymbol{\varepsilon}$ is represented by the one-dimensional arrays STRAN(6) (total strain) and DSTRAN(6) (strain increments), capturing the material's deformation. The UMAT routine then calculates the stress $\boldsymbol{\sigma}$, which is returned via the STRESS (6) array. The Jacobian material tangent $\mathbf{C}$ (a fourth-order tensor showing the partial derivatives of stress with respect to strain) is conveyed through DDSDDE(6×6). To apply the first-order forward difference scheme for computing the Jacobian, each of the six components of the strain vector STRAN(6) is perturbed individually by adding a disturbance value ε_d. During each perturbation step j (ranging from 1 to 6), only one component of STRAN(6) is modified, resulting in the perturbed strain vector $\mathrm{STRAN_d}(6)$, while all other components remain unchanged. For each step j, a column of the disturbed stress matrix $\mathrm{STRESS_d}(6{\times}6)$ is obtained, where the second index represents the perturbation step j, and the first index i (ranging from 1 to 6) corresponds to the stress response component. The undisturbed stress vector $\mathrm{STRESS_{ud}}(6)$ is calculated during an undisturbed step (i = 7) by evaluating the material routine with the original strain vector $\mathrm{STRAN_{ud}}(6)$.

By analyzing the stress changes caused by these perturbations, the partial derivatives of stress with respect to each strain component and thus the Jacobian material tangent $\mathbf{C}$ can be approximated:

$$C(i,j) = \frac{STRESS_d(i,j) - STRESS_{ud}(i)}{\varepsilon_d(j)} \tag{7.46}$$

where $C(i,j)$ represents the approximated fourth-order Jacobian material tangent tensor, which in ABAQUS®-UMAT is returned through the field DDSDDE(6×6). The value of the perturbation strain ε_d is limited by the precision of the floating point. In a double-precision environment, the limit for ε_d for each perturbation step j is given by [23]:

$$\varepsilon_d(j) = \max(1.0 \times 10^{-8}, \mathrm{Abs}\,(1.0 \times 10^{-8} \cdot \mathrm{STRAN_{ud}}(j))) \tag{7.47}$$

However in the context of this work, it was found through experience that the following expression for ε_d yielded the best results for achieving convergence:

$$\varepsilon_d(j) = \max(1.0 \times 10^{-4}, \mathrm{Abs}\,(1.0 \times 10^{-4} \cdot \mathrm{STRAN_{ud}}(j))) \tag{7.48}$$

7.6 Results and Model Validation

In this section, the simulation results from the elasto-plastic material model were evaluated and compared with the corresponding experimental data. Auxetic sheets with pattern orientation angles of $\theta = 0°$, $15°$, $30°$, and $45°$ were considered. The results demonstrate that the developed model and its implementation can accurately capture the real behavior of the sheets, including their anisotropic response under mechanical loading. The model reliably reproduces the direction-dependent deformation patterns observed in the experiments, reflecting the influence of the pattern orientation on the auxetic behavior. This indicates that the model is robust and reliable in predicting the mechanical performance of auxetic structures with varying orientations.
In the following, samples with different θ are presented separately, each focusing on the specific behavior and characteristics associated with their unique orientations.

Sample with $\theta = 0°$

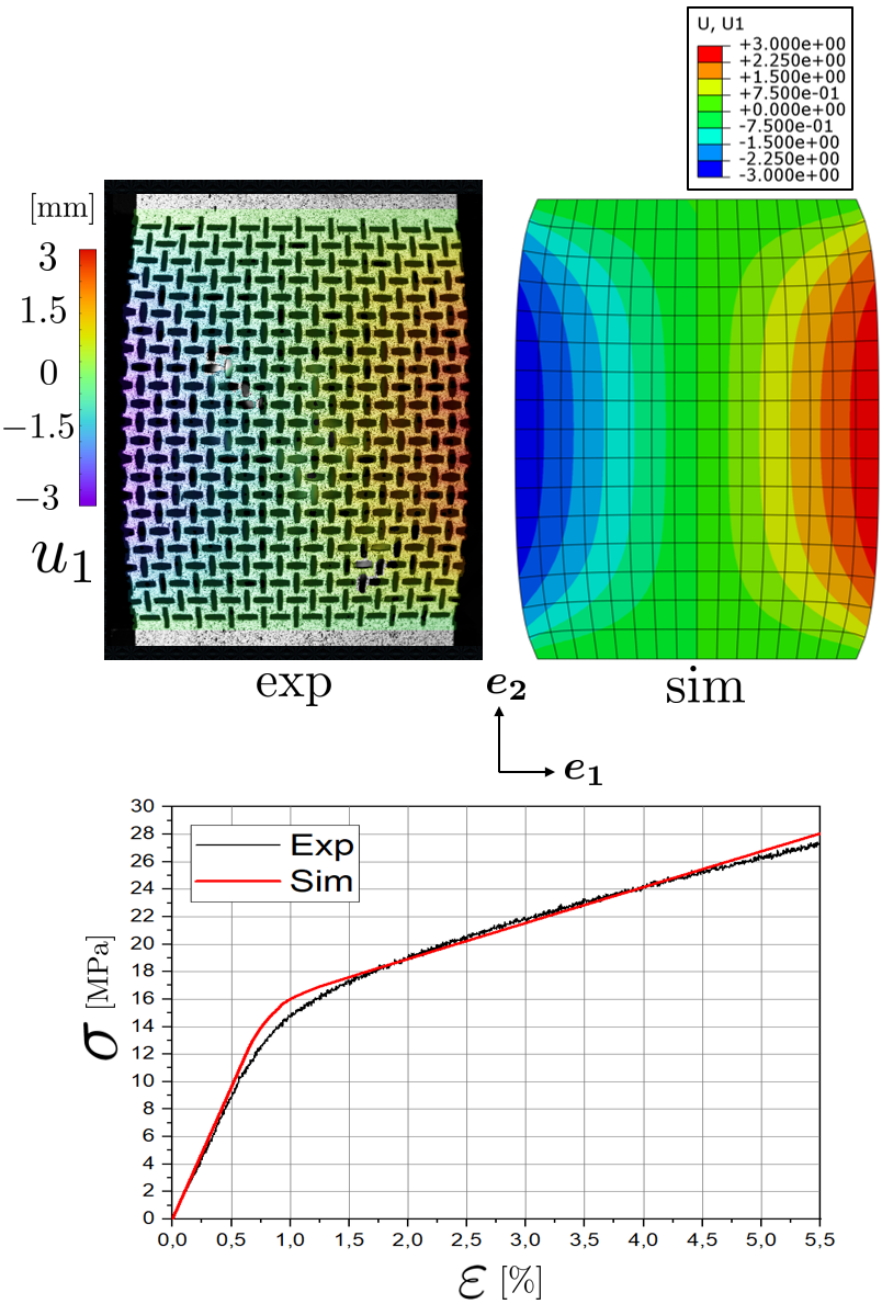

Figure 7.6: Comparison of experimental and simulated transverse displacements (u_1) and the corresponding global stress-strain curve for sample with $\theta = 0°$ after approx. 6% global strain induced from uniaxial tension in the e_2-direction.

Sample with $\theta = 15°$

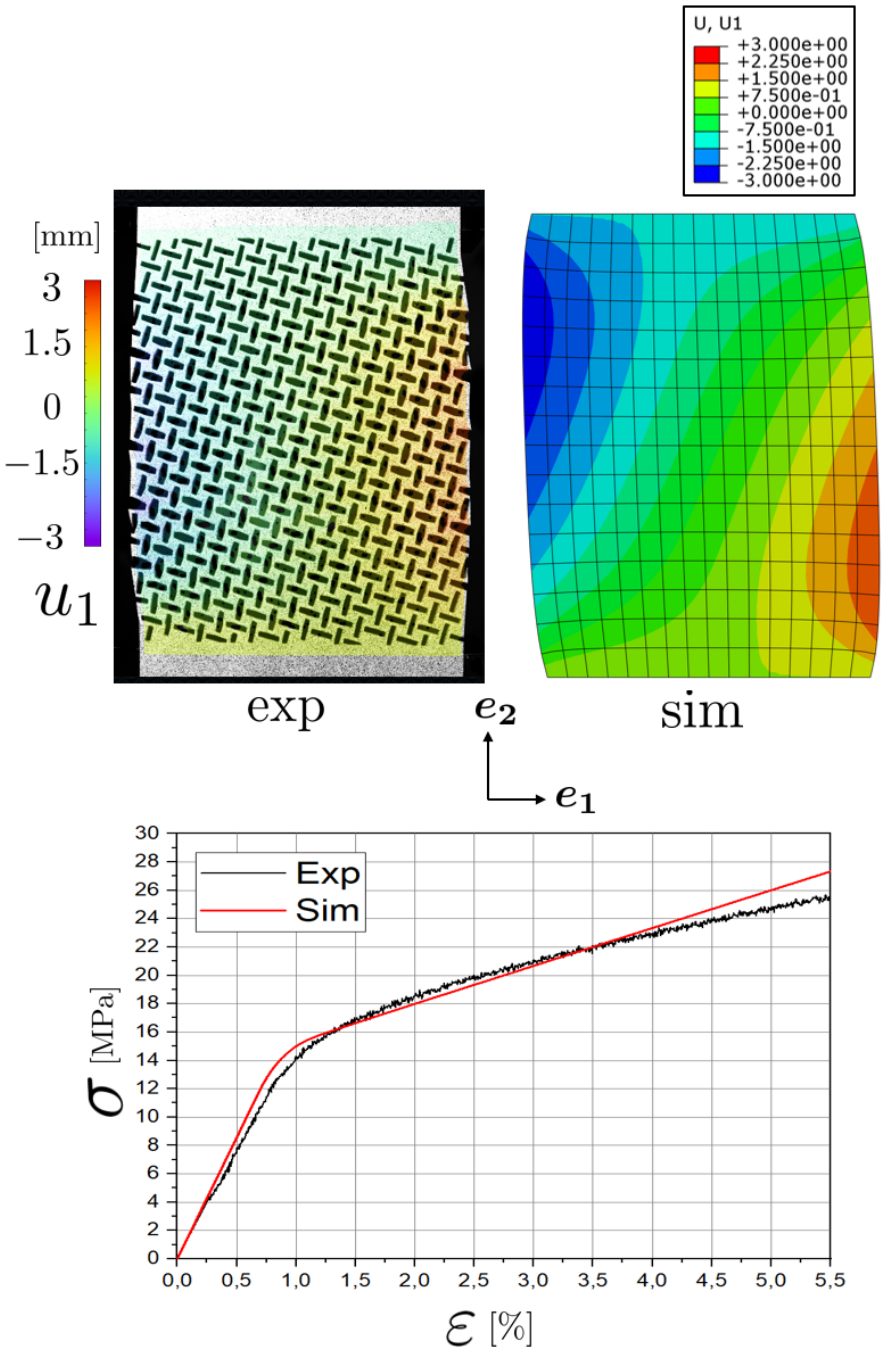

Figure 7.7: Comparison of experimental and simulated transverse displacements (u_1) and the corresponding global stress-strain curves for sample with $\theta = 15°$ after approx. 6% global strain induced from uniaxial tension in the e_2-direction.

Sample with $\theta = 30°$

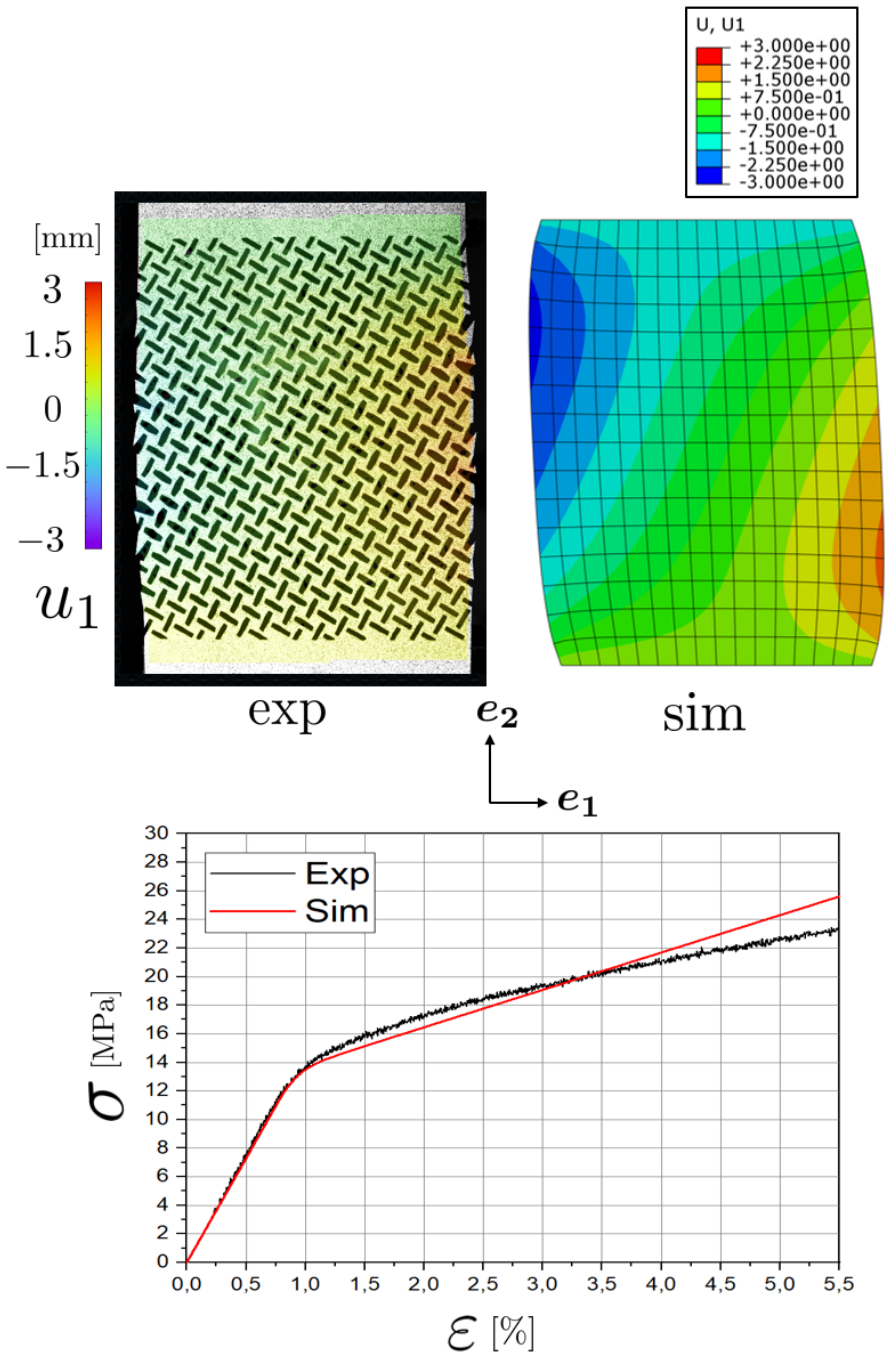

Figure 7.8: Comparison of experimental and simulated transverse displacements (u_1) and the corresponding global stress-strain curves for sample with $\theta = 30°$ after approx. 6% global strain induced from uniaxial tension in the e_2-direction.

Sample with $\theta = 45°$

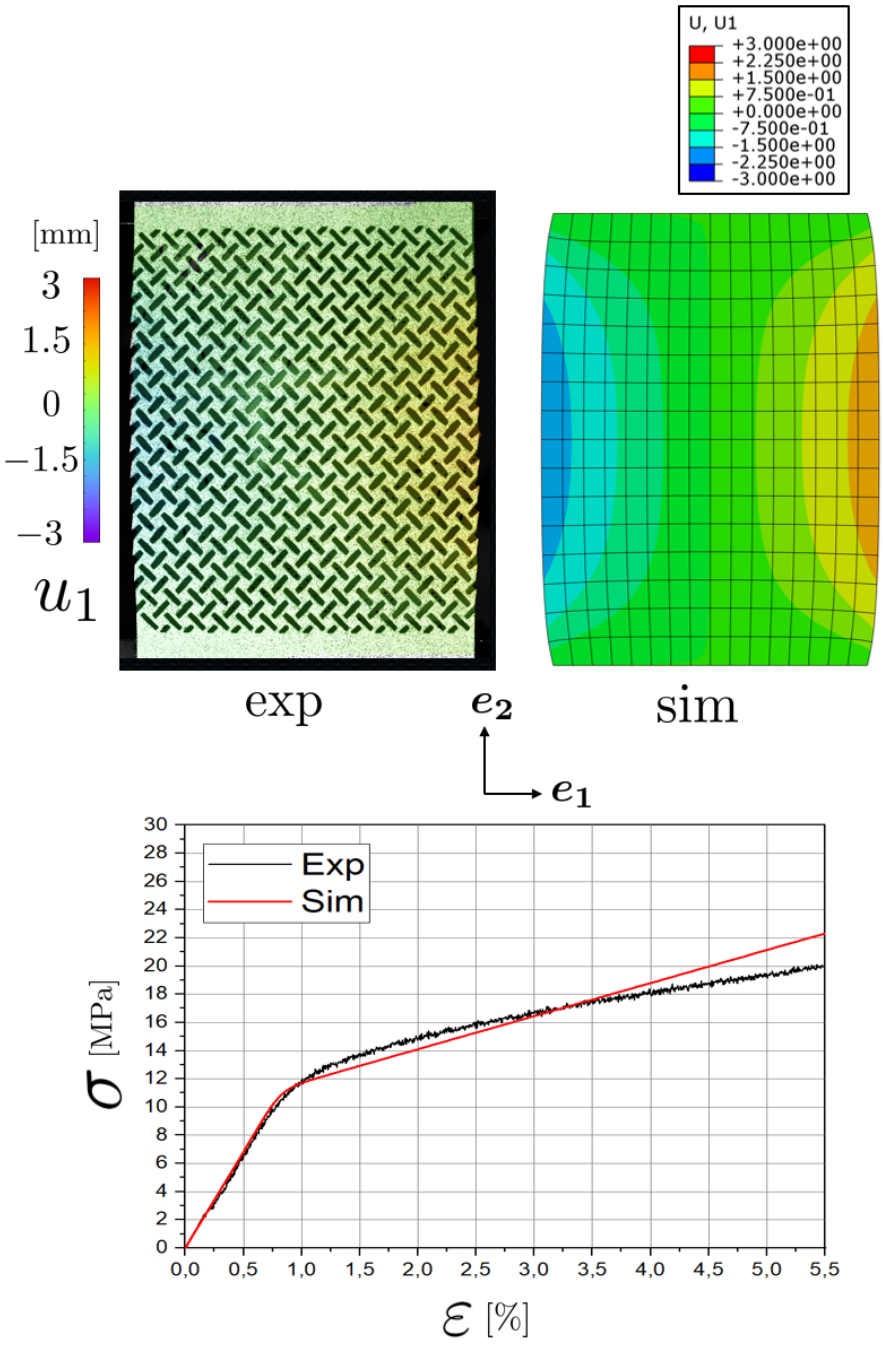

Figure 7.9: Comparison of experimental and simulated transverse displacements (u_1) and the corresponding global stress-strain curves for sample with $\theta = 45°$ after approx. 6% global strain induced from uniaxial tension in the e_2-direction.

8

Conclusion and Future Works

8.1 Conclusion

This dissertation presents a comprehensive investigation into the mechanical behavior and numerical modeling of auxetic sheet metal structures, with a particular focus on rotating unit patterns in AlMg3 aluminum alloy sheets. The aim was to enhance understanding of auxetic metamaterials for lightweight structural applications and to provide validated material models that can serve both theoretical development and practical implementation in design processes.

A robust experimental methodology was developed and executed, encompassing uniaxial and biaxial tensile tests, advanced characterization techniques such as Digital Image Correlation (DIC) and Infrared Thermography (IRT), and systematic variations in geometrical parameters namely pattern size, aspect ratio and orientation angle. These experimental studies revealed that the auxetic effect, mechanical stiffness and failure behavior are highly sensitive to microstructural configurations. For instance, increasing the aspect ratio of the rectangular perforations enhanced the auxetic behavior (more negative Poisson's ratio) but resulted in reduced stiffness and strength. Similarly, altering the orientation angle led to pronounced anisotropy, diminishing the global auxetic effect while impacting yield stress and stiffness. This

observation arises from the deformation mechanism of the auxetic sheet, characterized by the rigid body rotation of square units and localized deformation in the struts between perforations. An increased aspect ratio naturally leads to thinner struts, thereby enabling greater rigid body rotation of the square units and consequently, enhance the auxetic effect.
Another significant contribution lies in the methodological framework developed for transferring microstructural behavior into macroscopic material model. By integrating continuum mechanics theory with experimental data and numerical simulations, this framework enables efficient and accurate modeling of auxetic and potentially other metamaterial systems. Numerical homogenization played a central role in this process. By identifying the 2×2 unit cell as a representative volume element (RVE) and applying periodic boundary conditions (PBCs), it was possible to determine the effective microscale properties and assign them to material points within a homogeneous continuum.
From a computational standpoint, fully resolved finite element simulations and numerical homogenization were conducted to replicate the mechanical behavior observed experimentally. These simulations confirmed the significant anisotropy induced by pattern orientation and geometric design. A major outcome of this numerical work was the derivation of an anisotropic elasto-plastic material model based on the existing tetragonal symmetry incorporating a pressure-sensitive plastic yield surface. This model was implemented in ABAQUS® through a user-defined material subroutine (UMAT), incorporating robust numerical schemes such as implicit time integration and Newton–Raphson iteration. The model was successfully validated against uniaxial tests data, capturing key characteristics of the auxetic response, including stress-strain asymmetry and direction-dependent hardening. This modeling approach is highly adaptable and can be extended to different perforation geometries, base materials and loading conditions, thereby serving as a valuable tool for materials engineers and designers.
The findings not only expand our understanding of auxetic sheet metals but also pave the way for their application in high-performance, weight-sensitive structures such as aerospace components, protective equipment and morphing surfaces.

8.2 Future Works

Building on the insights and models developed in this dissertation, several promising avenues exist for future research. One key direction is the extension of current investigations from planar auxetic sheet metals to more complex shell structures. Shells, with their inherent curvature and additional geometric degrees of freedom, can amplify or modify auxetic effects under various loading conditions. Integrating auxetic behavior into shell geometries may unlock new functionalities for applications in morphing surfaces, aerospace components, and protective enclosures where stiffness, flexibility, and energy absorption must be balanced.

Additionally, the mechanical characterization methods employed in this work—primarily under quasi-static loading—should be extended to dynamic and fatigue loading scenarios. Such tests are crucial to understanding the long-term reliability and performance of auxetic structures under cyclic stresses, vibrations, and impact loads. Implementing high-speed DIC systems and time-resolved thermography could enable the capture of transient strain and thermal fields during dynamic events. This extension would not only validate the durability of auxetic designs but also inform the development of time-dependent material models such as viscoplastic or viscoelastic formulations.

Another promising direction is the use of artificial intelligence, and neural networks in particular, to enhance and extend the current modeling framework. The numerous datasets generated through extensive numerical simulations and experimental campaigns provide a strong foundation for data-driven surrogates capable of capturing complex, nonlinear material responses. Machine learning models could be trained to identify hidden patterns in stress–strain behavior, predict failure mechanisms, or accelerate large-scale simulations by serving as efficient constitutive approximators. Hybrid approaches that couple physics-based formulations with neural network enhancements may further improve predictive accuracy while preserving physical consistency. Such AI-driven methodologies hold significant potential for automating parameter calibration, optimizing auxetic designs, and enabling real-time structural response prediction.

Furthermore, exploring alternative base materials and manufacturing processes, including additive manufacturing, could lead to enhanced design flexibility and scale-up feasibility. Together, these extensions would broaden the applicability of auxetic metamaterials and deepen our understanding of their behavior under realistic service conditions.

Bibliography

[1] I. 16842:2021(E). Metallic materials – sheet and strip – biaxial tensile testing method using a cruciform test piece. 2021.

[2] B. E. Abali, H. Yang, and P. Papadopoulos. A computational approach for determination of parameters in generalized mechanics. *Higher gradient materials and related generalized continua*, pages 1–18, 2019.

[3] A. Alderson. A triumph of lateral thought. *Chemistry & Industry*, 17:384–391, 1999.

[4] A. Alderson, K. L. Alderson, D. Attard, K. E. Evans, R. Gatt, J. N. Grima, W. Miller, N. Ravirala, C. Smith, and K. Zied. Elastic constants of 3-, 4-and 6-connected chiral and anti-chiral honeycombs subject to uniaxial in-plane loading. *Composites Science and Technology*, 70(7):1042–1048, 2010.

[5] L. R. Alejano and A. Bobet. Drucker–prager criterion. In *The ISRM suggested methods for rock characterization, testing and monitoring: 2007-2014*, pages 247–252. Springer, 2014.

[6] H. Altenbach, T. Sadowski, et al. *Failure and damage analysis of advanced materials*. Springer, 2015.

[7] J. Altenbach and H. Altenbach. Einführung in die kontinuumsmechanik (teubner, stuttgart, 1994). *J. Acoust. Soc. Am*, 129(4):281–283, 2011.

[8] A. Bacigalupo and M. L. De Bellis. Auxetic anti-tetrachiral materials: equivalent elastic properties and frequency band-gaps. *Composite Structures*, 131:530–544, 2015.

[9] A. Bacigalupo, L. Gambarotta, et al. A micropolar model for the analysis of dispersive waves in chiral mass-in-mass lattices. *Frattura e Integrita Strutturale*, 29:1–8, 2014.

[10] F. Barlat, H. Aretz, J. W. Yoon, M. Karabin, J. Brem, and R. Dick. Linear transfomation-based anisotropic yield functions. *International journal of plasticity*, 21(5):1009–1039, 2005.

[11] F. Barlat, D. J. Lege, and J. C. Brem. A six-component yield function for anisotropic materials. *International journal of plasticity*, 7(7):693–712, 1991.

[12] F. Barlat and K. Lian. Plastic behavior and stretchability of sheet metals. part i: A yield function for orthotropic sheets under plane stress conditions. *International journal of plasticity*, 5(1):51–66, 1989.

[13] J. Bassani. Yield characterization of metals with transversely isotropic plastic properties. *International Journal of Mechanical Sciences*, 19(11):651–660, 1977.

[14] B. BUDIANSKY. Anisotropic plasticity of plane-isotropic sheets. In *Studies in Applied Mechanics*, volume 6, pages 15–29. Elsevier, 1984.

[15] A. Cangiani, G. Manzini, A. Russo, and N. Sukumar. Hourglass stabilization and the virtual element method. *International Journal for Numerical Methods in Engineering*, 102(3-4):404–436, 2015.

[16] J. Cao, H. Yao, A. Karafillis, and M. C. Boyce. Prediction of localized thinning in sheet metal using a general anisotropic yield criterion. *International Journal of Plasticity*, 16(9):1105–1129, 2000.

[17] A. Cazzani and M. Rovati. Extrema of young's modulus for elastic solids with tetragonal symmetry. *International journal of solids and structures*, 42(18-19):5057–5096, 2005.

[18] J. Chakrabarty. *Theory of plasticity*. Elsevier, 2012.

[19] E. Chetcuti, B. Ellul, E. Manicaro, J.-P. Brincat, D. Attard, R. Gatt, and J. N. Grima. Modeling auxetic foams through semi-rigid rotating triangles. *physica status solidi (b)*, 251(2):297–306, 2014.

[20] N. Cholewa, P. Summers, S. Feih, A. Mouritz, B. Lattimer, and S. Case. A technique for coupled thermomechanical response measurement using infrared thermography and digital image correlation (tdic). *Experimental mechanics*, 56:145–164, 2016.

[21] S. C. Cowin and M. M. Mehrabadi. Anisotropic symmetries of linear elasticity. 1995.

[22] M. Cuomo and M. Fagone. Finite deformation non-isotropic elasto-plasticity with evolving structural tensors. a framework. *Il Nuovo Cimento*, 32(1):55–72, 2009.

[23] A. Dean. Numerical computation of material tangent in implicit finite element analysis: Implementation within abaqus umat subroutine. 2024.

[24] S. Demmerle and J. Boehler. Optimal design of biaxial tensile cruciform specimens. *Journal of the Mechanics and Physics of Solids*, 41(1):143–181, 1993.

[25] S. Diebels. Lecture script: Continuum mechanics, 2020. Applied Mechanics, Saarland University.

[26] Y. Dong and B. Pan. A review of speckle pattern fabrication and assessment for digital image correlation. *Experimental Mechanics*, 57:1161–1181, 2017.

[27] F. Dos Reis and J. F. Ganghoffer. Construction of micropolar continua from the asymptotic homogenization of beam lattices. *Computers & Structures*, 112:354–363, 2012.

[28] F. Dos Reis and J.-F. Ganghoffer. Equivalent mechanical properties of auxetic lattices from discrete homogenization. *Computational Materials Science*, 51(1):314–321, 2012.

[29] F. Dunne. *Introduction to Computational Plasticity*. Oxford University Press, 2005.

[30] K. E. Evans. Auxetic polymers: a new range of materials. *Endeavour*, 15(4):170–174, 1991.

[31] K. E. Evans and A. Alderson. Auxetic materials: functional materials and structures from lateral thinking! *Advanced materials*, 12(9):617–628, 2000.

[32] K. E. Evans, M. Nkansah, I. Hutchinson, and S. Rogers. Molecular network design. *Nature*, 353(6340):124–124, 1991.

[33] H. E. Friedrich. *Leichtbau in der Fahrzeugtechnik*. Springer-Verlag, 2017.

[34] R. Gatt, L. Mizzi, J. I. Azzopardi, K. M. Azzopardi, D. Attard, A. Casha, J. Briffa, and J. N. Grima. Hierarchical auxetic mechanical metamaterials. *Scientific reports*, 5(1):1–6, 2015.

[35] M. Geiger, W. Hußnätter, and M. Merklein. Specimen for a novel concept of the biaxial tension test. *Journal of Materials Processing Technology*, 167(2-3):177–183, 2005.

[36] I. Gitman, H. Askes, and L. Sluys. Representative volume: Existence and size determination. *Engineering fracture mechanics*, 74(16):2518–2534, 2007.

[37] R. Green. A plasticity theory for porous solids. *International Journal of Mechanical Sciences*, 14(4):215–224, 1972.

[38] J. N. Grima and K. E. Evans. Auxetic behavior from rotating squares. *Materials Science Letters*, 19:1563–1565, 2000.

[39] J. N. Grima and R. Gatt. Perforated sheets exhibiting negative poisson's ratios. *Advanced engineering materials*, 12(6):460–464, 2010.

[40] M. E. Gurtin. *An introduction to continuum mechanics*, volume 158. Academic press, 1982.

[41] M. E. Gurtin, E. Fried, and L. Anand. *The mechanics and thermodynamics of continua*. Cambridge university press, 2010.

[42] A. Hannon and P. Tiernan. A review of planar biaxial tensile test systems for sheet metal. *Journal of materials processing technology*, 198(1-3):1–13, 2008.

[43] Z. Hashin. Theory of mechanical behavior of heterogeneous media. 1963.

[44] P. Haupt. *Continuum mechanics and theory of materials*. Springer Science & Business Media, 2013.

[45] S. Hess. *Tensors for physics*. Springer, 2015.

[46] A. Hildebrandt, P. Sharma, S. Diebels, and A. Düster. Nonlinear computation of cables with high order solid elements using an anisotropic material model. *PAMM*, 20(1):e202000217, 2021.

[47] R. Hill. A variational principle of maximum plastic work in classical plasticity. *The Quarterly Journal of Mechanics and Applied Mathematics*, 1(1):18–28, 1948.

[48] R. Hill. Elastic properties of reinforced solids: some theoretical principles. *Journal of the Mechanics and Physics of Solids*, 11(5):357–372, 1963.

[49] G. T. Houlsby and A. M. Puzrin. *Advanced Plasticity Theories*. Springer, 2007.

[50] T. Kanit, S. Forest, I. Galliet, V. Mounoury, and D. Jeulin. Determination of the size of the representative volume element for random composites: statistical and numerical approach. *International Journal of solids and structures*, 40(13-14):3647–3679, 2003.

[51] A. Karafillis and M. Boyce. A general anisotropic yield criterion using bounds and a transformation weighting tensor. *Journal of the Mechanics and Physics of Solids*, 41(12):1859–1886, 1993.

[52] A. S. Khan and S. Huang. *Continuum theory of plasticity*. John Wiley & Sons, 1995.

[53] V. Kompiš, M. Schanz, G. E. Stavroulakis, and S. Alvermann. Effective dynamic material properties for materials with non-convex microstructures. *Composites with Micro-and Nano-Structure: Computational Modeling and Experiments*, pages 47–65, 2008.

[54] Y. P. Korkolis and S. Kyriakides. Inflation and burst of anisotropic aluminum tubes for hydroforming applications. *International Journal of Plasticity*, 24(3):509–543, 2008.

[55] W. M. Lai, D. Rubin, and E. Krempl. *Introduction to continuum mechanics*. Butterworth-Heinemann, 2009.

[56] R. Lakes. Foam structures with a negative poisson's ratio. *Science*, 235:1038–1041, 1987.

[57] R. S. Lakes. *Viscoelastic materials*. Cambridge university press, 2009.

[58] D. Lecompte, A. Smits, S. Bossuyt, H. Sol, J. Vantomme, D. Van Hemelrijck, and A. Habraken. Quality assessment of speckle patterns for digital image correlation. *Optics and lasers in Engineering*, 44(11):1132–1145, 2006.

[59] J.-H. Lee, J. P. Singer, and E. L. Thomas. Micro-/nanostructured mechanical metamaterials. *Advanced materials*, 24(36):4782–4810, 2012.

[60] C. Lees, J. F. Vincent, and J. E. Hillerton. Poisson's ratio in skin. *Bio-medical materials and engineering*, 1(1):19–23, 1991.

[61] L. Li, J.-M. Muracciole, L. Waltz, L. Sabatier, F. Barou, and B. Wattrisse. Local experimental investigations of the thermomechanical behavior of a coarse-grained aluminum multicrystal using combined dic and irt methods. *Optics and Lasers in Engineering*, 81:1–10, 2016.

[62] G. Lijun, W. Chengyu, L. Zhanli, and Z. Zhuang. Theoretical aspects of selecting repeated unit cell model in micromechanical analysis using displacement-based finite element method. *Chinese Journal of Aeronautics*, 30(4):1417–1426, 2017.

[63] G. Lionello and L. Cristofolini. A practical approach to optimizing the preparation of speckle patterns for digital-image correlation. *Measurement Science and Technology*, 25(10):107001, 2014.

[64] Q. Liu. *Literature review: materials with negative Poisson's ratios and potential applications to aerospace and defence*. DSTO Victoria, Australia, 2006.

[65] A. Lorato, P. Innocenti, F. Scarpa, A. Alderson, K. Alderson, K. Zied, N. Ravirala, W. Miller, C. Smith, and K. Evans. The transverse elastic properties of chiral honeycombs. *Composites Science and Technology*, 70(7):1057–1063, 2010.

[66] J. Lubliner. *Plasticity theory*. Courier Corporation, 2008.

[67] H. C. Luo, X. Ren, Y. Zhang, X. Y. Zhang, X. G. Zhang, C. Luo, X. Cheng, and Y. M. Xie. Mechanical properties of foam-filled hexagonal and re-entrant honeycombs under uniaxial compression. *Composite Structures*, 280:114922, 2022.

[68] A. Maniatty, J.-S. Yu, and T. Keane. Anisotropic yield criterion for polycrystalline metals using texture and crystal symmetries. *International journal of solids and structures*, 36(35):5331–5355, 1999.

[69] A. S. U. Manual. Abaqus 6.11. *http://130.149*, 89(2080):v6, 2012.

[70] A. V. Mazaev, O. Ajeneza, and M. V. Shitikova. Auxetics materials: classification, mechanical properties and applications. *IOP Conference Series: Materials Science and Engineering*, 747(1):012008, jan 2020.

[71] L. Mizzi, D. Attard, R. Gatt, K. K. Dudek, B. Ellul, and J. N. Grima. Implementation of periodic boundary conditions for loading of mechanical metamaterials and other complex geometric microstructures using finite element analysis. *Engineering with Computers*, 37:1765–1779, 2021.

[72] S. Nemat-Nasser and M. Hori. *Micromechanics: overall properties of heterogeneous materials*. Elsevier, 2013.

[73] V. P. Nguyen, O. Lloberas-Valls, M. Stroeven, and L. J. Sluys. On the existence of representative volumes for softening quasi-brittle materials–a failure zone averaging scheme. *Computer methods in applied mechanics and engineering*, 199(45-48):3028–3038, 2010.

[74] W. Noll. On the continuity of the solid and fluid states. *Journal of Rational Mechanics and Analysis*, 4:3–81, 1955.

[75] W. Noll. A mathematical theory of the mechanical behavior of continuous media. *Archive for rational Mechanics and Analysis*, 2:197–226, 1958.

[76] H. Obrecht, P. Fuchs, U. Reinicke, B. Rosenthal, and M. Walkowiak. Influence of wall constructions on the load-carrying capability of lightweight structures. *International Journal of Solids and Structures*, 45(6):1513–1535, 2008.

[77] H. Obrecht, P. Fuchs, U. Reinicke, and M. Walkowiak. Verbesserte tragfähigkeit von dünnwandigen tragwerken durch hybridbauweise und flächenstrukturierung. *Stahlbau*, 75(9):737–741, 2006.

[78] N. S. Ottosen and M. Ristinmaa. *The mechanics of constitutive modeling*. Elsevier, 2005.

[79] P. Perzyna. Thermodynamic theory of viscoplasticity. *Advances in applied mechanics*, 11:313–354, 1971.

[80] Y. Prawoto. Seeing auxetic materials from the mechanics point of view: a structural review on the negative poisson's ratio. *Computational Materials Science*, 58:140–153, 2012.

[81] W. H. Press. *Numerical recipes 3rd edition: The art of scientific computing*. Cambridge university press, 2007.

[82] M. S. Rad, Y. Prawoto, and Z. Ahmad. Analytical solution and finite element approach to the 3d re-entrant structures of auxetic materials. *Mechanics of Materials*, 74:76–87, 2014.

[83] S. Reese and B. Svendsen. On the use of evolving structure tensors to model initial and induced elastic and inelastic anisotropy at finite deformation. In *Journal de Physique IV (Proceedings)*, volume 105, pages 31–37. EDP sciences, 2003.

[84] F. Robert. An isotropic three-dimensional structure with poisson's ratio=- 1. *J. Elast*, 15(4):427–430, 1985.

[85] J. Rossiter, K. Takashima, F. Scarpa, P. Walters, and T. Mukai. Shape memory polymer hexachiral auxetic structures with tunable stiffness. *Smart Materials and Structures*, 23(4):045007, 2014.

[86] M. Sanami, N. Ravirala, K. Alderson, and A. Alderson. Auxetic materials for sports applications. *Procedia Engineering*, 72:453–458, 2014.

[87] F. Scarpa, S. Jacobs, C. Coconnier, M. Toso, and D. Di Maio. Auxetic shape memory alloy cellular structures for deployable satellite antennas: design, manufacture and testing. In *EPJ Web of Conferences*, volume 6, page 27001. EDP Sciences, 2010.

[88] J. Schröder. *Theoretische und algorithmische Konzepte zur phänomenologischen Beschreibung anisotropen Materialverhaltens*. PhD thesis, Univ., 1996.

[89] A. Sendrowicz, A. O. Myhre, S. W. Wierdak, and A. Vinogradov. Challenges and accomplishments in mechanical testing instrumented by in situ techniques: Infrared thermography, digital image correlation, and acoustic emission. *Applied Sciences*, 11(15):6718, 2021.

[90] J. J. Skrzypek and A. W. Ganczarski. *Mechanics of anisotropic materials*. Springer, 2015.

[91] J. Smith, W. K. Liu, and J. Cao. A general anisotropic yield criterion for pressure-dependent materials. *International Journal of Plasticity*, 75:2–21, 2015.

[92] M. Spagnuolo, P. Franciosi, and F. Dell'Isola. A green operator-based elastic modeling for two-phase pantographic-inspired bi-continuous materials. *International Journal of Solids and Structures*, 188:282–308, 2020.

[93] G. Stavroulakis. Auxetic behaviour: appearance and engineering applications. *Physica status solidi (b)*, 242(3):710–720, 2005.

[94] T. C.-t. Ting and T. C.-t. Ting. *Anisotropic elasticity: theory and applications*. Number 45. Oxford University Press on Demand, 1996.

[95] C. Truesdell and C. Truesdell. *Rational mechanics of materials*. Springer, 1966.

[96] R. Usamentiaga, P. Venegas, J. Guerediaga, L. Vega, J. Molleda, and F. G. Bulnes. Infrared thermography for temperature measurement and non-destructive testing. *Sensors*, 14(7):12305–12348, 2014.

[97] W. Voigt. Bestimmung der Elasticitätsconstanten von Flussspath, Pyrit, Steinsalz, Sylvin. *Annalen der Physik*, 271(12):642–661, 1888.

[98] K. Wang, Y.-H. Chang, Y. Chen, C. Zhang, and B. Wang. Designable dual-material auxetic metamaterials using three-dimensional printing. *Materials & Design*, 67:159–164, 2015.

[99] W. Wu, J. Owino, A. Al-Ostaz, and L. Cai. Applying periodic boundary conditions in finite element analysis. In *SIMULIA community conference, Providence*, pages 707–719, 2014.

[100] Z. Xia, Y. Zhang, and F. Ellyin. A unified periodical boundary conditions for representative volume elements of composites and applications. *International journal of solids and structures*, 40(8):1907–1921, 2003.

[101] H. Yao and J. Cao. Prediction of forming limit curves using an anisotropic yield function with prestrain induced backstress. *International journal of plasticity*, 18(8):1013–1038, 2002.

[102] X. Zhang and D. Yang. Mechanical properties of auxetic cellular material consisting of re-entrant hexagonal honeycombs. *Materials*, 9(11):900, 2016.

[103] J. Zhu, Z. Mao, D. Wu, J. Zhou, D. Jiao, W. Shi, W. Zhu, and Z. Liu. Progress and trends in non-destructive testing for thermal barrier coatings based on infrared thermography: A review. *Journal of Nondestructive Evaluation*, 41(3):49, 2022.

9

Appendix

A Publications

- **Gordanshekan, A.**, Heib, T., Ripplinger, W., Herrmann, H. G., & Diebels, S. (2022). "Experimental and theoretical investigations of auxetic sheet metal." In Theoretical Analyses, Computations, and Experiments of Multiscale Materials: A Tribute to Francesco dell'Isola (pp. 689-707). Cham: Springer International Publishing.

- **Gordanshekan, A**., Ripplinger, W., & Diebels, S. (2024). RVE determination and developement of an anisotropic elastic model for auxetic sheet metal. Discover Mechanical Engineering, 3(1), 12.

B Presentations

- **Gordanshekan, A.**, Diebels, S. (Sep. 2022). "Characterization and modelling of auxetic rotating units structures." 14th Continuum Mechanics Workshop, Travemünde, Germany.

- **Gordanshekan, A.**, Diebels, S. (Nov. 2021). "Mechanical characterization of auxetic sheet metal." Poster Presentation at Doktorandentag der Naturwissenschaftlich Technischen Fakultät der Universität des Saarlandes, Saarbrücken, Germany.

C UMAT Code

```
      SUBROUTINE UMAT(STRESS,STATEV,DDSDDE,SSE,SPD,SCD,
     1 RPL,DDSDDT,DRPLDE,DRPLDT,
     2 STRAN,DSTRAN,TIME,DTIME,TEMP,DTEMP,PREDEF,DPRED,CMNAME,
     3 NDI,NSHR,NTENS,NSTATV,PROPS,NPROPS,COORDS,DROT,PNEWDT,
     4 CELENT,DFGRD0,DFGRD1,NOEL,NPT,LAYER,KSPT,JSTEP,KINC)
C
      INCLUDE 'ABA_PARAM.INC'
      REAL(8) :: E1, N12, G12, CELASTIC(3,3), EL11, EL12
      REAL(8) :: SHYDRO, sigDev(NTENS), STRESSNEW(3)
      REAL(8) :: THETA, SMISES, SYIEL0, DEQPL, HARD
      REAL(8) :: SYIELD, Fa, Fb, f, EQPLAS, DPSTRAN2(3,3)
      REAL(8) :: ENU, EBULK3, ELAM,  STRESS_UD(NTENS)
      REAL(8) :: STRESS_D(NTENS, NTENS), EPSILON_D
      REAL*8  :: STRAN_UD(NTENS), STRAN_D(NTENS, NTENS)
      REAL*8  :: STRESST2(3,3),SHYDRO2(3), SMISES2(3)
      REAL*8  :: sigDev2(3,3), FLOW2(3,3), DEQPL2(3)

      REAL*8, PARAMETER :: MACHINE_EPSILON = 1.0D-5

      CHARACTER*80 CMNAME
      DIMENSION STRESS(NTENS),STATEV(NSTATV),
     1 DDSDDE(NTENS,NTENS),DDSDDT(NTENS),DRPLDE(NTENS),
     2 STRAN(NTENS),DSTRAN(NTENS),TIME(2),PREDEF(1),DPRED(1),
     3 PROPS(NPROPS),COORDS(3),DROT(3,3),DFGRD0(3,3),DFGRD1(3,3),
     4 JSTEP(4)


      DIMENSION FLOW(NTENS),STRESST(NTENS),
     1    DPSTRAN(NTENS), DESTRAN(NTENS)

C
      PARAMETER(ZERO=0.D0, ONE=1.D0, TWO=2.D0, THREE=3.D0, SIX=6.D0,
     1 NEWTON=20.D0, TOLER=1.0D-8, PI = 3.14D0)



C ----------------------------------------------------------------
C !PROPS(1) - EMOD (Young's modulus)
C !PROPS(2) - N12 (Poisson's ratio)
C !PROPS(3) - G12 (Shear modulus)
C !PROPS(4) - SYIEL0 (Initial yield stress)
C !PROPS(5) - HARD (Plastic Hardening slope)
C !PROPS(6) - Fa (Parameter 'a' in yield function)
C !PROPS(7) - ORIENTATION ANGLE IN RADIAN (THETA)

C ----------------------------------------------------------------
C  ELASTIC PROPERTIES
C
      EMOD=PROPS(1)
      N12=PROPS(2)
      G12=PROPS(3)

      EL11=-EMOD/(N12**TWO-ONE)
      EL12=-EMOD*N12/(N12**TWO-ONE)

C ELASTIC STIFFNESS

      CELASTIC(1,1)=EL11
      CELASTIC(1,2)=EL12
      CELASTIC(1,3)=ZERO
      CELASTIC(2,1)=EL12
      CELASTIC(2,2)=EL11
      CELASTIC(2,3)=ZERO
      CELASTIC(3,1)=ZERO
      CELASTIC(3,2)=ZERO
      CELASTIC(3,3)=G12


      CALL SMISESFUNC(DSTRAN, CELASTIC, STRESS, STRESST, SHYDRO,sigDev, SMISES)

      EQPLAS=STATEV(1)
```

```
      SYIEL0= props(4)
      THETA = props(7)
      SYIEL0=SYIEL0*cos(THETA)
      HARD = props(5)
      HARD=HARD*cos(THETA)
      Fa = props(6)

      SYIELD = SYIEL0 + HARD*EQPLAS

      f = SMISES-Fa*(-SHYDRO)-SYIELD-Fa*SYIELD/TWO

      DEQPL=ZERO
      FLOW=ZERO

      IF (f .GT. TOLER*SYIELD)  THEN

      CALL DEQPLFunc(CELASTIC,SHYDRO,sigDev,SMISES,HARD,Fa,SYIELD,FLOW,DEQPL)

      STRAN_UD = DSTRAN

      DO I= 1, 3
      STRAN_D(:,I) = STRAN_UD
      EPSILON_D = MAX(MACHINE_EPSILON,
       ABS(MACHINE_EPSILON * STRAN_UD(I)))
      DO J=1, 3
      IF (I == J) THEN
      STRAN_D(I, J) = STRAN_UD(I) + EPSILON_D
      END IF
      END DO
      END DO

      DO I= 1, 3
      CALL SMISESFUNC(STRAN_D(:,
      I),CELASTIC,STRESS,STRESST2(:,I),SHYDRO2(I),sigDev2(:,I), SMISES2(I))

      CALL
      DEQPLFunc(CELASTIC,SHYDRO2(I),sigDev2(:,I),SMISES2(I),HARD,Fa,SYIELD,FLOW2(:,I),
      DEQPL2(I))

      END DO
      ENDIF

      CALL STRESS_UPD (STRESS, CELASTIC, DSTRAN,DEQPL,FLOW,
      DPSTRAN,STRESSNEW)

      STRESS=STRESSNEW
      EQPLAS=EQPLAS+DEQPL
      STATEV(1) = EQPLAS

      IF (f .LT. TOLER*SYIELD)  THEN

      DO i = ONE, NTENS
      DO j = ONE, NTENS
      DDSDDE(i,j) = CELASTIC(i,j)
      END DO
      END DO

      ENDIF

      IF (f .GT. TOLER*SYIELD)  THEN

      DO I= 1, 3

      CALL STRESS_UPD(STRESS, CELASTIC,
      STRAN_D(:,I),DEQPL2(I),FLOW2(:,I),DPSTRAN2(:,I) ,STRESS_D(:,I))

      END DO

      DO I = 1, 3
      DO J = 1, 3
      EPSILON_D = MAX(MACHINE_EPSILON,
       ABS(MACHINE_EPSILON * STRAN_UD(J)))

```

```
      DDSDDE(I, J) = (STRESS_D(I, J) -
       STRESS(I)) / EPSILON_D
      ENDDO
      ENDDO

      ENDIF

      RETURN
      END SUBROUTINE UMAT

ccccccccccccccccccccccccccccccccccccccccccccccccccccccccccccccccccccccccccccccccccccccccccccccccccccccccccc
cccc SUBROUTINE_SMISES
ccccccccccccccccccccccccccccccccccccccccccccccccccccccccccccccccccccccccccccccccccccccccccccccccccccccccccc
ccccccccccccccccc

      SUBROUTINE SMISESFUNC(DSTRAN,CELASTIC,STRESS,STRESST,SHYDRO,sigDev, SMISES)


      REAL*8, INTENT(IN)  :: DSTRAN(3), CELASTIC(3,3),STRESS(3)


      REAL*8, INTENT(OUT)  :: STRESST(3),SHYDRO, sigDev(3),SMISES

      REAL*8 :: Dsig


      PARAMETER(ZERO=0.D0, ONE=1.D0, TWO=2.D0, THREE=3.D0,SIX=6.D0)


      DO K1=1, 3
      Dsig = ZERO
      DO K2=1, 3
      Dsig = Dsig + CELASTIC(K1, K2)*DSTRAN(K2)
      END DO
      STRESST(K1)=STRESS(K1)+ Dsig
      END DO

      SHYDRO=(STRESST(1)+STRESST(2))/TWO

      DO K1=1,2
      sigDev(K1)=(STRESST(K1)-SHYDRO)
      END DO
      sigDev(3)=STRESST(3)

      SMISES= sigDev(1)**TWO+ sigDev(2)**TWO+ TWO*sigDev(3)**TWO
      SMISES=SQRT(SMISES*THREE/TWO)

      END SUBROUTINE SMISESFUNC

ccccccccccccccccccccccccccccccccccccccccccccccccccccccccccccccccccccccccccccccccccccccccccccccccccccccccccc
cccc ROUTINE_DEQPL
ccccccccccccccccccccccccccccccccccccccccccccccccccccccccccccccccccccccccccccccccccccccccccccccccccccccccccc
ccccccccccccccccc

      SUBROUTINE DEQPLFunc(CELASTIC,SHYDRO,sigDev,SMISES,HARD,Fa,SYIELD,FLOW,DEQPL)


      REAL*8, INTENT(IN)  :: sigDev(3), CELASTIC(3,3),SMISES, HARD, Fa, SYIELD, SHYDRO


      REAL*8, INTENT(OUT)  :: FLOW(3), DEQPL

      REAL*8 :: CFLOW(3), ALPHA, BETA, GAMMA,TRB, HMODL, RHS, TERM1, DDEQPL


      INTEGER :: KEWTON

      PARAMETER(ZERO=0.D0, ONE=1.D0, TWO=2.D0, THREE=3.D0,SIX=6.D0, NEWTON=20.D0)

      DO K1=1,2
      FLOW(K1)=(THREE/TWO)*(sigDev(K1))
      FLOW(K1)=FLOW(K1)/SMISES
      FLOW(K1)=FLOW(K1)+(Fa/TWO)
```

```
      END DO

      FLOW(3)=(THREE/TWO)*sigDev(3)
      FLOW(3)=FLOW(3)/SMISES

      CFLOW=ZERO
      DO K1=1,3
      DO K2=1,3
      CFLOW(K1)=CFLOW(K1)+CELASTIC(K1,K2)*FLOW(K2)
      END DO
      END DO
      CFLOW(3)=TWO*CFLOW(3)

      ALPHA=ZERO
      DO K1=1,3
      ALPHA=ALPHA+sigDev(K1)*CFLOW(K1)
      END DO
      ALPHA=ALPHA+sigDev(3)*CFLOW(3)

      BETA=ZERO
      DO K1=1,3
      BETA=BETA+CFLOW(K1)*CFLOW(K1)
      END DO
      BETA=BETA+CFLOW(3)*CFLOW(3)

      DEQPL=ZERO

      GAMMA=SMISES**TWO-THREE*ALPHA*DEQPL
      GAMMA=GAMMA+(THREE/TWO)*BETA*DEQPL**TWO
      GAMMA=SQRT(GAMMA)

      TRB=CFLOW(1)+CFLOW(2)

      HMODL=-HARD*(ONE+Fa/TWO)

      RHS=GAMMA+(Fa/TWO)*(TWO*SHYDRO-DEQPL*TRB)
      RHS=RHS-SYIELD*(one+Fa/TWO)

      KEWTON = ONE


      Do While (KEWTON .LT. NEWTON .and. RHS .GT. ZERO)

           SYIELDNEW = SYIELD + HARD*DEQPL
           GAMMA=SMISES**TWO-THREE*ALPHA*DEQPL
           GAMMA=GAMMA+(THREE/TWO)*BETA*DEQPL**TWO
           GAMMA=SQRT(GAMMA)
           RHS=GAMMA+(Fa/TWO)*(TWO*SHYDRO-DEQPL*TRB)
           RHS=RHS-SYIELDNEW*(one+Fa/TWO)
           TERM1=(ONE/TWO)*GAMMA**(-ONE/TWO)
           TERM1=TERM1*(THREE*DEQPL*BETA-THREE*ALPHA)
           TERM1=TERM1-(Fa/TWO)*TRB+HMODL
           DDEQPL=-RHS/TERM1
           DEQPL= DEQPL+DDEQPL
           KEWTON = KEWTON+ONE

      END DO

      END SUBROUTINE DEQPLFunc

cccccccccccccccccccccccccccccccccccccccccccccccccccccccccccccccccccccccccccccccccccccc
cccc ROUTINE_STRESS_UPD
cccccccccccccccccccccccccccccccccccccccccccccccccccccccccccccccccccccccccccccccccccccc
cccccccccccccccccc

      SUBROUTINE STRESS_UPD(STRESS, CELASTIC, DSTRAN,DEQPL,FLOW,
      DPSTRAN,STRESSNEW)

      REAL*8, INTENT(IN)   ::  STRESS(3), CELASTIC(3,3),DSTRAN(3), DEQPL, FLOW(3)


      REAL*8, INTENT(OUT)  :: DPSTRAN(3), STRESSNEW(3)

```

```
278         REAL*8 :: DESTRAN(3), DsigNew(3)
279
280
281         PARAMETER(ZERO=0.D0, ONE=1.D0, TWO=2.D0, THREE=3.D0,SIX=6.D0, NEWTON=20.D0)
282
283         DO K1=1, 3
284             DPSTRAN(K1)=DEQPL*FLOW(K1)
285         END DO
286
287         DO K1=1, 3
288         DESTRAN(K1)=DSTRAN(K1) - DPSTRAN(K1)
289         END DO
290
291         DsigNew=ZERO
292         DO K1=1, 3
293         DO K2=1, 3
294         DsigNew(K1)=DsigNew(K1)+CELASTIC(K1,K2)*DESTRAN(K2)
295         END DO
296         END DO
297
298         DO K1=1, 3
299         STRESSNEW(K1)=STRESS(K1)+DsigNew(K1)
300         END DO
301
302         END SUBROUTINE STRESS_UPD
303
304
305
306
307
308
309
310
311
312
313
314
315
316
317
318
319
320
321
322
323
324
325
326
```